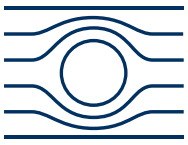

TECHNISCHE UNIVERSITÄT MÜNCHEN

WALTHER-MEISSNER-INSTITUT

BAYERISCHE AKADEMIE DER WISSENSCHAFTEN

Magnetism and Geometrical Frustration in Archimedean Lattices

Master's thesis

Ramona Melinda Stumberger

Supervisor: Prof. Dr. Rudi Hackl

Garching – December 6, 2021

Contents

1. Introduction

Back in ancient Greece, Archimedes was one of the first people to describe two-dimensional regular patterns. Until now, there are eleven different uniform two-dimensional Archimedean lattices, which are formed from 2D arrangements of regular polygons with every site being topologically equivalent [1–4]. Artists and Scientists in the Renaissance such as Leonardo DaVinci or Albrecht Dürer rediscovered these Archimedean patterns and incorporated them as well as regular and semi-regular polyhedra already known in antiquity in paintings and architecture [5]. In 1619 Kepler derived a complete description of these 2D and 3D patterns in his "Harmonices Mundi" and proved that there exist only eleven Archimedean lattices [2, 6].

As they exhibit exotic physical properties due to geometrical frustration materials with an archimedean lattice attract more and more attention in the fields of condensed matter physic and material science. They provide an ideal playground to systematically study the interplay between magnetic interaction, lattice topology and quantum fluctuations [1]. One speaks of geometrical frustration, which origins in a crystal lattice structure and the frustration of spins, if nearest neighbor interactions compete with each other and hence, a system is unable to simultaneously minimize the competing interactions to the neighboring spins. In 1977 Gerard Toulouse introduced the term frustration in the context of magnetic systems [7, 8], although they had been studied before, for example by G.H. Wannier in 1950 in the context of the Ising model on a triangular lattice [9]. In the early 1970ies spin systems with competing or frustrated interactions have drawn a renewed interest, especially in the context of spin glasses [10].

One of the material groups hosting an Archimedean lattice structures and hence being prone to geometrical frustration exhibit multiple types of exotic properties such as topological non-trivial electronic structures, charge density waves [11] and superconductivity [12, 13] are the Kagome-lattice materials.

Furthermore, the coexistence of Dirac cones and flat bands can produce correlated topological states, and the presence of a magnetic order stabilizes novel quantum anomalous Hall behaviour [14–16]. A subgroup of the Kagome materials consists of the basic building blocks T_3X with T = Fe, Mn, Co and X = Ge, Sn. One example is the itinerant Kagome ferromagnet Fe_3Sn_2, where the spin reorientation induces frustrated ferromagnetism [17]. Fe_3Sn_2 also possesses an unusual anomalous Hall effect being three orders of magnitude larger that the anomalous Hall effect in pure Fe [18]. Another member of this material group is the Weyl semimetal $Co_3Sn_2S_2$, which hosts a giant anomalous Hall effect [19]

and a large Berry curvature [20]. In 2019, another family of layered Kagome metals was discovered by Ortiz *et al.* [21], which have the structure AV_3Sb_5 (A = K, Rb, Cs). These two-dimensional metals with high mobility are playgrounds for metallic Dirac physics, frustrated magnetism, unconventional superconductivity among other exotic quantum phenomena. For this thesis the compound CsV_3Sb_5 is of special interest, as it develops, in addition to topological superconductivity, a charge density wave below 94 K, indicating strong electronic correlations [22].

The rare-earth tetraboride TmB_4 is also a member of the Archimedean lattice materials, and its sublattices have the same topology as a frustrated Shastry-Sutherland lattice consisting of perfect squares and nearly equilateral triangles of Tm atoms. Rare-earth tetraborides in general have a long-range magnetic ground state [23] and exhibit rich phase diagrams as a function of magnetic field and temperature [24]. TmB_4 also exhibits two additional magnetic effects, namely a magneto-caloric and a rotating magneto-caloric effect [25].

As Raman scattering is a sensitive method to analyze lattice-, electron- and spin dynamics, it affords a window into various types of exotic phenomena, the underlying interactions, an the interrelation thereof. Raman spectra show the superposition of all possible excitations at their corresponding energies in different symmetries [26], which are mapped via the Raman selection rules and show for instance, the impact of electronic of magnetic phase transitions on optical phonons [27].

The thesis is organized as follows: Chapter 2 introduces the examined Kagome lattice materials Fe_3Sn_2, $Co_3Sn_2S_2$, and CsV_3Sb_5, and the Tetraboride TmB_4, their lattice structure, and both their electronic and magnetic properties. Chapter 3 gives an overview of the concepts of Raman scattering. Chapter 4 describes the experimental setup for inelastic light scattering used in this thesis. The experimental Raman scattering results are presented in Chapter 5, which are then discussed in Chapter 6. Chapter 7 summarizes the results obtained.

2. Properties of Kagome Lattice Materials and Tetraborides

The following chapter gives an overview of three specific materials with a Kagome lattice structure, in particular Fe_3Sn_2, $Co_3Sn_2S_2$ and CsV_3Sb_5. Additionally, the tetraboride TmB_4 and its properties are described.

2.1. Kagome Lattice Materials

Materials with Kagome lattice structures can be divided into two different categories: insulating or metallic (semi-metallic) materials. For the latter group, a broad spectrum of instabilities is possible, depending on the degree of electron filling. These include, for example, the wave order of the bond density [12, 28], charge density waves [11] and superconductivity [12, 13].

In addition, these materials enable the investigation of topologically non-trivial electronic structures. Here, the coexistence of Dirac cones and flat bands, which promote strong correlation effects, can produce correlated topological states. For example, the presence of a magnetic order stabilizes [14–16] novel quantum anomalous Hall behavior. Moreover, electron-electron interactions can promote the formation of topological insulating phases [29]. In Fe_3Sn_2, the presence of ferromagnetic ordering leads to the splitting of the spin-degenerate Dirac bands. This leads to the generation of a topologically nontrivial phase and a two-dimensional "Chern gap" [15]. A large anomalous Hall reaction and a large Berry curvature make $Co_3Sn_2S_2$ an attractive Weyl semimetal candidate [20]. Besides the two mentioned materials, another family of layered Kagome metals has recently been discovered, which have the structure AV_3Sb_5 (A = K, Rb, Cs) [21]. These compounds are two-dimensional metals with high mobility and exhibit both correlation effects and potential electronically controlled symmetry breaking [22].

2.1.1. Lattice Structure

Fe_3Sn_2 and $Co_3Sn_2S_2$

The basic building blocks of a subgroup of the Kagome lattice materials examined in this thesis is T_3X, where T = Fe, Mn, Co and X = Ge, Sn. As shown in Fig. 2.1.1 these Kagome layers are perfectly aligned being either interleaved with Graphite like sulfur (S) layers, tin (Sn) layers [Fe_3Sn_2: Fig. 2.1.2 (b)] or both of them [$Co_3Sn_2S_2$: Fig. 2.1.2 (a)]. These Kagome

lattices have a rhombohedral lattice structure with the space group R$\bar{3}$m (Nr. 166). This space group has a triple rotation axis, threefold mirror planes and an inversion center [30].

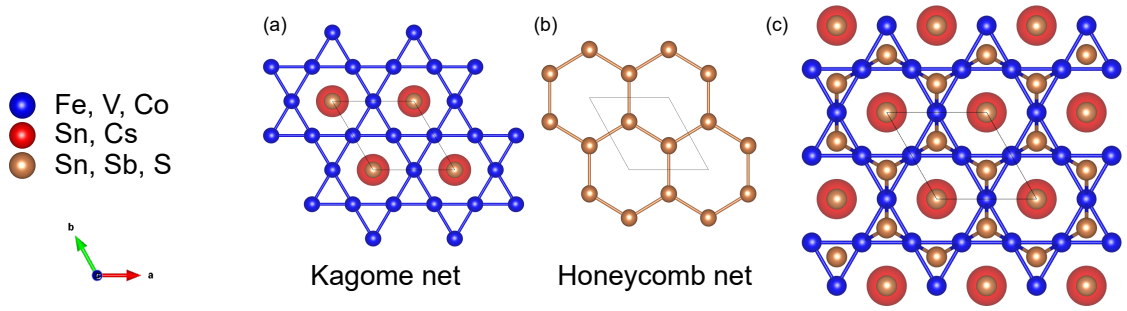

Figure 2.1.1.: 2D lattice structure of the kagome lattices [Fig. 2.1.1 (c)]: Structurally perfectly aligned kagome lattices [blue atoms in Fig. 2.1.1 (a)] are interleaved with two different kind of sublattices. The first sublattice is a simple hexagonal net, which is formed by the X-atoms [red spheres in Fig. 2.1.1 (a)]. The second sublattice is a honeycomb lattice below and above each kagome lattice [gold coloured atoms in Fig. 2.1.1 (b)]. Adapted from [21, 22]

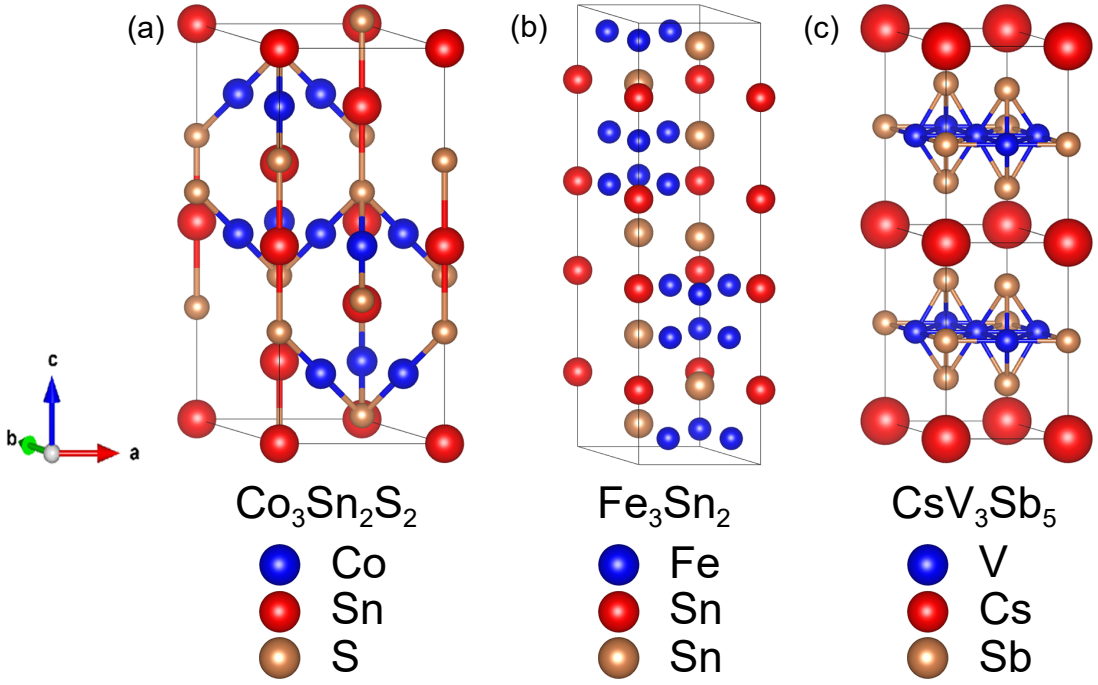

Figure 2.1.2.: Crystal structures of the relevant kagome lattice material investigated in this work. Adapted from [17, 22, 31]

CsV_3Sb_5

The layered superconductor CsV_3Sb_5 shown in Fig. 2.1.2 (c) with a $T_C \approx 2.5$ K [22] has a hexagonal crystal structure with V-Sb layers intercalated by Cs. These consist of a structurally perfect, 2D kagome lattice of vanadium [Fig. 2.1.1 (a)]. The first Sb-sublattice is a simple hexagonal net, which is centered on each kagome hexagon. The second sublattice

formed by Sb-atoms forms a honeycomb layer [Fig. 2.1.1 (b)] located above and below each kagome layer [22, 32].

2.1.2. Electronic Structure

Band Structure

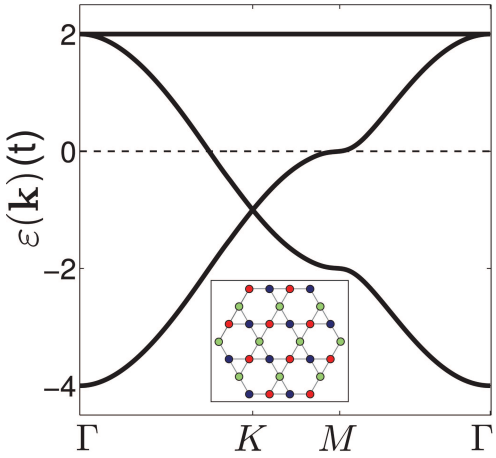

Figure 2.1.3.: Tight-binding model band structure in units of the kinetic energy term in the tight binding model t resulting from the three-sublattice structure of the kagome lattice shown in the inset. Taken from [33].

The theoretical band structure of Kagome lattice materials from a tight binding model, which is shown in Fig. 2.1.3 exhibits various characteristic properties for Kagome lattices. The highest band above the Fermi energy is a a flat band with low dispersion. The two lower bands are Dirac bands, which cross linearly at the K point. If one includes spin orbit coupling (SOC), anti-crossings can occur leading to a gap opening [34].

At the M point the two lower bands show saddle points, which means the dispersion curve runs horizontally and therefore the group velocity goes to zero. Since the dispersion slope is flat at this point, so called Van Hove-singularities or critical points occur at the M point in the density of states [35]. For energies close to the Fermi level this divergence in the density of states can lead to increased electron correlation with quasiparticles, resulting in various ordered phases of matter such as superconductivity, magnetism and density waves [36].

Expanding on this simple and general approach of a Kagome lattice, the three separate crystals of $Co_3Sn_2S_2$, Fe_3Sn_2 and CsV_3Sb_5 are now described in more detail.

The band structure of $Co_3Sn_2S_2$ obtained by density functional theory (DFT) calculations, which is pictured in Fig. 2.1.4 (a), leads to the following three key points: (i) The spin-up channel crosses the Fermi level, which leads to a metallic character, in contrast to the insulating spin down channel with a gap of 0.35 eV. (ii) Two hole pockets are located at L point and $L-U$ path and two electron pockets at the Γ point and $L-\Gamma$ path. This makes

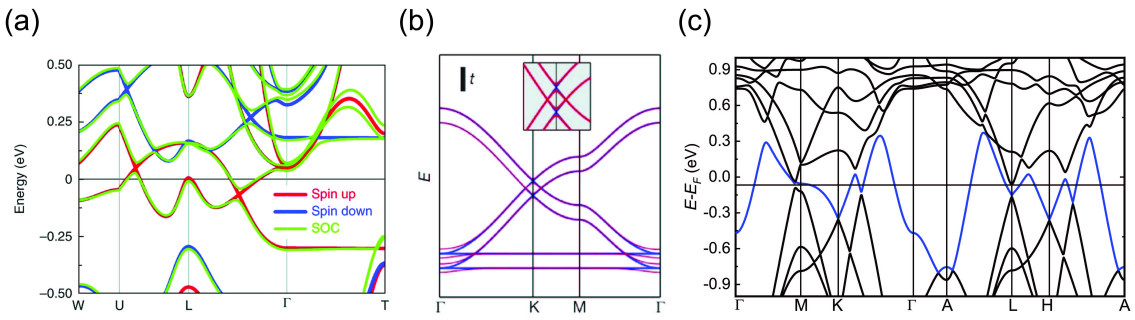

Figure 2.1.4.: (a) Band structure of $Co_3Sn_2S_2$ [20]. (b) Tight-binding band model of Fe_3Sn_2 with (red) and without (blue) spin–orbit coupling. The in-set shows a magnified view of the double Dirac structure near the K point. The spin–orbit coupling strength was set to $\lambda = 0.05$ t [15]. (c) Calculated electronic band structure of CsV_3Sb_5 along the high-symmetry directions across the Brillouin zone. The band, which crosses the E_F is highlighted in blue. Adapted from [37].

the compound semimetal-like. (iii) Linear band crossings appear along $L-\Gamma$ paths slightly below and along the $L-U$ paths slightly above the Fermi energy, which open small gaps with band anti-crossings for finite spin-orbit coupling [20].

The band structure of Fe_3Sn_2 is shown in Fig. 2.1.4 (b). Tight-binding calculations in the double-layer kagome lattice are sufficient to reproduce the main features of the band dispersion in this material. Two overlapped Dirac cones can be found at the K point, which are located 70 meV and 180 meV below the Fermi level, respectively. A gap opening of 30 meV was identified at the second Dirac point. Therefore, massive Dirac fermions at the K point dominate the physical properties of Fe_3Sn_2. According to Ye *et al.* [15] the k_z dispersion of this system appears to be irrelevant for this material, indicating the quasi 2D nature of Fe_3Sn_2.

The band structure of CsV_3Sb_5 is pictured in Fig. 2.1.4 (c). First-principle DFT calculations show a metallic behaviour. The band crossing the Fermi level E_F is highlighted in blue. Dirac-like features are the origin of most of the band crossings at various points like H, K, L or even along the $H-A$ and the $\Gamma-K$ directions of the Brillouin zone. Multiple Dirac points with nearly linear dispersion are located near the Fermi level E_F. The band crossings with nearly linear dispersion at K and H are not isolated Dirac cones. According to Ortiz *et al.* [21] taking the dispersion along $K-H$ into account leads to connected features, which form a conical valley. Van Hove singularities occur at the Γ and the M point close to the Fermi energy [21, 22, 32, 37]

Weyl-Points

When talking about coincidental touching points of non-degenerate bands corresponding to magnetic monopoles in momentum space [39], one talks about the so-called Weyl points. These are sources or sinks of Berry curvature [40]. Either time reversal symmetry (broken by ferromagnetic transition) or space inversion symmetry should be broken to form these double degenerate Weyl points. This is the difference between a Weyl point and a Dirac

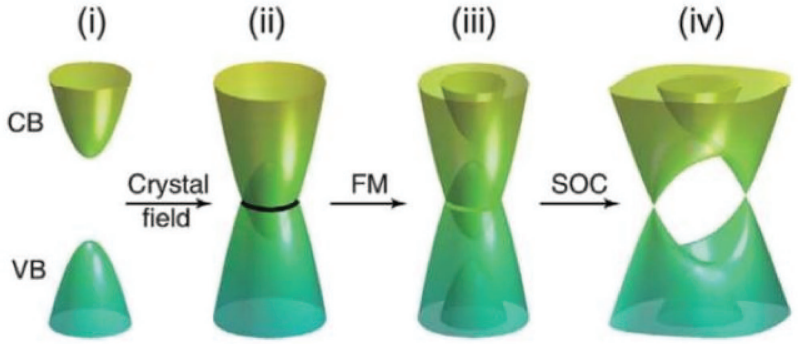

Figure 2.1.5.: Schematic drawing illustrating the formation of Weyl points in $Co_3Sn_2S_2$. The crystal field shifts the bands (i) and makes them overlap (ii). (iii) Ferromagnetism (FM) splits the individual bands in spin-up and spin-down parts. (iv) The spin-orbit interaction (SOC) introduces a coupling between the bands which leads to a gap in most parts of the BZ except for the high-symmetry points.Taken from [38]

point, which is four-fold degenerate and protected by both time reversal and spacial inversion symmetry. The mechanism for the formation of Weyl points in magnetic semimetals is depicted in Fig. 2.1.5. To form a four-fold degenerate (i.e. $+k\uparrow$, $+k\downarrow$, $-k\uparrow$, $-k\downarrow$) nodal ring, the crystal field mixes the conduction band (CB) with the valence band (VB). Afterwards, ferromagnetic transition lifts the spin degeneracy and with the existence of spin-orbit coupling (SOC) the nodal ring splits into a pair of so-called Weyl points with opposite chirality [38].

$Co_3Sn_2S_2$ is a magnetic Weyl semi metal, which is confirmed by different experiments in the form of the intrinsic large anomalous Hall effect [20, 41], the zero-field Nernst effect [31], and surface Fermi arcs by scanning tunneling microscopy (STM) and angle-resolved photo emission spectroscopy (ARPES) [16, 38]. In this material six nodal rings can be found, whose planes are perpendicular to the $k_x - k_y$ plane [30]. As described earlier the nodal ring splits and a gap opens except for two Weyl points [Fig. 2.1.5 (iv)], which have opposite chirality and are located 60 meV above the Fermi Energy [20]. There are six Weyl-points in the first Brillouin zone [41].

On one hand Fe_3Sn_2 is considered to host massive Dirac electronic states. Here the bulk Dirac cones open gaps below the Fermi Energy at the corner of the Brillouin zone [15]. On the other hand Yao *et al.* argued that Fe_3Sn_2 is a Weyl semimetal, where the quantity and locations of the Weyl points depend on the orientation of the magnetization. They assume the threefold rotational degeneracy of the magnetic domains to be the reason for the absence of Weyl-points in ARPES data of Fe_3Sn_2 [42].

In CsV_3Sb_5 ARPES measurements combined with DFT calculations show the existence of multiple Dirac points near the Fermi level E_F. There are also topologically protected surfaces states at the M point located only 0.05 eV above the Fermi level E_F [22].

Flat band dispersion

The existence and impact of flat bands on the physical properties of $Co_3Sn_2S_2$ is still a highly debated topic. According to Yin *et al.* there exists a flat band below the Fermi level [43]. They found a sharp peak at $E_p = -8$ meV in tunneling spectra of a S−terminated surface, which is associated with flat band induced features. Such a peak on S−surface was reproduced by LDOS calculations. Here the enhanced DOS comes from the contribution of Co $3d$ electrons. Xu *et al.* [44] on the other hand found an asymmetric peak-like feature at 38 meV in optical conductivity spectra, which was suggested to arise from a flat band. Yet, the theoretically predicted energy scale of this feature is much higher than the experimentally observed one in tunneling spectra. ARPES measurement refute the existence of extended flat bands over the entire Brillouin zone due to the interlayer hybridization. The strong k_z dispersion already mentioned also does not support the existence of a flat band. Nevertheless DFT and DMFT calculations predict flat bands centered at the L point, which connect the Weyl points. These flat bands could still exist within a small range and close to the Fermi level, which would be hard to identify by ARPES due to both the low spectral weight or the low energy resolution.

In Fe_3Sn_2 a flat band was found around 0.2 eV below the Fermi energy by both STS and ARPES experiments [45]. This flat band is centered at the Γ-point, which is consistent with DFT calculation.

According to Hu *et al.* [46] CsV_3Sb_5 does exhibit a flat band around -1.2 eV, which can be found across the entire momentum space. This flat band exists in both ARPES measurements and DFT calculations at the same energy. Another non-dispersive feature was found in the region of E_F, which is similar to the one found in FeSn [14]. Not only the kagome physics might be the origin of this non-dispersive feature near E_F, but the existence of quasi-1D stripe order [32, 47], the formation of dangling bonds on the surface [48, 49] or a magic twist angle between adjacent layers [50–52].

Charge Density Wave

According to Peierl, at low temperatures, a 1D metal, which couples to the underlying lattice, is not stable and is therefore susceptible to periodic lattice distortion. This distortion changes the lattice periodicity and hence can lower the total energy of the system. This phenomenon is pictured in Fig. 2.1.6. Fig. 2.1.6 (a) illustrates the ground state without accounting for interactions between electrons or electrons and phonons at T $= 0$ K. The atoms, shown as blue circles, are located at the same distance a from one another. The electronic states are filled up to the Fermi surface E_F and the Fermi wave vector k_F, which means the electron band is half occupied. If interactions between electrons and phonons are considered, a lattice distortion with the periodicity $\lambda = \pi/k_F$ is energetically favourable. Here, the previously equidistant atoms now move closer to one neighbour atom and further away from another neighbouring atom. Therefore the lattice constant a doubles, but

the unit cell now not only contains one atom but a pair of atoms. This opens a finite energy gap 2Δ at the Fermi level at $\pm\pi/2a$ in k-space, which is depicted in Fig. 2.1.6 (b). As metals have a constant charge density ρ_0, the formation of an energy gap transforms a metallic to an insulating phase, where the conduction electrons can be modulated statically by a standing wave, the so-called charge density wave (CDW). Therefore, the charge density can be described by $\rho(r) = \rho_0 + \rho_1 \cos(2k_\mathrm{F} \cdot r + \phi)$ with the amplitude ρ_1 and phase ϕ of the periodically modulated electron density and the displacement r. The CDW most likely forms, if Fermi surface nesting with wave vector $\mathrm{Q} = 2k_\mathrm{F}$ occurs, which means areas at the Fermi surface are connected by the same wavevector Q, the so-called Nesting vector. Gaps, which modify the Fermi surface, form at these nested positions and due to that, the system can gain energy. If this gained energy is bigger than the energy lost due to the strain associated with the periodic lattice distortion, a CDW can be formed. In addition, strong electron-phonon coupling is required to form a CDW [53–56].

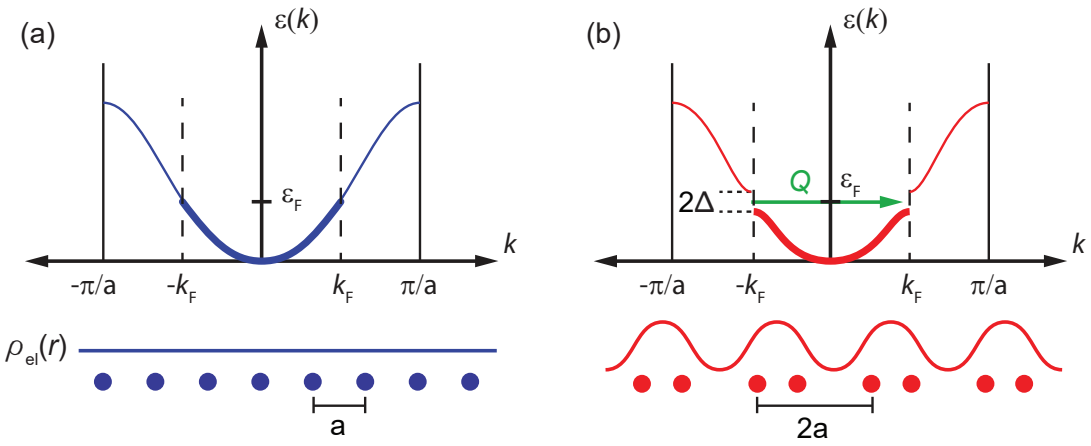

Figure 2.1.6.: Schematic drawing of Peierls distortion in 1D metal. (a) Without interactions like electron-phonon interaction or electron-electron interactions the electron states are filled up to the Fermi level and the charge density is constant. (b) If these interactions are considered, Peierl's distortion occurs and an energy gap 2Δ opens at the Fermi level at $\pm\pi/2a$. This results in a periodically modulated charge density. Taken from [27].

In 2D materials multiple bands, electron-electron correlations and spin-orbit coupling can manifest simultaneously. Due to these various interactions the formation mechanism for a CDW is more complex. Possible mechanisms for forming CDWs could be electronic-based mechanisms due to van Hove singularities, Fermi surface nesting or strong electron-phonon coupling.

According to Wang *et al.* [57] single crystal x-ray diffraction (XRD) experiments suggest the existence of charge density wave order in CsV_3Sb_5 below the CDW critical temperature $T_{CDW} = 94$ K [22].

2.1.3. Magnetism

$Co_3Sn_2S_2$ is a ferromagnetic material with $T_C = 175$ K as determined by magnetization, resistivity and specific heat measurements [20, 38, 58]. An anomalous magnetic transition occurs around 150 K at low field (0.0025 T = 25 Oe) in the zero field cooled (ZFC) curve, which is suppressed during the field cooled (FC) measurement as well as for higher external magnetic fields. The magnetic momenta are parallel to the c-axis in the ground state, which is confirmed by DFT calculations and longitudinal magnetization measurements [59].

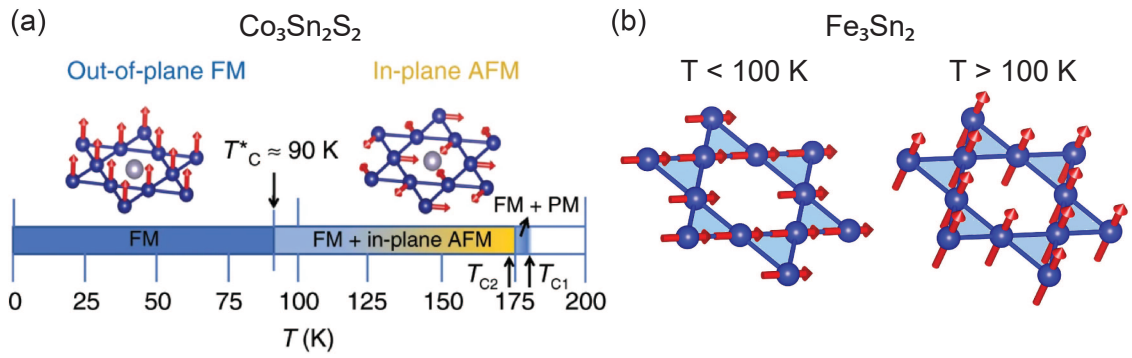

Figure 2.1.7.: (a) In-plane antiferromagnetic and out-of-plane ferromagnetic order in $Co_3Sn_2S_2$. The magnetic phase is shown in a schematic diagram as a function of temperature and spin structures (out-of-plane FM and the in-plane AFM structures) of $Co_3Sn_2S_2$. The arrows highlight the critical and the transition temperatures ($T_{C1} = 177$ K, $T_{C2} = 172$ K and $T_C^* = 90$ K). Taken from [60]. (b) Spin reorientation in Fe_3Sn_2 around $T_f \approx 100$ K: When reducing the sample temperature, the spins first rotate from parallel for $T_f < 100$ K to perpendicular alignment and then to the kagome planes for $T_f > 100$ K.

The Co-spins have both ferromagnetic interactions along the c-axis as well as antiferromagnetic interactions within the kagome plane, which compete with each other as shown in Fig. 2.1.7 (a). Two oscillating components of μSR time spectra between 90 K − 177 K were found, which stem from an out-of-plane FM and an in-plane AFM interaction. Only one component can be identified below 90 K. In the AFM state, the spins are aligned non-colinearly at an angle of 120°. AFM as well as FM states can be tuned by pressure and magnetic field. Increasing pressure suppresses both AFM and FM and the AFM state disappears below an applied magnetic field of 0.1 T [60]. With Neutron scattering experiments [58] a spin wave gap below T_C was discovered, whose gap energy is approximately 2.3 meV in the ground state. Generally, spin waves of ferromagnetic metals are either gap-less in the weak correlation limit, or exhibit an isotropic spin gap following the magnetic order parameter in the strong correlation limit with SOC. The spin wave gap is considerably larger than the estimated spin anisotropy energy [58] due to possible contributions from the Weyl fermions. This indicates that the low-energy spin dynamics can interplay with the topological states.

Fe_3Sn_2 is an unusual magnetic conductor with a high $T_C = 670$ K, which undergoes

an unexplained spin reorientation at $T_f \approx 100$ K [42, 61, 62] [Fig. 2.1.7 (b)]. The magnetization rotates from perpendicular to the kagome planes to parallel while cooling down. Two mechanisms for ferromagnetism can be found on the kagome lattice: The first one is Mielke's flat-band ferromagnetism [63, 64]. This is an extreme case of the Stoner instability, which reduces the potential energy of repulsive electron-electron interactions. The second one is Nagaoka-type ferromagnetism [65] which is a result of the gain in kinetic energy of electrons [66]. The dominant mechanism for the formation of magnetic order in these materials is still under debate.

Unlike $Co_3Sn_2S_2$ or Fe_3Sn_2, CsV_3Sb_5 has no resolvable magnetic order [22].

2.2. Tetraborides

The interplay of geometric frustration with strong correlations can lead to exotic quantum phases such as superconductivity in organic materials [67] and quantum spin liquid in frustrated magnets [68]. The rare earth (RE) tetraborides (RE = C, Er, La, Y, Tm, Eu, etc.) are members of the metallic frustrated magnets, which have long range magnetic ground states [23]. According to Kato *et al.* [69] and Olsen *et al.* [70], who made high-resolution structural refinement of LaB_4 and HoB_4, respectively, the RE-RE bonds in both materials, which correspond to J_1 and J_2 are nearly equal in length. Due to this fact, the RE sublattice belongs to the eleven Archimedean lattices. Other members of the frustrated Archimedean lattices are triangular lattices or Kagome lattices, which were already discussed in this thesis [1, 71, 72].

2.2.1. Lattice Structure

REB_4 materials belong to the space group $P4/mbm$ (127) and crystallize in a tetragonal structure. The crystal structure is shown in Fig. 2.2.1 in (a) 3D and (b) 2D in the (a,b) plane. In addition to the B_6 octahedra and metal atoms in hexaborides, RE tetraborides also consist of planar dimer pair B_2 units. Below or above these dimer pairs are no extra-planar borons. Therefore, their 2 p_z are not occupied and thus couple most strongly to the Tm $4f$ level electrons.

The atom Boron is expected to form 6-element rings, but in contrast to TmB_2 this is not the case in TmB_4. Here the Boron atoms form 7-atom rings. This can be seen in Fig. 2.2.1 (b) [73] . The purple atoms represent the rare-earth thulium atoms and the green and orange atoms illustrate the B_6 octahedra and the B_2 units, respectively, which form alternating layers of Tm and B [Fig. 2.2.1 (a)].

The thulium lattice is orientated perpendicular to the tetragonal c-axis [73]. This lattice consists of 2D sublattices and each sheet has the same topology as a frustrated Shastry-Sutherland lattice (SSL), which consists of perfect squares and nearly equilateral triangles of Tm atoms [72–74].

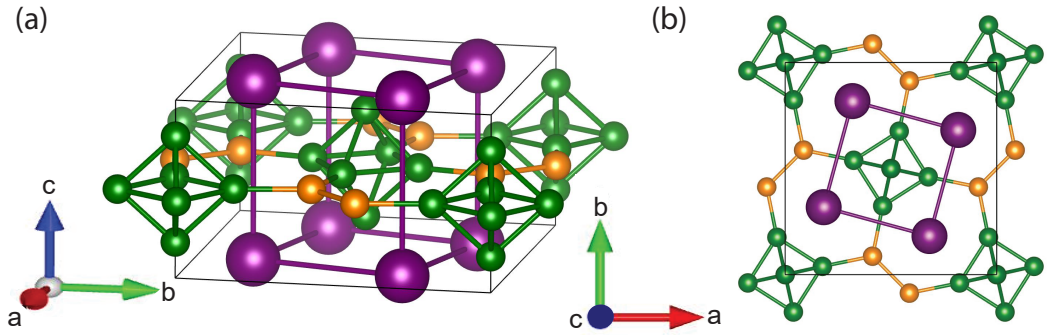

Figure 2.2.1.: Crystal structure of TmB_4. Tm atoms (purple) and B atoms (B_6 octahedra in green and B_2 units in orange) form alternating layers. (a) 3D crystal structure (b) 2D lattice structure of the (a,b) plane [72, 74, 75].

2.2.2. Electronic Structure

In the works of Pakhira *et al.* [23] significant dispersion along various high symmetry directions are detected in angle resolved photo-emission spectra (ARPES). Along the $X-M$ line a flat band and therefore no dispersion occurs. The band structure calculated within GGA (Generalized Gradient Approximation) shows four bands crossing the Fermi level. The bands are mostly of Tm f-character. Spin orbit coupling, which modifies the topology of the Fermi surface, occurs due to the large atomic mass of thulium.

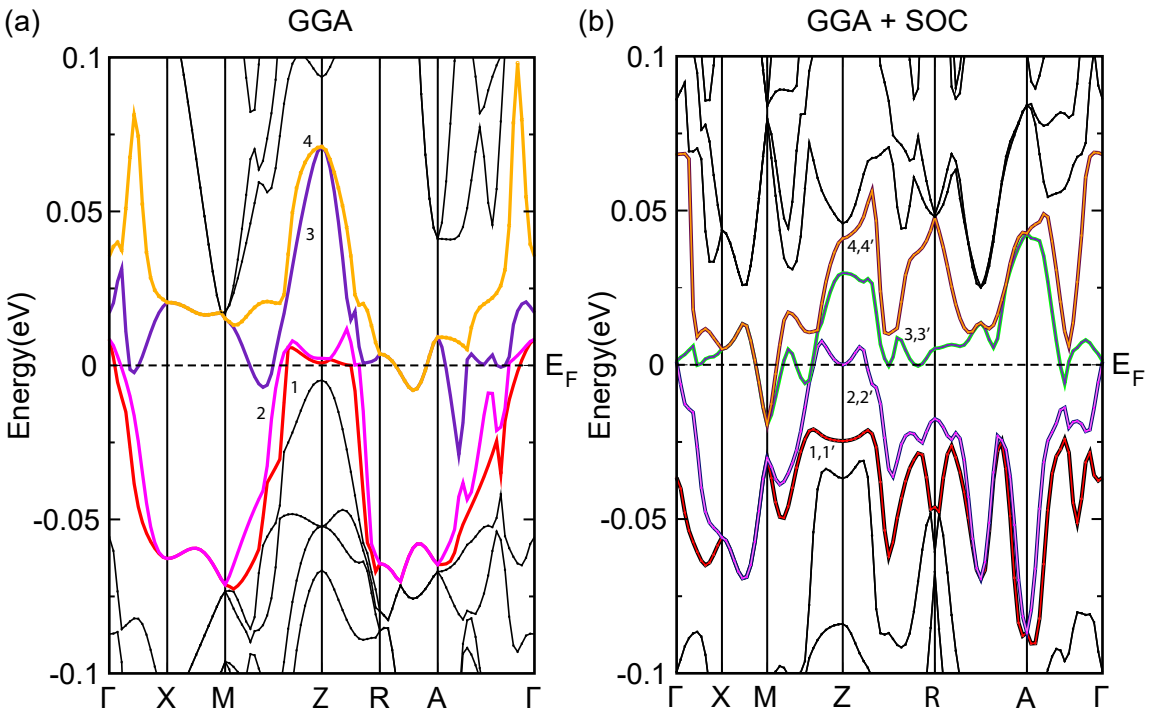

Figure 2.2.2.: Band structure of TmB_4 within (a) GGA and (b) GGA + SO. All bands, which cross E_F are highlighted in different colours. Adapted from [23].

Taking spin-orbit interaction into account, the bands, which cross the Fermi level double and some of these bands are degenerate. Only 6 (2,2′; 3,3′; 4,4′) of these 8 new bands cross the Fermi level. The other two (1,1′) are pushed below E_F. The Fermi surface, which corresponds to the degenerate bands (2,2′), has disconnected hole pockets along the $Z - \Gamma - Z$ path, while the Fermi surface, which corresponds to the degenerate bands (3,3′) and (4,4′) has hole pockets at the R point. In addition, the Fermi surface of bands 5 and 6 also consists of electron like pockets. Some of the valence electrons of TmB_4 are delocalized in a conduction band, and are therefore itinerant electrons, while others fill the bonding orbitals. Two electrons from each metal atom (rare-earth materials) are required to stabilize the boron framework of the REB_4 materials [76]. One of the three valence electrons per rare-earth ion (RE^{3+}) goes into the conduction band. Thus, tetraborides are good metals. The RKKY exchange interaction, which describes the indirect exchange between localized magnetic moments of the metal atoms, plays an important role. Another interesting aspect about TmB_4 are the strong correlation effects and the large Hund's coupling. Due to these effects the degeneracy of certain manifolds is lifted at low temperatures. Some orbitals in other manifold still remain degenerate [23–25, 72, 73].

2.2.3. Magnetism

Now the magnetic properties of TmB_4 as examined by Siemensmeyer *et al.* [24] and Orendáč *et al.* [25] will be reviewed.

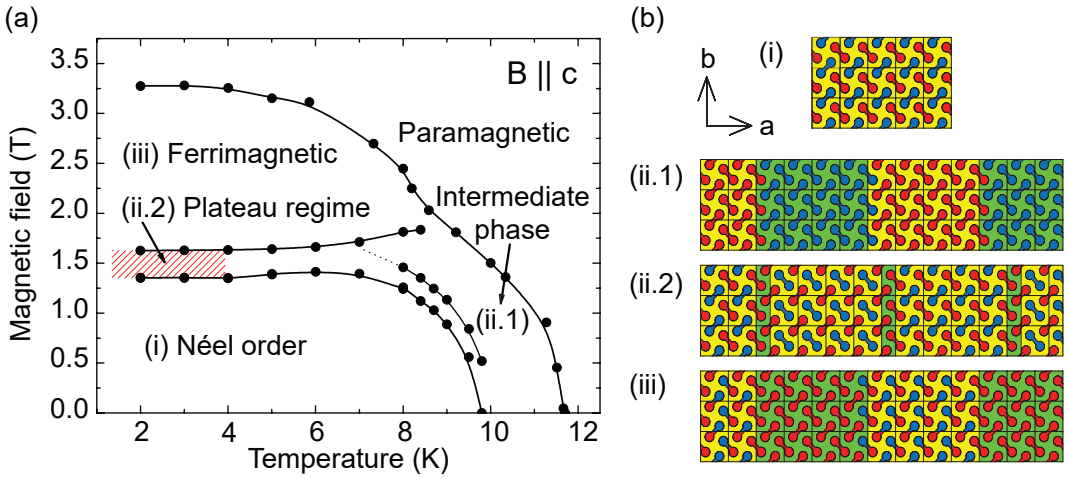

Figure 2.2.3.: Magnetic ordering in TmB_4. (a) Phase diagram of TmB_4 as a function of field and temperature. It was derived from magnetization data for $B||(001)$. (b) Orientation of the Ising-spins in the ab-plane in TmB_4. Spin up and down along the c-axis are presented as red and blue circles. The periodicity of the magnetic domains along the a-axis are indicated with different surface colours. The labeling in (a) and (b) correspond to each other. Adopted from [24].

The magnetic Tm^{3+} ions have a 4f configuration and an angular momentum $J = 6$. Crystal field effects occur at Tm^{3+} sites. These crystal field effects lift the degeneracy of the $J = 6$ multiplet. This lifted degeneracy leads to a doublet $M_J = \pm 6$ ground state. Due to this

ground state a strong Ising-like magnetic anisotropy is induced. The magnetic moments of the Tm ions point in c-direction within the Néel phase below $T_N = 11.8$ K. In this antiferromagnetic phase, a saturated magnetization is reached at ≈ 4 T, if the magnetic field is applied parallel to c-direction of the crystal. Here, also magnetization plateaus occur at a fraction of saturation magnetization, which are attributed to the large spin degeneracy in TmB_4. The stable plateaus appear at $M/M_{sat} = 1/2$ and the fractional plateaus at $M/M_{sat} = 1/7, 1/8,$ etc.. These plateaus also appear at the magnetization of a 2D degenerate electron gas. In TmB_4 also hysteretic longitudinal magneto-resistance, anomalous Hall resistivity as well as a rich phase diagram are found. If the magnetic field is applied perpendicular to the c-direction, the magnetization saturation is not reached until a magnetic field of 30 T is applied.

The rich phase diagram as a function of magnetic field and temperature and the magnetic structure of Ising spins in the ab-plane are shown in Fig. 2.2.3 (a) and (b), respectively. With no magnetic field applied TmB_4 orders magnetically below $T_N = 11.8$ K. Full antiferromagnetism [Fig. 2.2.3 (b-i)] is observed below $T_N = 9.8$ K [Fig. 2.2.3 (a-i)]. Besides these two ordered states, three other phases were found. Below temperatures of ≈ 8 K and an applied field of $B \approx 3.6$ T the order is ferrimagnetic [Fig. 2.2.3 (a-iii) and (b-iii)]. There, a plateau at $M/M_{sat} = 1/2$ can be identified. The main portion of the plateau regime [Fig. 2.2.3 (a-ii.2)] with magnetization plateaus at $M/M_{sat} = 1/7, 1/8, 1/9, ...$ below 4 K, which are hysteretic, is located below ≈ 1.6 T and at temperatures between $0 - 7$ K. The Plateau regime [Fig. 2.2.3 (a-ii.2)] shows a long range antiferromagnetic order intercalated with small stripes of ferromagnetic order [Fig. 2.2.3 (b-ii.2)]. The intermediate phase [Fig. 2.2.3 (a-ii.1)] at temperatures ranging from $7 - 11.8$ K orders ferromagnetically in the short range regime and antiferromagnetically in the long range regime [Fig. 2.2.3 (b-ii.1)]. Once the ferrimagnetic phase was reached, the zero field cooling plateaus are independent of both the magnetic field direction and the magnetic field changes. Close to $T_N = 9.8$ K the intermediate state splits into two phases, which was found in specific heat and resistivity measurements.

According to Orendáč *et al*. TmB_4 shows a magnetocaloric effect (MCE) as well as a rotating magnetocaloric effect (R-MCE). If the applied magnetic field is increased, the magnetic moments align parallel to the direction of the field. This alignment leads to a decrease of the magnetic entropy. For adiabatic conditions the energy of the system stays constant, and therefore the lattice entropy increases, which leads to a heating by a temperature ΔT. The magnetization in TmB_4 for fields parallel to the c-direction is much higher up to 4 T compared to the magnetization perpendicular to the c-direction, which can be beneficial for the emergence of the R-MCE. The magnetocaloric effect describes a magneto-thermodynamic phenomenon. The change of the orientation of an external applied magnetic field changes the temperature of the material. This phenomenon can be enhanced and intensified by geometrical spin frustration, which is found in TmB_4.

Fig. 2.2.4 shows the distribution of the temperature difference $\Delta T(T, B)$. The strongest

cooling effect occurs above 4 T at temperatures around ≈ 20 K, while the sample heats up as much as $5 - 10$ K, if a magnetic field of more than 3.5 T is applied. The strongest R-MCE is detected when the sample is rotated by $90°$ or $270°$.

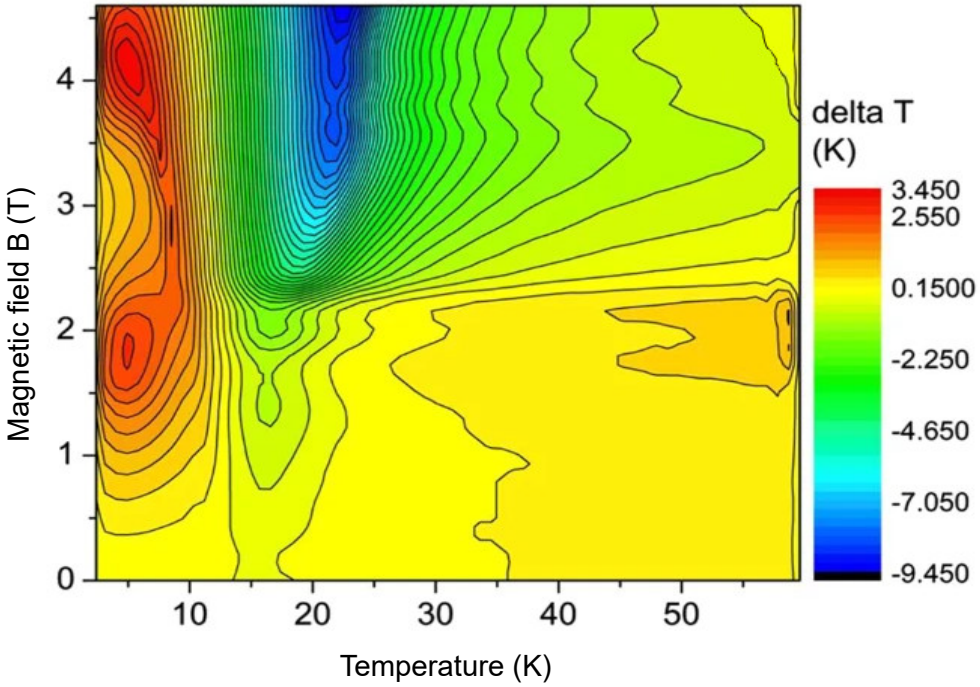

Figure 2.2.4.: Distribution of the temperature difference $\Delta T(T, B)$ due to the magnetocaloric effect in TmB_4 during rotation from B $\parallel$ c to B $\perp$ c. Taken from [25].

3. Raman Scattering

This chapter introduces Raman spectroscopy as the main experimental method of this thesis. A more detailed description for Raman spectroscopy can be found in Ref. [77].

3.1. Theory of Raman Scattering

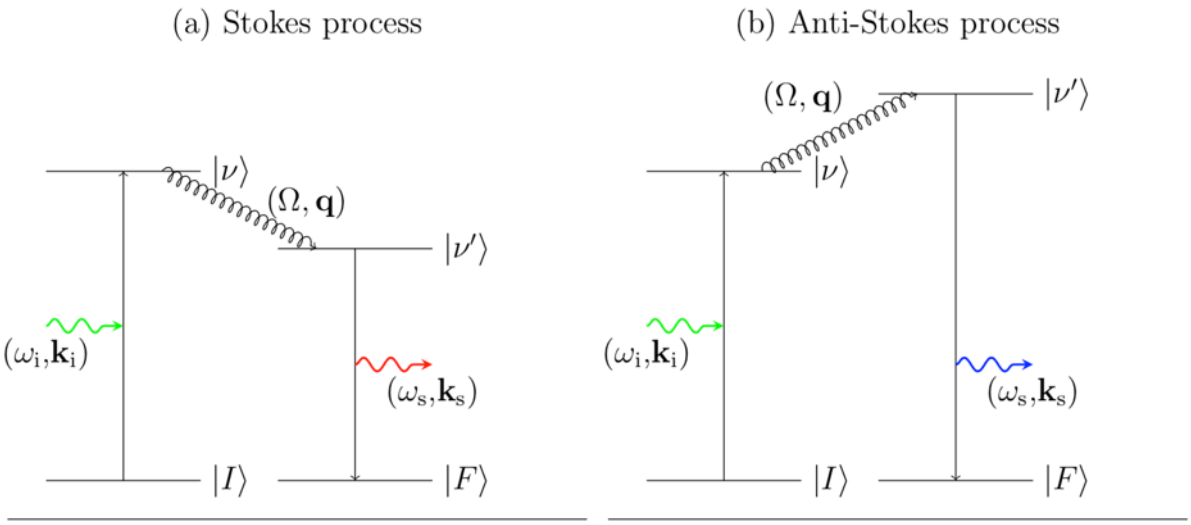

Figure 3.1.1.: Simplified scheme of a Raman scattering process. The incident photon $(\omega_i, \mathbf{k}_i)$ (green wavy line) excites the system from its initial state $|I\rangle$ to an intermediate state $|\nu\rangle$. By either (a) creating or (b) destroying an excitation $(\Omega, \mathbf{q})$ (curled line) the system makes a transition to a second intermediate state $|\nu'\rangle$, and relaxes to its final state $|F\rangle$ by emission of a (a) red- or (b) blue-shifted photon $(\omega_s, \mathbf{k}_s)$ [78]. Taken from [79].

Smekal predicted the inelastic scattering of visible light from matter in 1923 [80], the so-called Raman scattering. Raman and Krishnan discovered Raman scattering in liquids experimentally in 1928 [81] and, in the same year, it was also discovered in crystals by Landsberg and Mandelstam [82].

In Fig. 3.1.1 the principle of Raman scattering is illustrated. First, in a scattering event a photon of energy ω_i and momentum $\mathbf{k}_i$ is absorbed. This photon excites the system from the initial state $|I\rangle$ to an intermediate state $|\nu\rangle$, which can now couple to low energy excitations such as e.g. phonons or magnons. This coupling destroys or creates an excitation with energy Ω. Thus the system reaches a second intermediate state $|\nu'\rangle$, before it emits another photon with energy ω_s and momentum $\mathbf{k}_s$ before relaxing to its final state $|F\rangle$. The

energy difference between the incident and the emitted photon is called Raman shift Ω. It corresponds to the energy transferred to or from the material.

$$\Omega = \omega_\mathrm{i} - \omega_\mathrm{s} \tag{3.1}$$

If an excitation is created, the process is called Stokes process, which is shown in Fig. 3.1.1 (a). In this process, the energy of the incident photon is larger than the energy of the emitted photon. In the opposite case, if the emitted photon energy is larger than the energy of the incident photon, the process is called anti-Stokes process (Fig. 3.1.1 (b)). In both cases the transferred momentum $\mathbf{q}$ can be considered small, putting Raman scattering in the limit $|\mathbf{q}| = 0$. Anti-Stokes processes vanish at $T = 0$

Every scattering process involves two dipole transitions $|I\rangle \rightarrow |\nu\rangle$ and $|\nu'\rangle \rightarrow |F\rangle$. These transitions and the symmetry of the crystal are the basis for the Raman selection rules.

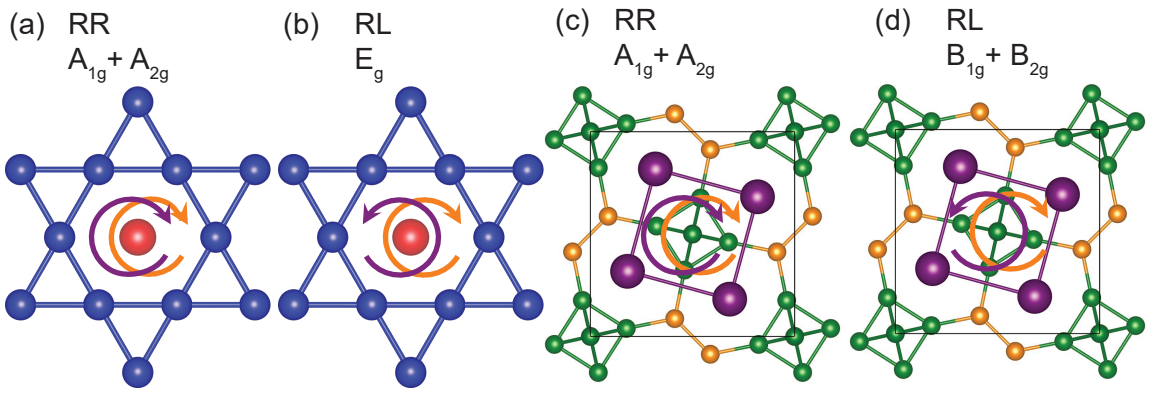

Figure 3.1.2.: Selection rules of Raman scattering in Kagome lattice materials [(a) and (b)] and the Tetraboride TmB_4 [(c) and (d)]. The orange and the purple arrows denote the polarizations of the incident and the scattered light, respectively. Here, only circular polarizations are shown. For individual symmetries seperately at least one (a) and (b) or two (c) and (d) additional configurations are necessary.

As shown in Fig. 3.1.2, every set of polarizations $(\mathbf{e}_\mathrm{i}, \mathbf{e}_\mathrm{s})$ of the incident (orange arrow) and scattered (purple arrow) light projects different symmetries. Each symmetry can be extracted as a linear combination of spectra. The relevant coordinate system for the selection rules in Kagome materials is given by the Kagome net and in the Tetraboride TmB_4 is given by the tetragonal unit cell. As will be shown experimentally below, the A_{2g} symmetry can be neglected in both Kagome and Tetraboride material classes. Only RR- and RL-polarization combinations were used in the measurements for this thesis. Therefore only contributions stemming from A_{1g} and E_g pictured in Fig. 3.1.2 (a) and (b), respectively, are relevant for Kagome lattice materials. The relevant contributions of the Tetraboride TmB_4 stem from A_{1g} and $B_{1g} + B_{2g}$ pictured in Fig. 3.1.2 (c) and (d), respectively.

In general, both intermediate states $|\nu\rangle$ and $|\nu'\rangle$ are virtual states. They exist within time and energy uncertainty, but they can also be eigenstates of the system. In this case, the scattering intensity diverges as the energy denominator (in perturbation theory) becomes

zero [83]. This effect is called resonance and provides a probe to the electronic structure of the material [78, 79].

3.2. Raman Features

Raman scattering is a method, which is very sensitive to detect various excitations and their possible changes. Therefore, Raman spectra show the superposition of various excitations at their corresponding energies [26]. Some Raman features, which are important for this thesis, are shown schematically in Fig. 3.2.1.

Fig. 3.2.1 (a) shows a schematic plot of spectra typical for particle-hole excitations, which are visible in most Raman measurements of metals. This electronic continuum of a correlated metal [1] can be described phenomenologically by Eq. 3.2, where $a,\ b,\ c$ and d are adjustable parameters,

$$\chi''(\Omega) = a\ \tanh(b + c \cdot \Omega) + d. \tag{3.2}$$

The Raman response of other excitations is superimposed on this continuum. One type of excitations are phonons, whose Raman response is marked by two asterisks. Phonons typically have a width of only a few wavenumbers and a symmetric shape, which can be represented by a Voigt function due to the Lorentz-distribution of the excitation response itself and the Gaussian-distribution caused by the resolution of the spectrometer. Taking a look at phonons and how they change in energy and linewidth can provide information about changes in the lattice, the symmetries of the crystal or, for instance magnetic ordering phenomena.

Peierls considered the case of a linear chain with just one electron per unit cell (half filling) [84]. Then the energy may be reduced if two unit cells dimerize (the new superlattice contains not only one but two atoms) and the elastic energy required for the distortion is smaller than the energy gain from the opening of a gap at the Fermi level. The modulation is called a charge density wave (CDW). Fig. 3.2.1 (b) shows the typical Raman response of an opening gap of the charge density wave (CDW) below T_{CDW}, which consists of a redistribution of spectral weight [85, 86]. The asterisk marks the approximate position of the CDW gap [26].

Magnetism can arise from localized or from itinerant electrons. Fig. 3.2.1 (c) and (d) show exemplary Raman spectra. The driving force for magnetism in La_2CuO_4 is the exchange interaction J between localized electrons. The corresponding Raman response is characterized by a two-magnon peak. This peak hardens upon cooling [87]. In the metallic material $BaFe_2As_2$ magnetism arises from itinerant electrons and therefore, the Raman response has a different shape. The spectrum at $T = 300$ K is described by particle-hole excitations with superimposed phonons [88, 89]. At 130 and 50 K (blue and black lines, respectively), below

[1] where the relaxation of the electrons follows approximately $\Gamma \propto k_B T + \hbar\omega$ (marginal Fermi liquid) as opposed to $\Gamma \propto (k_B T)^2 + (\hbar\omega)^2$ in the Landau-Fermi liquid.

the spin density wave critical temperature T_{SDW} a gap evolves at low energies and spectral weight gain occurs at higher energies. This behaviour is typical for spin *and* charge density waves.

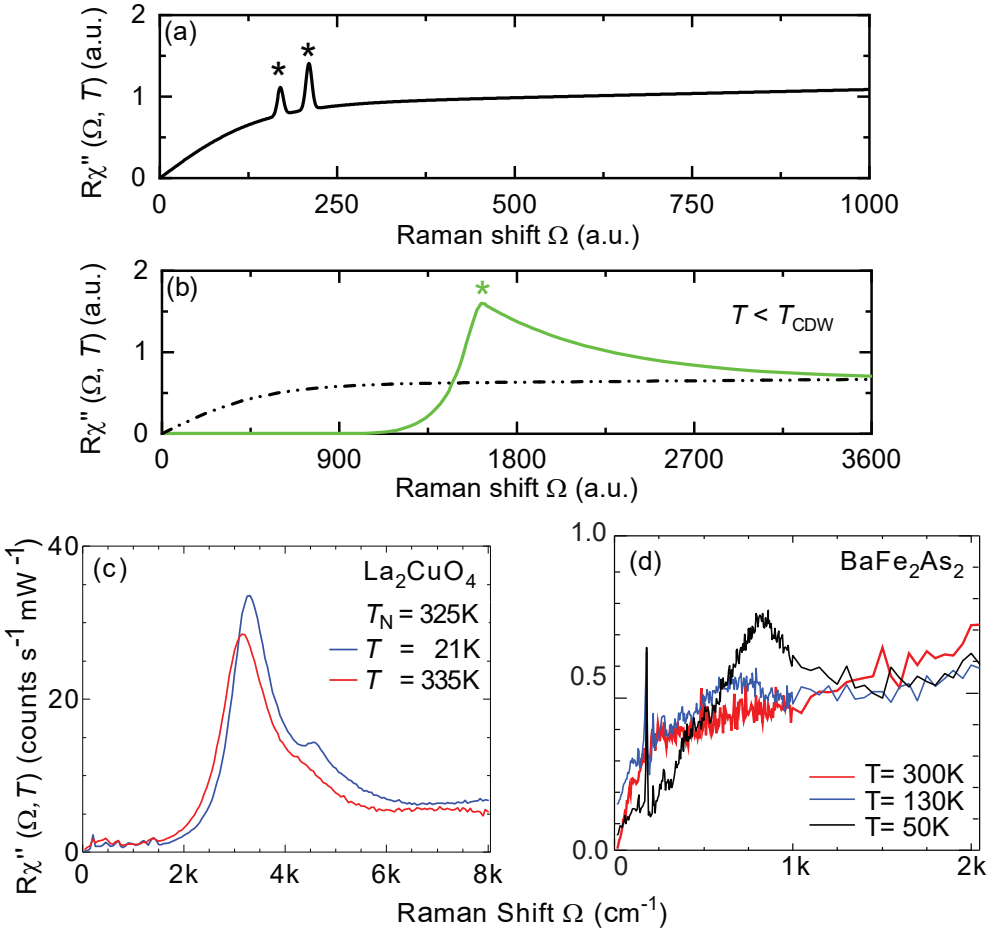

Figure 3.2.1.: Schematic spectra observed with Raman spectroscopy. (a) The black curve corresponds to a phenomenological description of the particle-hole (p-h) continuum. The two modes marked by the asterisks are phonon modes superimposed on the p-h continuum [26]. (b) The dashed line represents the p-h continuum for $T > T_{CDW}$. The gap of the CDW phase opening for $T < T_{CDW}$ redistributes the spectral weight (green). The spectrum has its maximum (green asterisk) at approximately $2\Delta_{CDW}$ [26]. (c) Raman spectra in B_{1g} symmetry of La_2CuO_4. Since La_2CuO_4 hosts localized magnetic order, the Raman spectra are dominated by a two-magnon peak, which hardens upon reducing temperature [87]. (d) Raman spectra in B_{1g} symmetry of $BaFe_2As_2$ hosting itinerant electrons. The spectrum at room temperature $T = 300$ K does not exhibit abrupt changes in the detected light intensity. For $T < T_{SDW} = 135$ K a gap opens and weight is redistributed [88, 89].

3.3. Intensity Calibration

A short overview of the intensity calibration in both laboratories "Raman I" and "Raman II" is given in this subsection.

3.3.1. Laboratory "Raman I"

Experimentally, the count rate $\dot{N}_{is}$ of detected photons is measured for a certain wavelength of the scattered light, which corresponds to a certain Raman shift Ω. The physical property of interest is the susceptibility χ'', which can be calculated using Eq. 3.3.

$$R\chi''_{is}(\Omega, T) = \frac{\dot{N}_{is}}{P_\mathrm{i} \cdot s(\omega_\mathrm{s})} \frac{\omega_\mathrm{i}^2}{\omega_\mathrm{s}\tilde{\omega}} \left[1 - \exp\left(-\frac{\hbar\Omega}{k_\mathrm{B}T}\right)\right] \tag{3.3}$$

In Eq. 3.3 ω_i and ω_s are the energies of the incident and the scattered photons, P_i is the absorbed laser power of the incident light and the constant R includes temperature- and energy-independent factors. $\tilde{\omega} = 20000$ is used to keep the corrections close to one for visible incoming photons. The instrument has an energy-dependent sensitivity $s(\omega_\mathrm{s})$ which becomes relevant if spectra are measured in large energy ranges. Therefore, one needs to correct the data to calculate χ'' properly. This sensitivity was determined by calibration [90]. The expression in the square brackets results from the fluctuation-dissipation theorem. In Refs. [77] and [78] a more detailed description can be found [79].

3.3.2. Laboratory "Raman II"

As already mentioned in Sec. 3.3.1 measurements of the Raman scattered light over a wide energy range require energy dependent corrections with respect to the sensitivity of the setup $s(\omega)$ according to Eq. 3.3. Therefore, also a sensitivity curve for the setup of the laboratory "Raman II" is required. To get this sensitivity curve, the transmission of the spectrometer with the 1800 gr/mm gratings and the quantum efficiency (QE) of the CCD need to be determined. In addition the spectral resolution as a function of the grating angle is required. In Ref. [91] a more detailed description of the whole process can be found.

The transmission of the spectrometer can be determined the following way: The laser beam is directed through the spectrometer. The spectrometer's gratings must be set to -1^{st} order, while the light has to be polarized parallel to their dispersion direction (perpendicular to the grooves). The laser beam exits at the monochannel exit after the third monochromator. To get the transmission, the ratio of the laser power right in front of the entrance slit and after the monochannel exit needs to be calculated. This ratio is determined for all available laser lines of the Krypton ion laser and the green Nd-YAG diode-pumped solid state laser (Fig. 3.3.1 (a)). It reaches a maximum in the green range of the laser beam and drops rapidly towards both shorter and longer wavelengths.

The quantum efficiency of the CCD on the other hand is determined by directing the beam directly on the CCD. The intensity is then measured by the detector. Since the CCD is very sensitive, an overflow of the detector needs to be avoided. Therefore, the beam needs to be attenuated sufficiently to keep the number of registered counts below the maximum capacity of the analog-to-digital converter ($2^{16} = 65536$ counts) with the use of neutral density (ND) filters. The optical density of the ND filters also depends on the wavelength and hence needs to be measured by measuring their transmission using a power meter

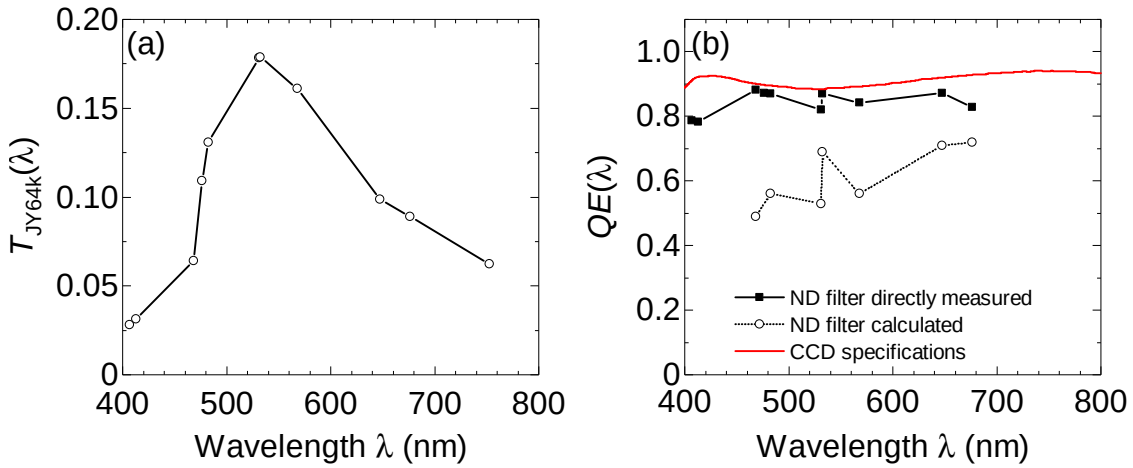

Figure 3.3.1.: Optical sensitivity of the setup in the laboratory "Raman II". (a) Transmission through the Jobin-Yvon T64000 spectrometer as a function of wavelength. (b) Quantum efficiency (QE) of the Jobin-Yvon Symphony II CCD as a function of wavelength. The QE is determined experimentally by using neutral density (ND) filters with method 1 (black circles) and method 2 (white circles). The red curve is the QE taken from the CCD's datasheet. In addition the spectral resolution as a function of the grating angle is required. Taken from [79].

(method 1). Another method (method 2) to get the quantum efficiency of the CCD is the usage of different combinations of ND filters for measuring the intensity of the beam on the CCD. To obtain the OD and the QE a set of equations [91] needs to be solved. The results obtained with both methods are pictured in Fig. 3.3.1 (b) together with the QE as given in the CCD's datasheet. The QE determined with method 1 (black circles) agrees reasonably well with the specifications (red line) of the CCD. The QE determined with method 2 is much lower and varies strongly over the whole measured range (white circles) [79].

4. Experimental Setup

The measurements performed in this thesis using the Raman spectroscopy setups in the laboratories "Raman I" and "Raman II". Both setups will be described in this chapter.

4.1. Laboratory "Raman I"

4.1.1. Scattering Setup

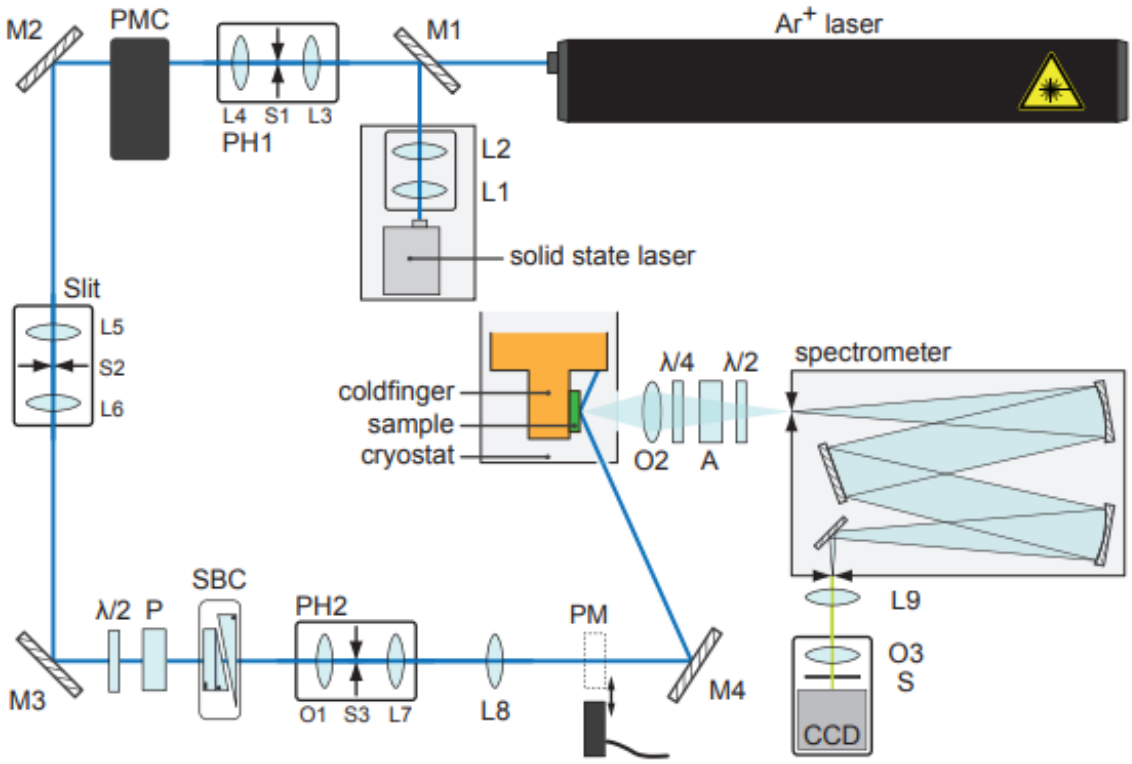

Figure 4.1.1.: Setup in the laboratory "Raman I" for Raman spectroscopy. Mirrors are marked with M, lenses with L, objectives with O and slits with S. The numbering index of the components rise by 1 with respect to their position to the light source. The two pinhole systems are labeled with PH1 and PH2 [26, 92].

The Setup of the laboratory "Raman I" is shown in Fig. 4.1.1. The setup for Raman spectroscopy consists of a source of monochromatic polarized (P) light. Either a yellow solid state laser (Coherent-Genesis MXSLM), which emits light with a wavelength of 575 nm or an ion laser (Coherent Innova 300C), which provides five lines in the range from 458 nm to 514 nm, is used. The beam, shown as a blue line, is expanded using a lens system (L1, L2).

Afterwards it gets filtered spatially by the pinhole system (PH1) to remove off-axis contributions. To suppress plasma lines of the laser beam, the prism monochromator (PMC) and the following slit system (L5, S2, L6) act as a single-stage spectrometer. Since the laser light is already polarized, the $\lambda/2$-plate can be rotated to set the desired laser power for the experiment. The laser power is determined using a power meter (PM) before and after every measurement to ensure the comparability of the different measurements. The combination of the polarizer (P) and the Soleil-Babinet compensator (SBC) enables the generation of any polarization of the incident light via the variable phase shift between ordinary and extraordinary direction in the compensator. Afterwards the beam gets filtered spatially again by the second pinhole system (PH2) and is focused to a spot of roughly 50 x 100 μm^2 onto the sample using a lens (L8) and a mirror (M4) on a kinetic mount, which can be tilted in along two axes to position the laser spot on the sample surface. The angle of incidence is $\theta_i = 66°$.

After the light was focused onto the sample an objective (O2) collects the scattered light. The polarization of the scattered light is selected using a $\lambda/4$-retardation plate and a polarizer/analyzer (A). A second $\lambda/2$-plate rotates the polarization of the scattered light into the direction of highest sensitivity of the spectrometer. The light is focused on the entrance slit (SL1) of the spectrometer (Jarrell-Ash 25-100 double monochromator equipped with 2400 gr/mm gratings). The spectrometer selects a frequency band the width of which can be determined by the slit between the two subtractively coupled monochromators. The resolution of the spectrometer, which operates in subtractive mode is given by the width M of the intermediate slit (SL2). The absolute wavelength of the transmitted light is chosen by the rotation angle of the gratings. Afterwards the transmitted light is focused onto the CCD detector by a lens (L9) and an objective (O3).

The sample is mounted on a cold finger inside a continuous-flow ^{4}He-cryostat, which can be set to temperatures in the range of 4.2 K to 350 K. To assure a steady temperature, a heater controlled by a temperature controller and a silicon diode near the sample holder are built in. The sample stage of the cryostat is evacuated to pressures below $2 \cdot 10^{-6}$ mbar to reduce the contamination of the sample surface [26, 78].

4.1.2. Optical Constants

The Raman selection rules introduced in Section 3.1 require a precise setting of the light polarization and absorbed power of the sample.

Due to the complex index of refraction of a metal $\tilde{n} = n + ik$ the light polarization inside the sample is elliptical in general except for normal incidence and polarization parallel or perpendicular to the plane of incidence. Here the angles of incidence are $\theta_i = 66°$ and the desired polarization inside the sample may be circular or at $45°$ with respect to the plane of incidence. This condition which determines the selection rules requires the appropriate polarization outside the sample to be determined individually by applying the Fresnel formulae due to the angle of incidence $\theta_i = 66°$ in laboratory "Raman I" and $\theta_i = 30°$ in

laboratory "Raman II" the polarization inside the sample differs from the polarization of the incident beam in the setup used here. Similarly the propagation direction of light inside the sample depends on the index of refraction n of the sample according to the Fresnel equations. Therefore, $\tilde{n} = n + ik$ was determined for each sample by ellipsometry. The correct polarization inside the sample and the power factor between the incident and the absorbed light can be calculated based on $\tilde{n}$. More detailed information can be found in Refs. [93] and [94][78].

4.2. Laboratory "Raman II"

4.2.1. Scattering Setup

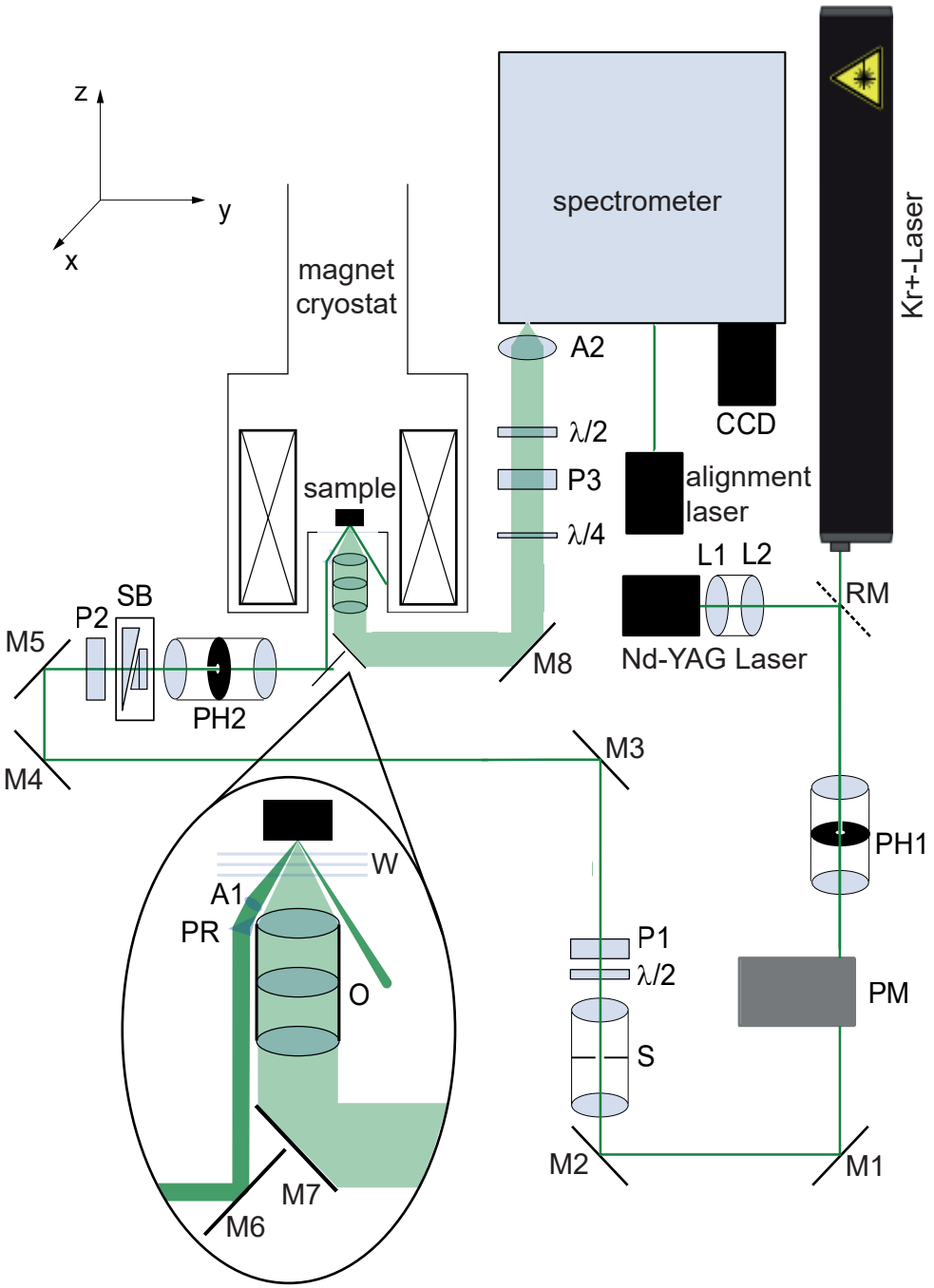

Figure 4.2.1.: Experimental setup and beam path in the laboratory "Raman II". Mirrors are marked with M, lenses with L, objectives with O, polarizers with P and the pinhole systems with PH. The numbering index of the components rise by 1 with respect to their position to the light source. Adapted from [95].

The setup of the laboratory "Raman II" is shown schematically in Fig. 4.2.1. Here, either a Krypton ion laser (Coherent Sabre Innova), which emits laser light with different wavelengths in the range of 406.7 nm and 799.3 nm or a green Nd-YAG diode-pumped solid state laser (Coherent Sapphire) emitting light with a wavelength of 532 nm were used as a light source. To switch between the solid state laser and the ion laser a mirror (RM) needs to be removed or added to the beam path. The light emitted by the chosen laser is initally filtered spatially and expanded in diameter by a lens system (PH1). The system consists of a microscope objective, which focuses the beam onto a pinhole, and a lens, which makes the beam parallel after the pinhole.

Afterwards a prism monochromator (PM) disperses the laser light and the following lens focuses the beam on a slit (S), so just monochromatic light of a selected wavelength can pass. A $\lambda/2$-plate in combination with a polarizer (P1) is used to reduce the power of the pre-polarized laser light. The polarization of the incident light is selected by a polarizer (P2) and a Soleil-Babinet compensator. This compensator consists of wedge-shaped crystals, which can be rotated and shifted against each other to adjust the relative phases of the ordinary and the extraordinary beams. Then, the beam is directed by a mirror (M6) and a prism (PR) onto the sample with an angle of incidence $\theta_i = 30°$ and is finally focused onto the sample surface with an achromat (A1) into warm bore of a solenoid superconducting magnet providing fields up to 7.5 T. A schematic drawing and an actual picture of these optical components in the bore of the cryostat are shown in Fig. 4.2.2. Since the angle of incidence is $\theta_i = 30°$, the absorption coefficients for light polarized parallel or perpendicular to the plane of incidence are different. As the incoming light is focused on the sample surface at an non-zero angle, for example circularly polarized light, assumes an elliptical polarization inside the sample. This problem can be solved with the compensator (SB). It polarizes the light elliptically outside the sample such that the absorbed light is circularly polarized inside. Therefore the complex index of refraction needs to be known and experimentally determined for every sample and excitation wavelength, as already mentioned in Section 4.1.2. Since the incidence angle of the photons reflected from the sample surface is larger than the aperture angle of the objective lens (O), they cannot enter the collection optics. The collection optics consist of a custom-made objective lens with a numerical aperture of $NA = 0.34$ $(19.5°)$. The lens corrects optical aberrations introduced by the cryostat windows (W). The z-axis points in a positive direction to the ceiling, which means it perpendicular to the cryostat. The y-axis runs parallel to the optical axis below the cryostat and the x-axis is derived from the right hand rule. The magnetic field always points in the z-direction. Before entering the spectrometer the desired polarization of the scattered light is selected with a $\lambda/4$-plate and an analyzer (P3). The spectrometer is most sensitive in the vertical direction, so a $\lambda/2$-plate rotates the light polarization into the vertical direction. A triple-stage spectrometer (Jobin-Yvon T64000) in combination with a liquid nitrogen cooled charge coupled device (CCD, Jobin-Yvon Symphony II) is used to spectrally analyze the scattered light.

The sample is mounted on a sample holder made out of copper at the end of a dipstick and is built into the He flow magnet cryostat. This allows the sample to be exposed to a magnetic field of up to 7.5 T in a temperature range of $1.8 - 330$ K. The orientation of the sample in the applied magnetic field can be controlled by tilting and rotating the sample manipulator. The sample is in thermal contact with the sample holder. A Cernox resistor is used to determine the temperature near the sample [27, 95–97].

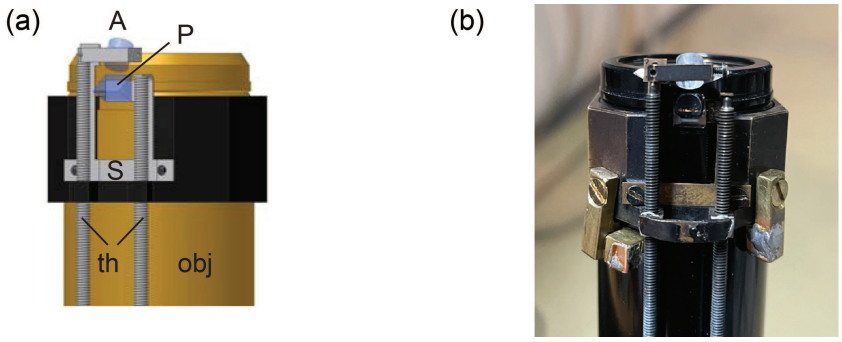

Figure 4.2.2.: Drawing (a) and photograph (b) of the optics in the bore of the magnet cryostat, which are focusing the laser on the sample. The objective (obj) collects the scattered light. With threaded rods (th), which are pushing against springs (S), the position of both the achromat (A) and the prism (P) can be adjusted separately. Adapted from [27].

4.2.2. Sample Orientation in the Magnetic Field

To observe the magneto-caloric effect in the Tetraboride TmB_4 a magnetic field parallel and perpendicular to the sample surface needs to be applied. Thus, the sample needs to be tilted by $90°$ with the manipulator. Fig. 4.2.3 shows both the sample holder and the sample manipulator at the lower end of the sample rod in the laboratory "Raman II". The sample on the sample holder can be rotated or tilted vertically and parallel to the sample surface. If the sample is aligned horizontally, which means the surface is perpendicular to the z-axis of the cryostat, the incoming laser beam and the scattered light irradiate directly onto the sample. If the sample is vertically orientated, which means the surface is parallel to the z-axis, an additional mechanically foldable mirror is needed to direct the excitation laser onto the sample. Analogously the scattered light is also directed back into the objective via this mirror. The mirror is not visible in Fig. 4.2.3, because it is hidden by the tilting mechanism.

The Faraday rotation needs to be taken into account for measurements in a magnetic field. If polarized light propagates parallel to a magnetic field in a dielectric, the Faraday rotation causes a rotation of the light polarization which is proportional to the magnetic field strength. Due to their position in the warm bore hole of the cryostat the prism (P), the achromat (A1), the cryostat window (W) and the objective lens (O) (Fig. 4.2.1) are all exposed to the magnetic field. Hence both the incident and the scattered light experience a Faraday rotation of their polarization. The rotation for the incident light is $1.2°/T$ and for the scattered light $8.7°/T$. In order to obtain the desired light polarization, the settings of

the polarizer (P2) and the compensator (SB) on the side of the incident light and the $\lambda/4$-delay plate, the polarizer (P3) and the $\lambda/2$-plate on the side of the scattered light must be adjusted accordingly [95].

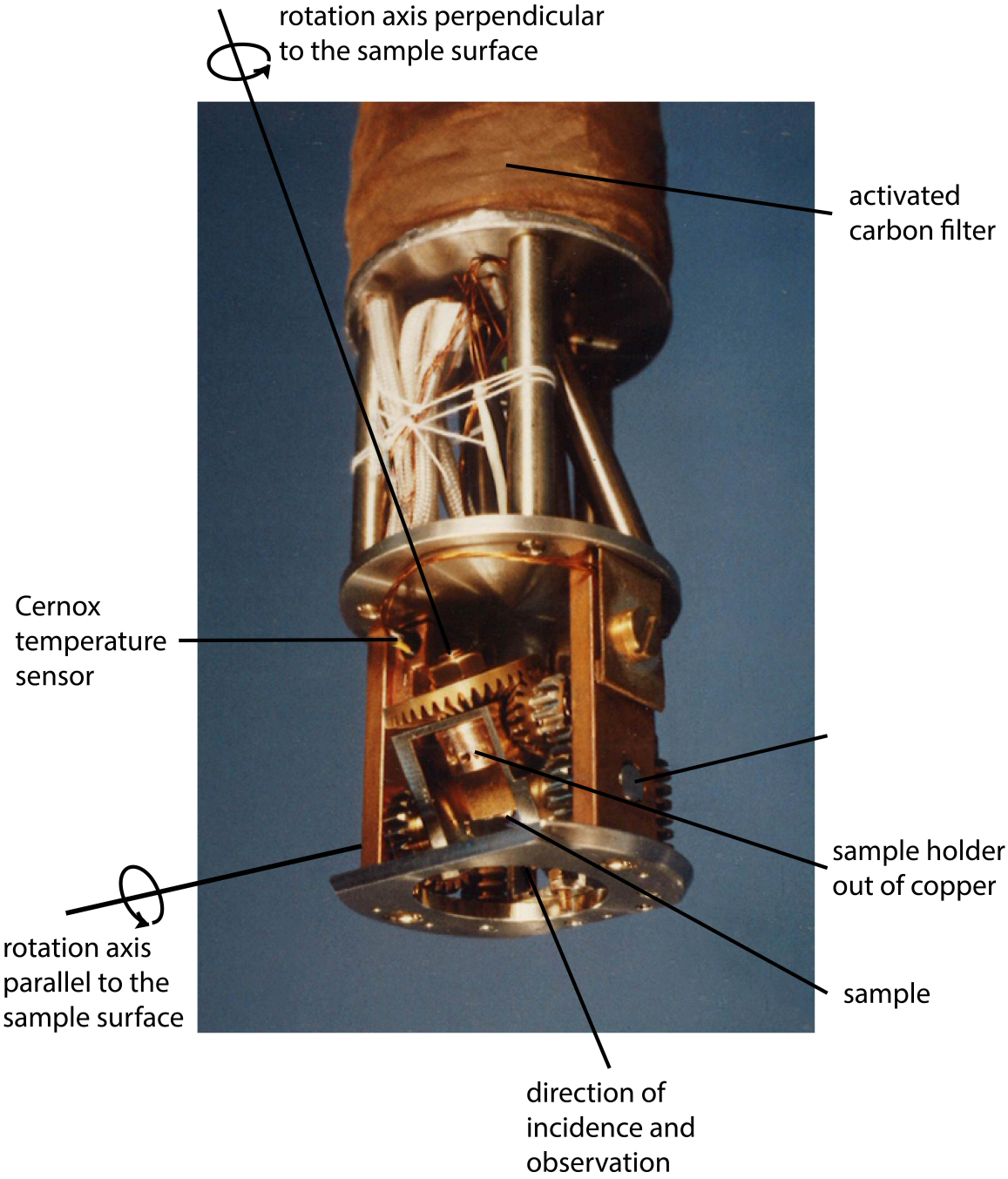

Figure 4.2.3.: The sample manipulator is located at the lower end of the sample stick. The rotation axis of the device parallel to the sample surface as well as the rotation axis perpendicular to the sample intersect in the sample. The sample is in thermal contact with the sample holder made out of copper. Adapted from [95, 97].

4.2.3. Determination of the Gaussian Width

To quantitatively analyze symmetric phonon peaks a Voigt-function is needed. The Voigt-function is a convolution of the intrinsic line-width of the phonons or other homogeneously broadened responses (Lorentzian shape) and the setup broadening/spectral resolution of the setup, which has approximately a Gaussian shape (Eq. 4.1). For measurements in the laboratory "Raman I" in a narrow spectral range and for the laser line used ($\lambda = 575$ nm) the resolution is set to the constant value 2.8 cm^{-1}.

$$y(\omega) = y_0 + A \cdot \frac{2 \cdot \ln(2)}{\pi^{3/2}} \cdot \frac{\omega_L}{\omega_G^2} \int_{-\infty}^{\infty} \frac{e^{-t^2}}{\left(\sqrt{\ln(2)} \cdot \frac{\omega_L}{\omega_G}\right)^2 + \left(2\sqrt{\ln(2)} \cdot \frac{\omega - \omega_c}{\omega_G} - t\right)^2} \, dt \qquad (4.1)$$

In order to find a suitable value for the resolution for the "Raman II" laboratory, Raman spectra of the silicon phonon were measured at 20 K in xy-polarization for different second-intermediate slit settings of the triple stage spectrometer (cf. Fig. 4.2.1) and various binning settings of the CCD. The silicon phonon was examined at 20 K, since the intrinsic line width is nearly constant and small here, so only the Gaussian width changes with the changing second-intermediate slit settings and can be investigated.

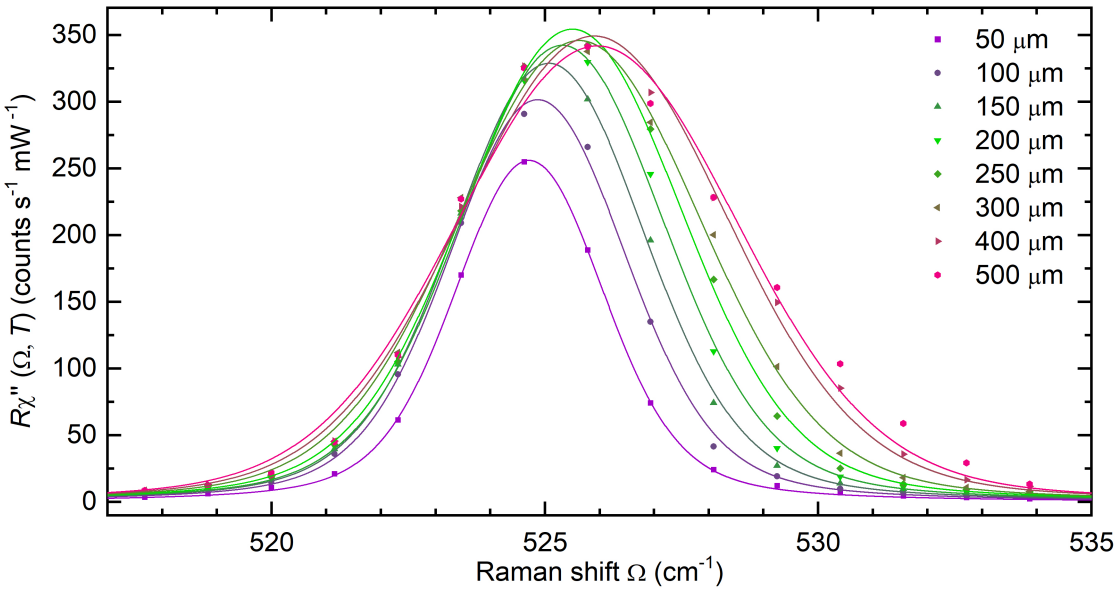

Figure 4.2.4.: The Raman spectra (symbols) of a silicon sample were detected at 20 K with different second intermediate slit widths as indicated in the legend. The data was plotted with the Voigt-function (line), which is a convolution of a Lorentz and a Gauss distribution. The best fitting value of the intrinsic line width ω_L was used for all the spectra.

The measurements of the silicon phonon were then fitted with the Voigt function with a shared intrinsic line width ω_L. The fitting leads to an intrinsic linewidth of $\omega_L \approx 1$ cm^{-1} as the best fit. The data and the corresponding fits of the silicon phonon with binning b $= 2$ are shown in Fig. 4.2.4. For measurements with a second intermediate slit setting between

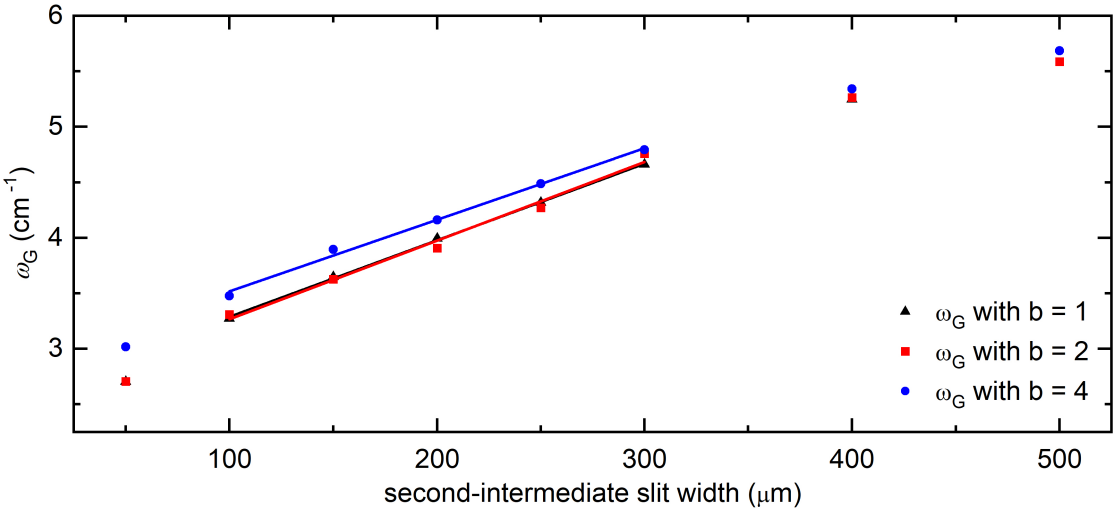

Figure 4.2.5.: The Gaussian widths of the Voigt fits of the Silicon phonon (Fig. 4.2.4) with different binnings of the CCD pixels are fitted linearly. Only the data points with a second intermediate slit width between $100-300$ μm were taken into account for the linear fit. More information can be found in the text.

$100-300$ μm in the spectrometer, the Gaussian width increases linearly with increasing second intermediate slit as shown in Fig. 4.2.5 for all binnings, which agrees to expectations. The data points for 50 μm, 400 μm and 500 μm do not follow this linear regression. The slit cuts into the focus and the slit width determines the Gaussian distribution. If the slit width is now bigger than the spot size, no cutting appears and the curve flattens. The data of the b $= 4$ measurements are a little shifted upwards, which corresponds to the binning distribution for ≥ 100 μm to the Gaussian broadening. The Gaussian width for the measurement setup (second intermediate slit width $= 300$ μm, b $= 2$) can now be determined from Fig. 4.2.5: $\omega_G = 4.7$ cm^{-1}.

5. Experimental Raman Scattering Results

5.1. Kagome Lattice Materials

5.1.1. Fe_3Sn_2

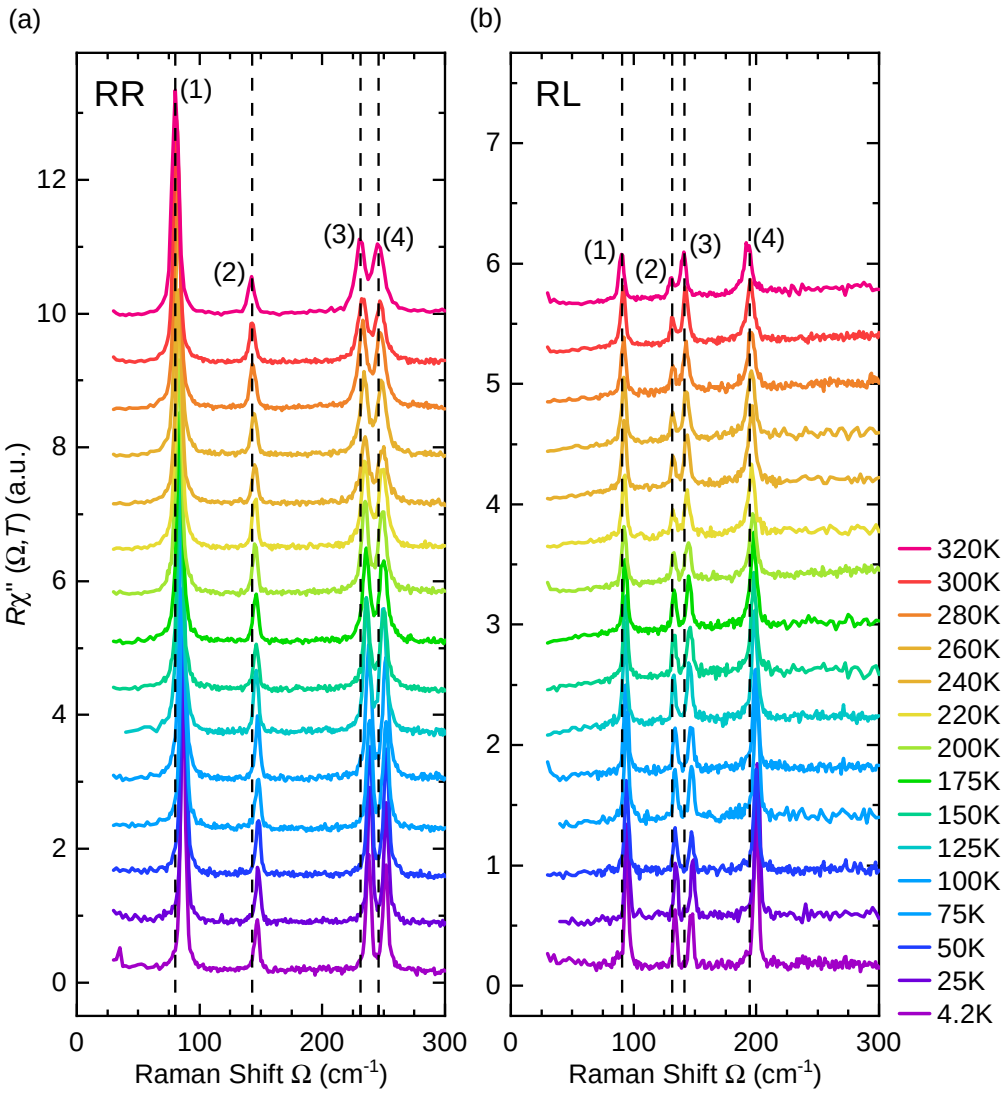

Figure 5.1.1.: Raman spectra of Fe_3Sn_2. Panel (a) and (b) depict the temperature dependence of the eight observed peaks in Fe_3Sn_2 in RR- and RL-polarization, respectively. The spectra at the lowest temperature display the experimentally detected intensity. The A1g spectra are consecutively offset by 0.7 cts/(s mW) and those in Eg symmetry by 0.4 cts/(s mW) each for clarity [17].

Spectra of Fe_3Sn_2 measured in the laboratory "Raman I" are shown in Fig. 5.1.1. The range of the measured Raman shift Ω is from 30 cm^{-1} to 300 cm^{-1} with steps of $\Delta\Omega = 2.5$ cm^{-1} between $\Omega \in [30, 70]$ cm^{-1} and $\Delta\Omega = 1$ cm^{-1} between $\Omega \in [70, 300]$ cm^{-1}. The colour scale on the right indicates the temperatures at the sample holder. Raman spectra were taken in RR- (shown in Fig. 5.1.1 (a)) and RL-polarization (shown in Fig. 5.1.1 (b)) at temperatures ranging between 4.2 K and 320 K. The spectra in Fig. 5.1.1 (a) show clear peaks. At the temperature T = 320 K they are located at 80.4 cm^{-1} (1), 142.2 cm^{-1} (2), 230.8 cm^{-1} (3), and 245.9 cm^{-1} (4). All of them harden continuously with decreasing temperature and get sharper. At T = 4.2 K they are located at 86.6 cm^{-1} (1), 146.8 cm^{-1} (2), 237.7 cm^{-1} (3), and 251.6 cm^{-1} (4). On the other hand the measurements in Fig. 5.1.1 (b) were performed with the polarization "RL". Here, four peaks could be identified. At the temperature T = 320 K the peaks are located at 90.2 cm^{-1} (1), 130.8 cm^{-1} (2), 140.6 cm^{-1} (3), and 193.1 cm^{-1} (4). All peaks harden continuously with decreasing temperature as well especially peak (2) and gain intensity. At T = 4.2 K they are located at 94.3 cm^{-1} (1), 133.8 cm^{-1} (2), 147.0 cm^{-1} (3), and 199.8 cm^{-1} (4). The spectra in RR- and RL-polarization are consecutively offset by 0.7 cts/(s mW) and 0.4 cts/(s mW) for clarity, respectively [17].

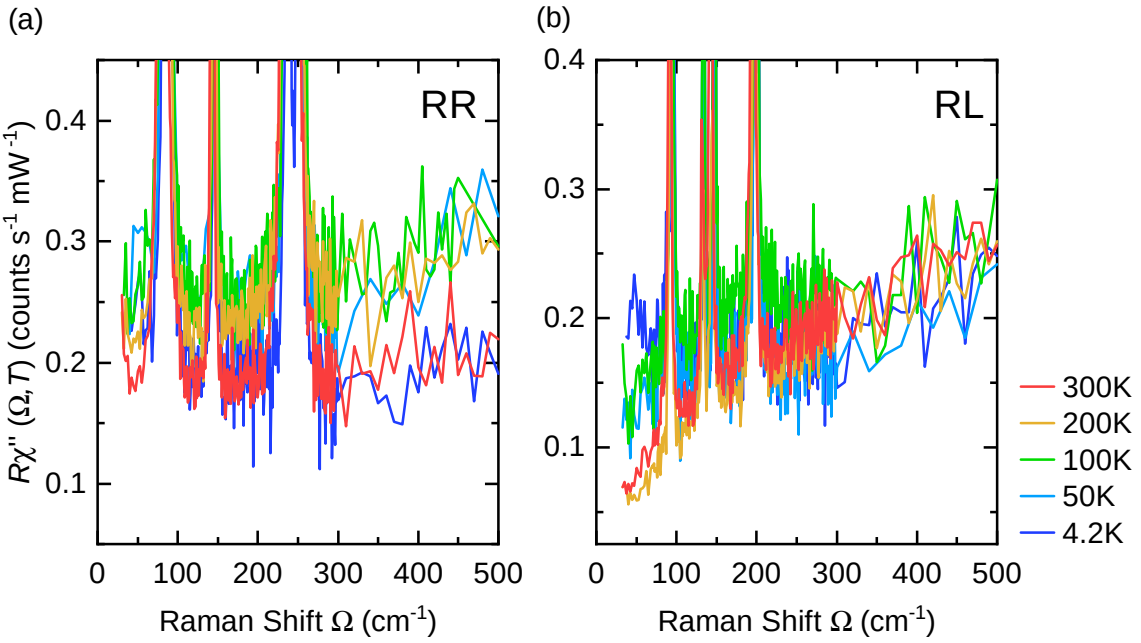

Figure 5.1.2.: Electronic continuum in (a) RR- and (b) RL-polarization at temperatures as indicated. Only the continuum in RL-polarization remains examinable at low temperature, since the spectra in RR-polarization increase too strongly towards low energies due to surface contamination and diffuse elastic scattering from the laser. The increase of the spectra in RL-polarization in the limit $\Omega \to 0$ is a real physical effect since the spectra at 4.2 K have a peak at finite energy and then decrease again as opposed to a laser-induced divergence [17].

To take a closer look at the electronic continuum at low energies, Fig. 5.1.2 shows the spectra from Fig. 5.1.1 zoomed in for the relevant temperatures at the right bottom. Only

the measurements in RL-polarization exhibit a visible temperature dependency, while the spectral weight at low energies in RR-polarization increases to strongly. This stems most likely from surface contamination leading to diffuse elastic scattering of the laser light. Upon cooling from 300 K the initial slope and the spectral weight below 100 cm^{-1} increase and a peak forms at approximately 47 cm^{-1} at 4.2 K. The increase in the limit $\Omega \rightarrow 0$ is a real effect since the spectra at 4.2 K have a peak at finite energy and then decrease again as opposed to a laser-induced divergence [17].

5.1.2. $Co_3Sn_2S_2$

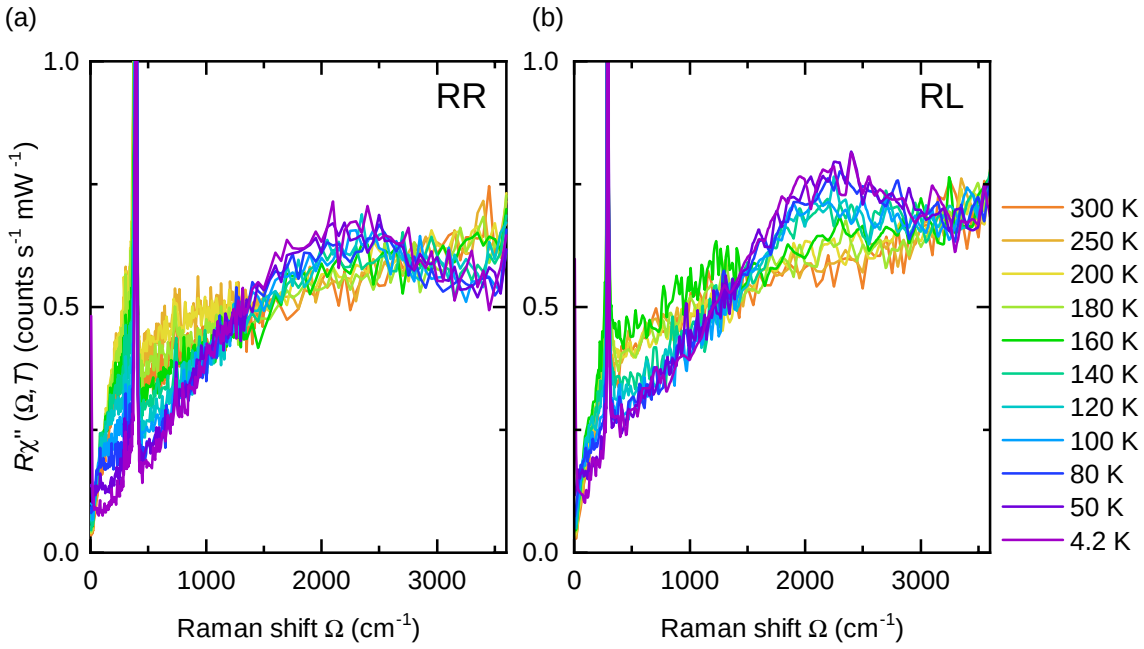

Figure 5.1.3.: Raman spectra in (a) RR- and (b) RL-polarization recorded for various temperatures ranging from 4.2 K – 300 K.

Fig. 5.1.3 (a) and (b) show Raman spectra of $Co_3Sn_2S_2$ measured in the laboratory "Raman I" at temperatures ranging between 4.2 K and 300 K. Measurements were done in a Raman shift Ω range from 5 cm^{-1} to 3600 cm^{-1}. The colour scale on the right displays the temperatures measured at the sample holder. The measurements in Fig. 5.1.3 (a) were performed in RR-polarization with steps of $\Delta\Omega = 5$ cm^{-1} between $\Omega \in [5, 230]$ cm^{-1}, $\Delta\Omega = 2.5\,cm^{-1}$ between $\Omega \in [230, 450]$ cm^{-1}, $\Delta\Omega = 10\,cm^{-1}$ between $\Omega \in [450, 1350]$ cm^{-1}, and $\Delta\Omega = 50$ cm^{-1} between $\Omega \in [1350, 3600]$ cm^{-1}. The measurements in Fig. 5.1.3 (b) were taken in RL-polarization with steps of $\Delta\Omega = 10$ cm^{-1} between $\Omega \in [5, 175]$ cm^{-1}, $\Delta\Omega = 5$ cm^{-1} between $\Omega \in [175, 410]$ cm^{-1}, $\Delta\Omega = 20$ cm^{-1} between $\Omega \in [410, 1410]$ cm^{-1}, and $\Delta\Omega = 50\,cm^{-1}$ between $\Omega \in [1350, 3600]$ cm^{-1}.

The spectra in both RR- and RL-symmetries consist of a continuum with an overlaying peak. In RR-symmetry (Fig. 5.1.3 (a)) the spectrum shows one clear peak with an asym-

metric shape, which hardens and sharpens continuously with decreasing temperature. In RL-symmetry on the other hand, a clear peak with a symmetric shape appears, which hardens and sharpens continuously with decreasing temperature as well. Cooling down from 200 K leads in both spectra to a decrease in the initial slope of the electronic continuum and the spectral weight in the range from 5 cm^{-1} up to 1400 cm^{-1}. At energies above 1400 cm^{-1} the spectral weight increases again, but shows another decrease in spectral weight above 3000 cm^{-1}. The decrease of spectral weight at lower energies is stronger in RR-symmetry compared to RL-symmetry, while the increase of spectral weight at high energies is vice versa. The strong increase at 4.2 K for $\Omega \rightarrow 0$ stems from insufficient suppression of the laser light.

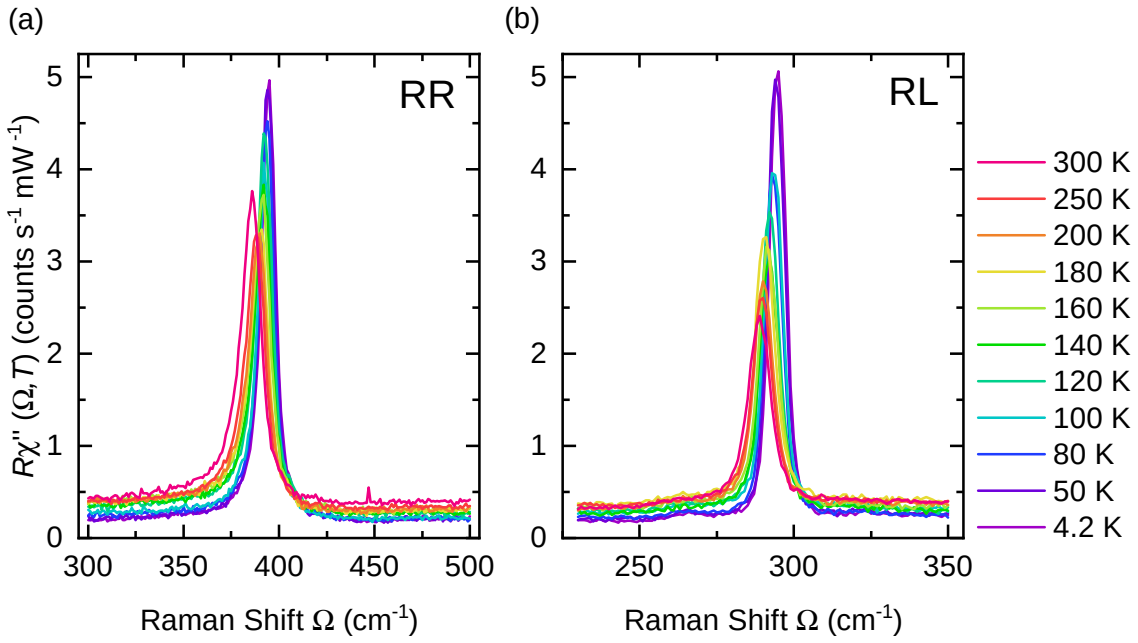

Figure 5.1.4.: Raman spectra in (a) RR- and the (b) RL-polarization at temperatures as indicated in $Co_3Sn_2S_2$.

Fig. 5.1.4 (a) and (b) takes a closer look at the peaks in RR- and RL-symmetry from Fig. 5.1.3, respectively. The range of the measured Raman shift Ω is from 300 cm^{-1} to 500 cm^{-1} in Fig. 5.1.4 (a) and from 230 cm^{-1} to 350 cm^{-1} in Fig. 5.1.4 (b). The measurements were performed with steps of $\Delta\Omega = 1$ cm^{-1} over the whole range. The RR- (shown in Fig. 5.1.4 (a)) and the RL-polarized (shown in Fig. 5.1.4 (b)) Raman spectra were measured at temperatures ranging between 4.2 K and 300 K.

The spectrum taken in RR-polarization shows one clear peak with an asymmetric shape, which hardens and sharpens continuously with decreasing temperature. The peak position shifts from 386.4 cm^{-1} at T $= 300$ K to 394.8 cm^{-1} at T $= 4.2$ K. The spectrum taken in RL-symmetry on the other hand shows one clear peak with a symmetric shape, which hardens and sharpens continuously with decreasing temperature as well. The peak position moves from 288.8 cm^{-1} at T $= 300$ K to 294.8 cm^{-1} at T $= 4.2$ K.

5.1.3. CsV_3Sb_5

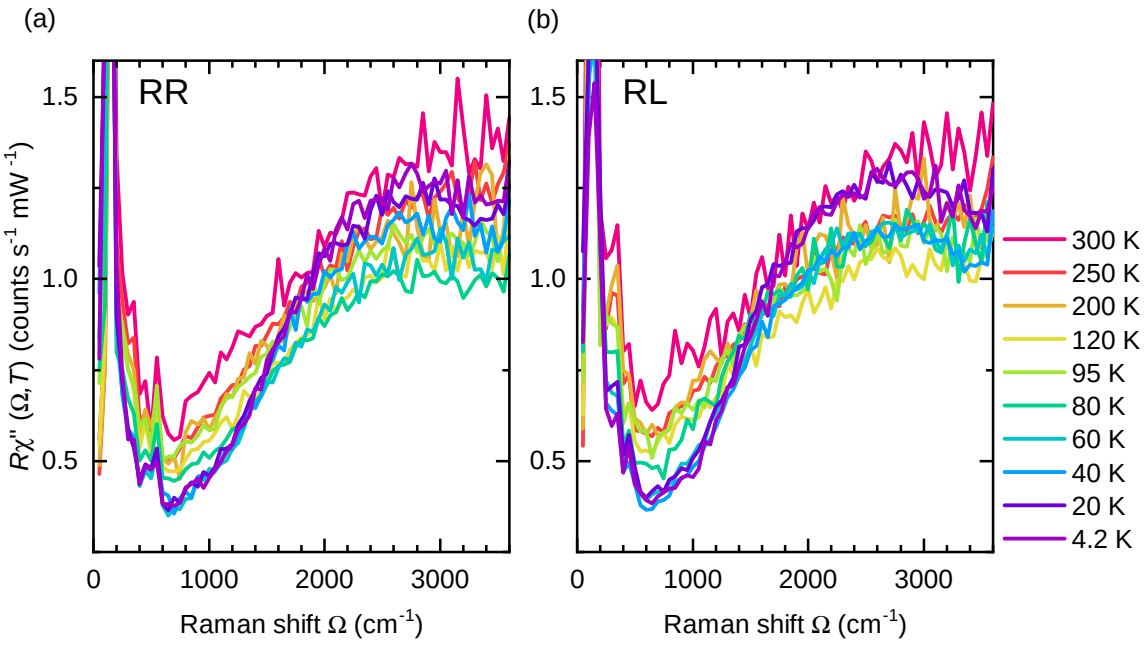

Figure 5.1.5.: Raman spectra from 50 cm^{-1} to 3600 cm^{-1} in (a) RR- and (b) RL-polarization for CsV_3Sb_5 at temperatures measured at the sample holder as indicated.

Long Ω-range spectra of CsV_3Sb_5 measured in the laboratory "Raman I" are shown in Fig. 5.1.5. Measurements in RR- and RL- polarization were taken with steps of $\Delta\Omega = 50$ cm^{-1} from 50 cm^{-1} to 3600 cm^{-1} at temperatures between $4.2 - 300$ K measured at the sample holder.

Fig. 5.1.5 (a) shows Raman spectra in RR-polarization above and below T_{CDW}, which consist of a strong peak at 138.2 cm^{-1} at 300 K on top of an electronic continuum. Upon cooling below T_{CDW}, spectral weight starts shifting from low to high energies with a crossing point at around 1500 cm^{-1}. The magnitude of this redistribution increases with lower temperatures, while no change is found above 95 K. Fig. 5.1.5 (b) shows Raman spectra in RL-polarization above and below T_{CDW}, which as well consist of a strong peak at 119.5 cm^{-1} at 300 K on a continuum. In RL-polarization, the same behaviour as in RR-polarization can be found, although the extent of the redistribution is slightly larger in the latter.

To take a closer look at the lower energy region, Raman spectra from 25 cm^{-1} to 300 cm^{-1} at temperatures between $4.2 - 300$ K were measured. Here, a step size of $\Delta\Omega = 1$ cm^{-1} between $\Omega \in [25, 150]$ cm^{-1} and $\Delta\Omega = 2.5$ cm^{-1} between $\Omega \in [150, 300]$ cm^{-1} was used. Both, RR- and RL-polarization are pictured in Fig. 5.1.6 (a) and (b), respectively. In RR-polarization three peaks appear additionally to the peak (3) at 138.2 cm^{-1} as already seen in Fig. 5.1.5 (a). The first peak (peak (1)) at the lowest energies appears below the CDW

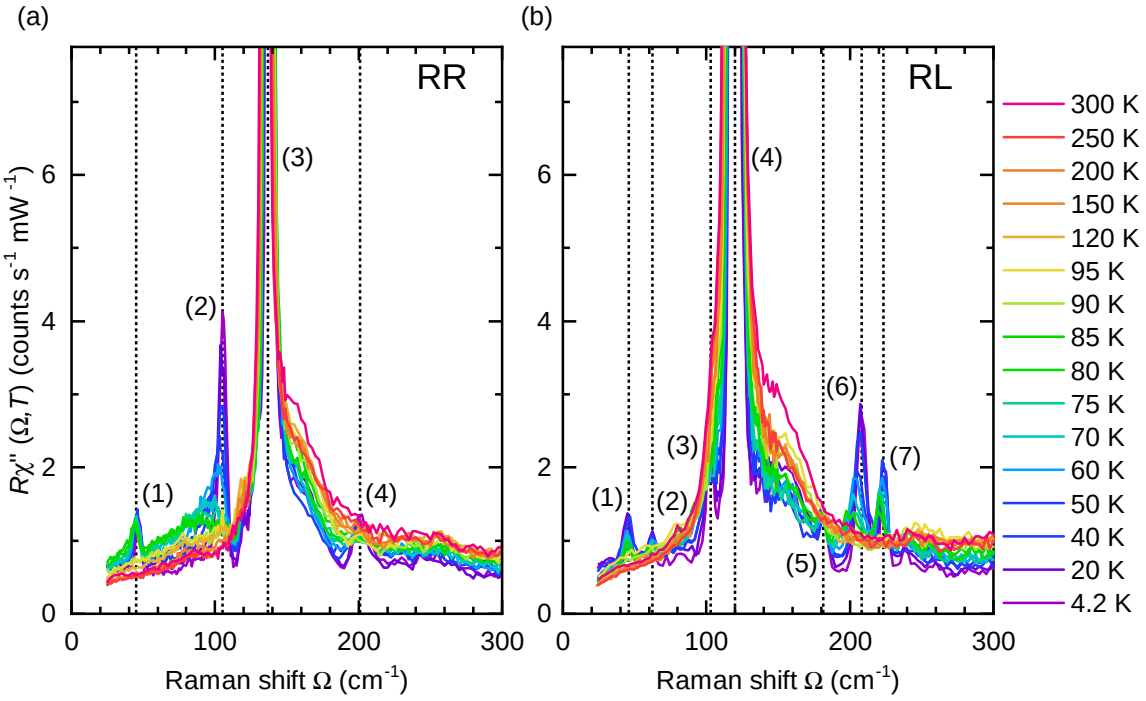

Figure 5.1.6.: Raman spectra from 50 cm^{-1} to 300 cm^{-1} in (a) RR- and (b) RL-polarization at temperatures measured at the sample holder as indicated in CsV_3Sb_5.

critical temperature $T_{CDW} = 94$ K at 42.1 cm^{-1}. It gains intensity, gets sharper and hardens for lower temperatures. Hence, the peak shifts from 42.1 cm^{-1} to 44.3 cm^{-1}. A second peak (peak (2)) builds up at low energies.First, a small hump appears around 85 K at 89.9 cm^{-1}. This hump shifts drastically to higher energies (from 89.9 cm^{-1} to 104.4 cm^{-1}), sharpens and gains intensity. Also, this peak shows an asymmetric form. The third peak at 134.6 cm^{-1} at 300 K shifts to higher energies (136.7 cm^{-1} at 4.2 K)and sharpens for lower temperatures. The fourth peak (peak (4)) slowly arises for temperatures below 70 K, sharpens and gains in intensity, but stays at its peak position of approximately 201 cm^{-1}.

In RL-polarization more peaks manifest additionally to the peak (peak (4)) located at 118.5 cm^{-1} at 300 K. Four peaks develop below 85 K. The first peak (peak (1)) is located at 44.0 cm^{-1}, the second one (peak (2)) at 60.2 cm^{-1}, the third one (peak (5)) at 179.3 cm^{-1} and the fourth one (peak (7)) at 220.0 cm^{-1}. All these four peaks sharpen, gain in intensity and shift to higher energies for lower temperatures (45.7 cm^{-1}, 62.4 cm^{-1}, 181.5 cm^{-1} and 223.9 cm^{-1} at 4.2 K, respectively). A fifth peak (peak (3)) begins to form below 60 K at 101 cm^{-1} overlaying on the slope of the fourth peak at 119.5 cm^{-1}. This peak behaves similar to the other already observed peaks. A sixth peak (peak (6)) arises from a small hump below 85 K at 199.8 cm^{-1}. This one behaves kind of similar to the second peak (peak (2)) in RR-polarization. The hump shifts drastically to higher energies (to 208.3 cm^{-1} at 4.2 K), sharpens and gains intensity, but it shows a symmetric form. In both, RR- and RL-polarization the peaks at 138.2 cm^{-1} and 119.5 cm^{-1} exhibit a shoulder on the higher

energy side, respectively.

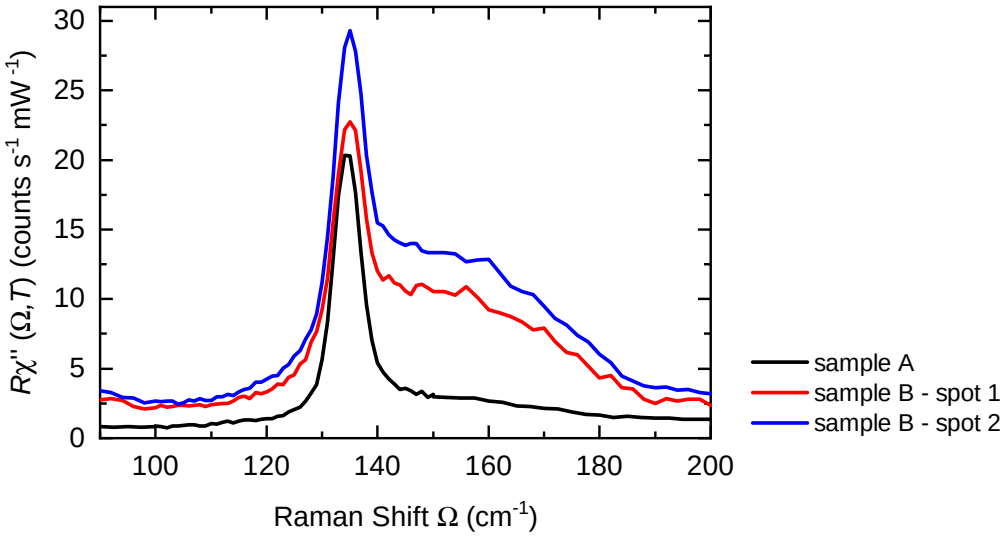

Figure 5.1.7.: Raman spectra in RR-polarization at 300 K for different samples of the material CsV_3Sb_5. In contrast to sample A, a clear shoulder manifests for sample B for both spots.

For the measurements on the material CsV_3Sb_5 different samples and the same sample reinstalled for a second time were investigated. Sample B designates the reinstalled sample A after some time at the air. A broad shoulder, which can be seen in Fig. 5.1.7, appears for sample B for different spots on the sample but is not observed for sample A. The same shoulder can be found in Fig. 5.1.6. Due to the fact, that in contrast to sample A, sample B was exposed to air for a long time, this shoulder probably originates from contamination of the sample surface.

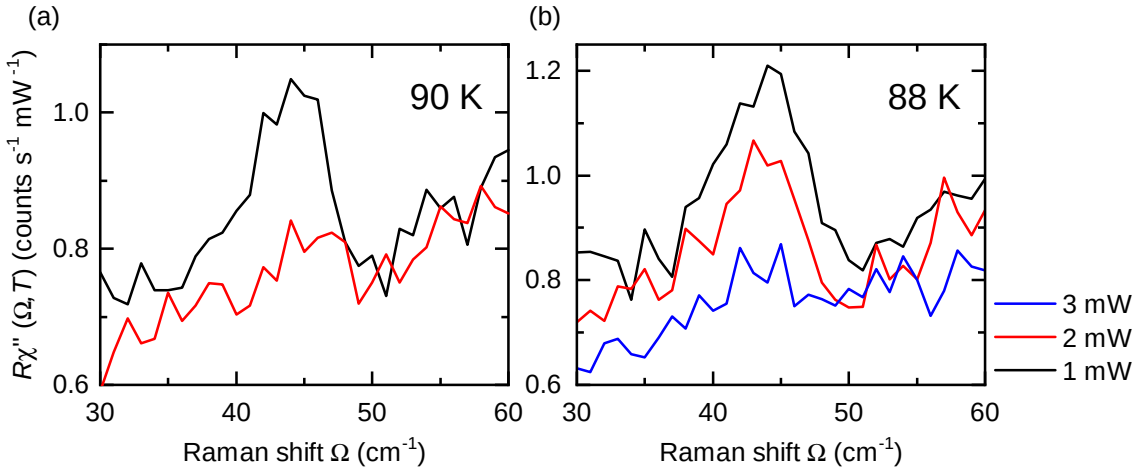

Figure 5.1.8.: Temperature calibration of the actual temperature on the sample CsV_3Sb_5 with the peak at 43.0 cm^{-1} in RR-polarization. (a) At 90 K the peak appears, if the laser beam has an absorbed laser power $p_{abs} = 1$ mW and disappears for $p_{abs} = 2$ mW. (b) At 90 K the peak appears up to an absorbed laser power $p_{abs} = 2$ mW. For $p_{abs} = 3$ mW the peak disappears.

The peak with the energy $\Omega = 43.0$ cm^{-1} appears abruptly in RR-polarization, when cooling down below the CDW critical temperature $T_{CDW} = 94$ K [22]. Therefore, this sharp peak can be used to determine the additional heating of the sample due to the laser spot on the sample. Measurements were made at two different temperatures, 90 K and 88 K using a different laser beam power. These measurements are pictured in Fig. 5.1.8 (a) and (b), respectively. At 90 K, the peak appears, if 1 mW absorbed laser power is applied and disappears for $p_{abs} = 2$ mW. At 88 K the peak is visible for $p_{abs} = 1$ mW and $p_{abs} = 2$ mW but vanishes for $p_{abs} = 3$ mW. Since the peak only appears for temperatures below $T_{CDW} = 94$ K a value for the laser-induced heating can be found: $2\text{ K} < h < 3\text{ K}$. Looking at the measurement at 85 K with a laser power of $p_{abs} = 4$ mW, the peak is also present. Therefore the heating range is $2\text{ K} < h < 2.25\text{ K}$. Although the impact of heating is higher at lower temperatures, a constant value for the heating will be taken into account. Therefore, the average of the two boundary values is used and added to the temperature values measured at the sample holder: $h \approx 2.1$ K. From now on temperatures of measurements of CsV_3Sb_5 will be adjusted.

5.2. Tetraboride TmB_4

All measurements of TmB_4 were performed in the laboratory "Raman II". Long Ω-range spectra of TmB_4 are shown in Fig. 5.2.1. Measurements in RR- and RL- polarization were taken with steps of $\Delta\Omega = 1.25$ cm^{-1} from 30 cm^{-1} to 1142.5 cm^{-1} at temperatures between $1.8 - 12$ K at the sample holder as indicated. A static external magnetic field $B = 1$ T was applied during the measurements. The data are consecutively offset by 0.65 cts/(s mW) in RR- and by 0.8 cts/(s mW) in RL-polarization for clarity.

Fig. 5.2.1 (a) present Raman spectra in RR-polarization at temperatures as indicated, which consist of various peaks on an electronic continuum. Four peaks are observed in this polarization. The first peak appears at around 98.5 cm^{-1}, the second peak at 531.6 cm^{-1}, the third peak at 804.45 cm^{-1} and the fourth one at 1000.5 cm^{-1} in all temperatures. Fig. 5.2.1 (b) depicts Raman spectra in RL-polarization at temperatures as indicated, which consist of six peaks on an electronic continuum. The following peak energies were recorded at 1.8 K. The first peak appears at 119.5 cm^{-1} and the second peak at 601.2 cm^{-1}. The following double peak consists of the third and fourth peak of the spectra, which are located at 660.6 cm^{-1} and 681.0 cm^{-1}, respectively. The fifth peak with energy 982.1 cm^{-1} overlaps with the shoulder of the sixth peak, which has a Raman shift of 1001.2 cm^{-1}. No visible change in linewidth or position occurs for higher temperatures.

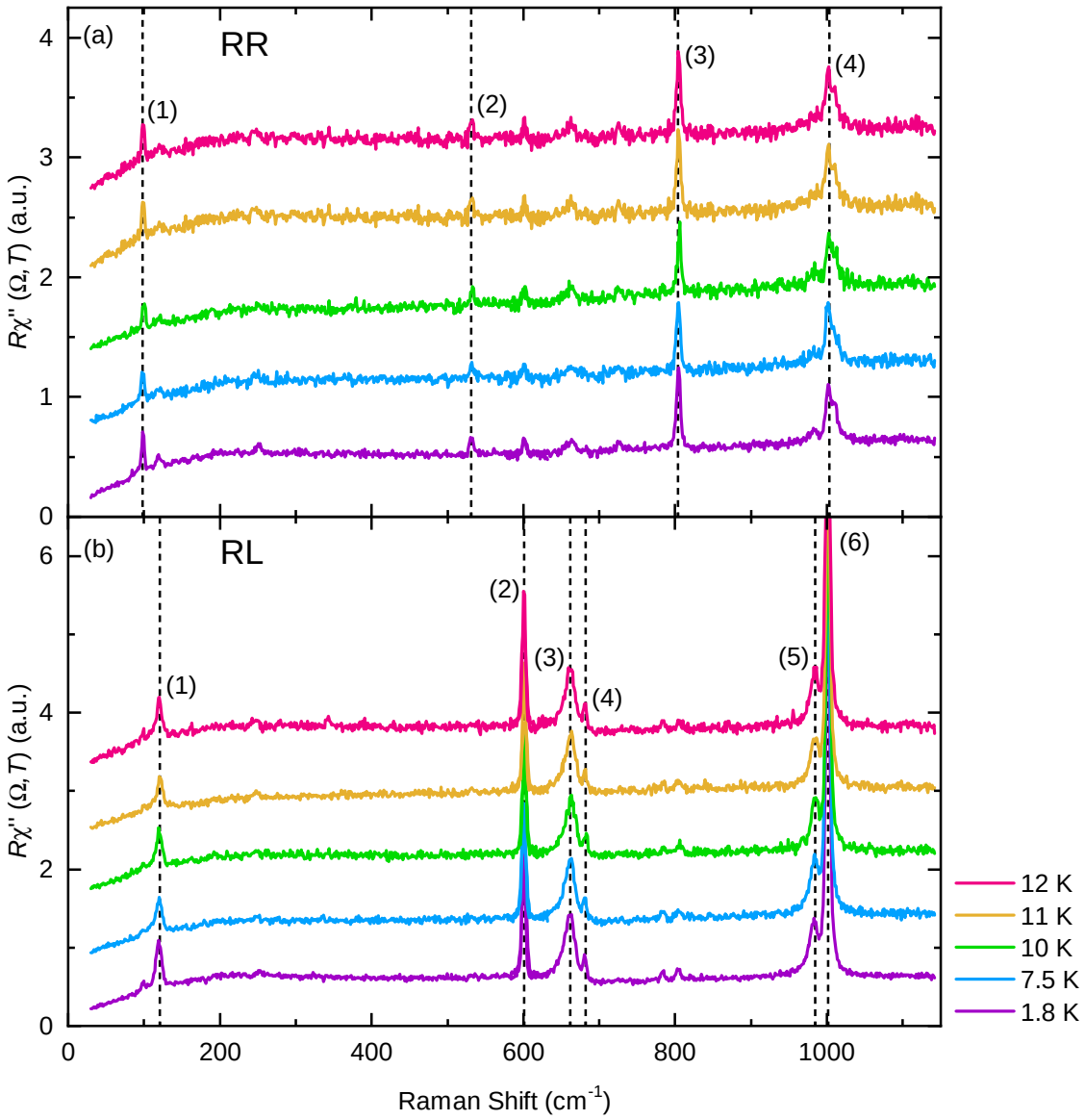

Figure 5.2.1.: The temperature-dependent Raman spectra of TmB_4 in the (a) RR- and (b) RL-polarization at temperatures as indicated in the "Raman lab II", respectively. A magnetic field B = 1 T was applied. The data are consecutively offset by 0.65 cts/(s mW) in RR- and by 0.8 cts/(s mW) in RL-polarization for clarity. The dashed black lines mark the energy of the peak at the highest temperature.

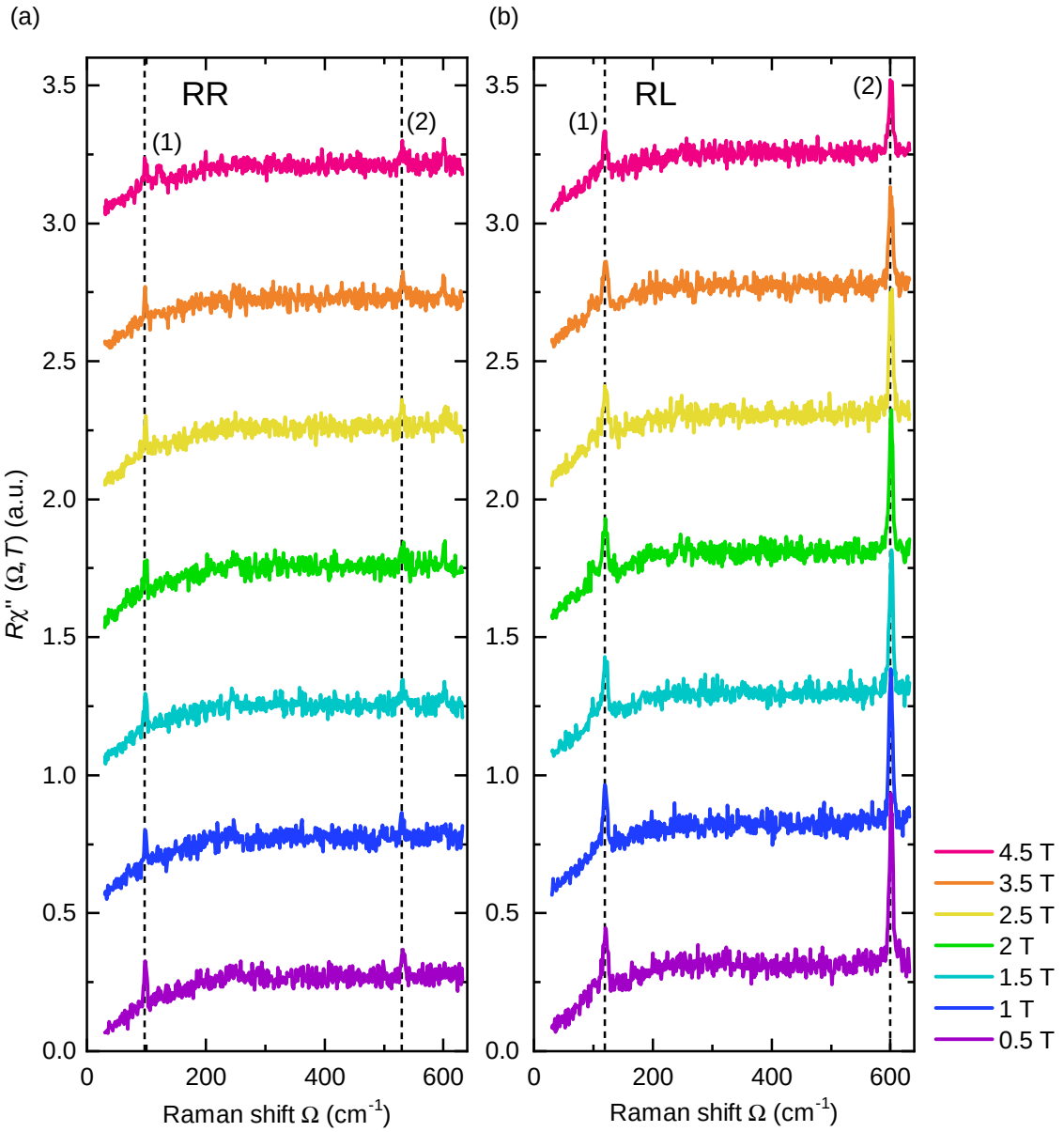

Figure 5.2.2.: The temperature-dependent Raman spectra at T = 20 K of TmB_4 in the (a) RR- and (b) RL-polarization measured with applied magnetic fields as indicated in the "Raman lab II", respectively. The data are consecutively offset by 0.5 cts/(s mW) each for clarity. The dashed black lines mark the energy of the peak at the highest magnetic field.

Low energy Raman spectra of TmB_4 obtained at T = 20 K are pictured in Fig. 5.2.2. Measurements with a step size of $\Delta\Omega = 1.25$ cm^{-1} from 30 cm^{-1} to 632.5 cm^{-1} were performed in RR- and RL-polarization while a static external magnetic field was applied ranging between B = 0.5 − 4.5 T. The magnetic field was ramped up in steps of $\Delta B = 0.5$ T. The data are consecutively offset by 0.5 cts/(s mW) each for clarity. Raman spectra obtained in RR-polarization, which are illustrated in Fig. 5.2.2 (a) are composed of two peaks superimposed on a continuum. The first peak appears at 98.3 cm^{-1} and the second peak at 532.2 cm^{-1}. In RL-polarization on the other hand two peaks appear as well. The

corresponding Raman spectra are shown in Fig. 5.2.2 (b). These two peaks at 120.35 cm^{-1} and 601.2 cm^{-1}, respectively, are also overlaying on an electronic continuum.

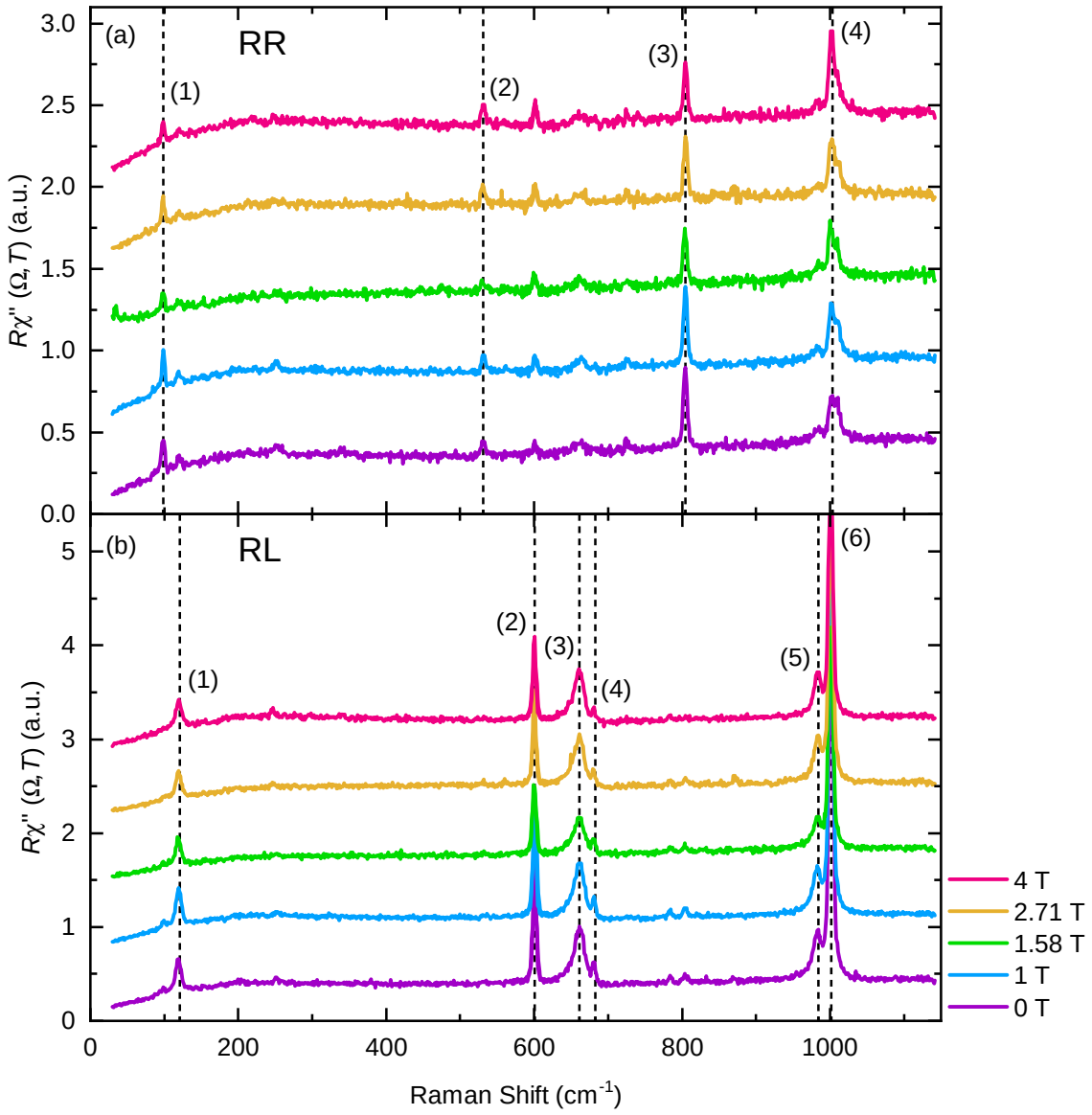

Figure 5.2.3.: The temperature-dependent Raman spectra in the superfluid phase at T = 1.8 K of TmB_4 in the (a) RR- and (b) RL-polarization measured with applied magnetic fields as indicated in the "Raman lab II", respectively. The data are consecutively offset by 0.5 cts/(s mW) in RR- and 0.7 cts/(s mW) in RL-polarization for clarity. The dashed black lines mark the energy of the peak at the highest magnetic field.

Fig. 5.2.3 illustrates Raman spectra taken in the superfluid phase at T = 1.8 K in both RR- and RL-polarization. These measurements were carried out in steps of $\Delta\Omega = 1.25$ cm^{-1} in an energy range of 30 cm^{-1} to 1142.5 cm^{-1}. A static external magnetic field as indicated was applied during the measurements. The data are consecutively offset by 0.5 cts/(s mW) in RR- and 0.7 cts/(s mW) in RL-polarization for clarity.

The RR-polarized Raman response in Fig. 5.2.3 (a) consists of four sharp peaks superimposed on a continuum. At zero-field the first peak is located at 98.1 cm^{-1}, the second peak at 531.1 cm^{-1}, the third peak at 804.1 cm^{-1} and the fourth peak at 1005.4 cm^{-1}. In RL-polarization in addition to the first peak with the energy 119.0 cm^{-1} and the second peak with the energy 600.6 cm^{-1}, two double peaks can be identified. The first double peak consists of the energy-wise third and the fourth peak, which occur at 660.9 cm^{-1} and 680.8 cm^{-1}, respectively. The fourth peak overlaps with the shoulder of the third peak. The second double peak arises from the fifth and the sixth peak of the RL-polarized Raman response. These members of the second double peak have the energies 982.4 cm^{-1} and 1001.4 cm^{-1}, respectively.

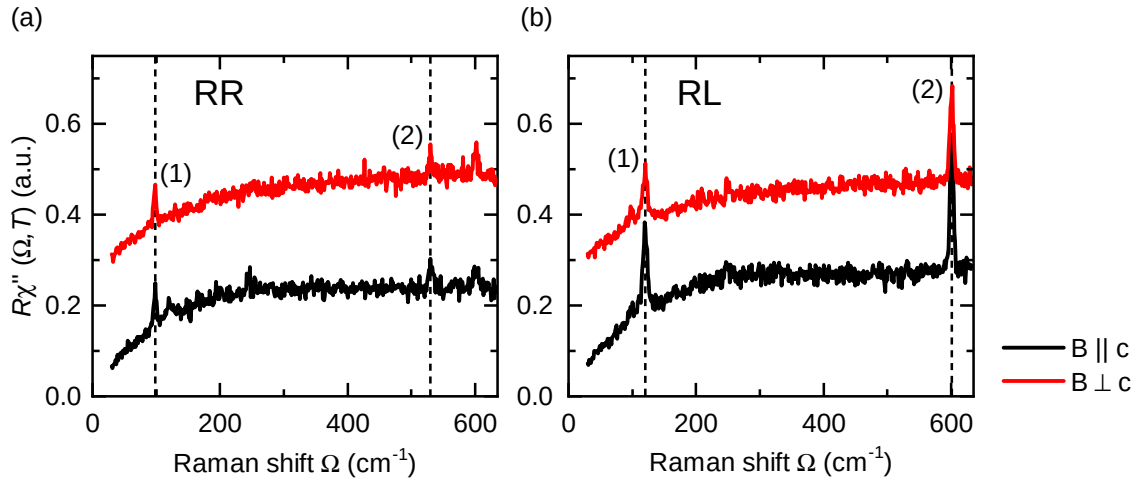

Figure 5.2.4.: The temperature-dependent Raman spectra with an applied magnetic field B $=$ 5 T at T $=$ 20 K of TmB_4 in the (a) RR- and (b) RL-polarization measured in the "Raman lab II", respectively. The data are consecutively offset by 0.25 cts/(s mW) each for clarity. The dashed black lines mark the energy of the peak. The sample was cooled down to T $=$ 20 K. First, the measurement with B $\parallel$ c was performed. Afterwards, the sample was rotated so B $\perp$ c.

The measurements of TmB_4 in Fig. 5.2.4 were performed at a static externally applied magnetic field at T $=$ 20 K in both RR- and RL- polarization. First, the sample was cooled down to the desired temperature and afterwards the magnetic field, which was applied parallel to the c-direction of the sample, was ramped up to B $=$ 5 T. After the measurement with B $\parallel$ c were taken, the sample was rotated to B $\perp$ c and the same measurement was repeated. These measurements were performed with a step size of $\Delta\Omega = 1.25$ cm^{-1} from 30 cm^{-1} to 632.55 cm^{-1}. The data are consecutively offset by 0.25 cts/(s mW) each for clarity.

The two peaks onto a continuum in RR-polarization are located at 98.2 cm^{-1} and 530.8 cm^{-1}, respectively, while the RL-polarization data consist of two peaks onto a continuum as well, which have the energies 119.8 cm^{-1} and 600.7 cm^{-1}. The energies of the peaks correspond to $B \parallel$ c. The peaks change neither in shape nor in position, if the sample is rotated in an applied external magnetic field.

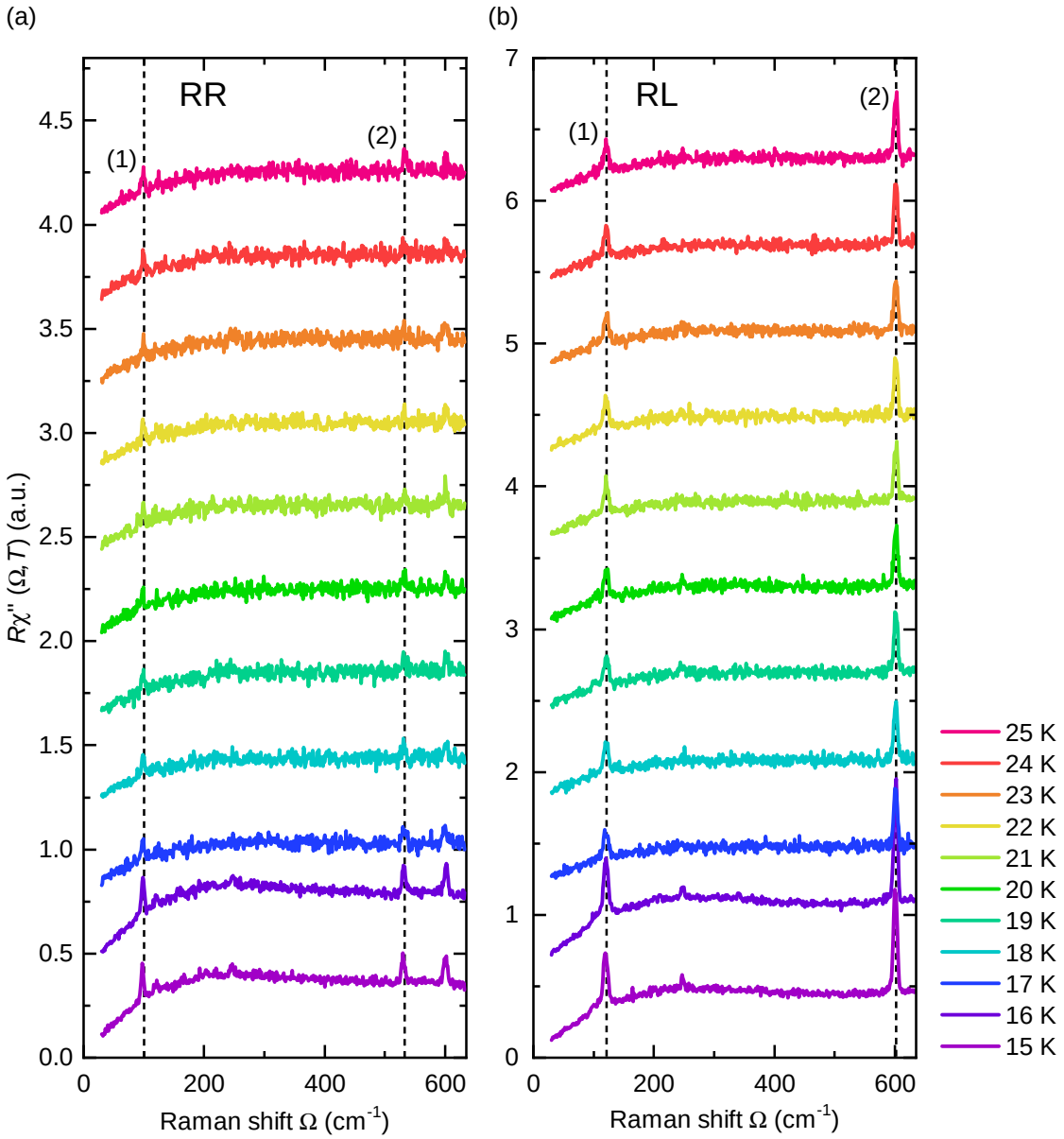

Figure 5.2.5.: The temperature-dependent Raman spectra with an applied magnetic field B = 4.5 T of TmB_4 in the (a) RR- and (b) RL-polarization measured at temperatures as indicated in the "Raman lab II", respectively. The data are consecutively offset by 0.4 cts/(s mW) in RR- and 0.6 cts/(s mW) in RL-polarization for clarity. The dashed black lines mark the energy of the peak.

Raman spectra were recorded at temperatures between 15 K and 25 K with $\Delta T = 1$ K. The corresponding Raman response is illustrated in Fig. 5.2.5 (a) in RR- and (b) in RL-polarization. The step size was $\Delta\Omega = 1.25$ cm^{-1} in a range $[30, 1142.5]$ cm^{-1}. The two peaks in RR-polarization have the energies 97.8 cm^{-1} and 530.2 cm^{-1} at 15 K. The two sharp peaks in RL-polarization are located at 119.5 cm^{-1} and 600.5 cm^{-1}, respectively. The shape of the continuum and the lost intensity between of the spectra below 16 K and above 17 K has changed due to the new alignment of the optics.

6. Discussion

6.1. Kagome

6.1.1. Fe_3Sn_2

As already introduced in Section 2.1.1 the space group of Fe_3Sn_2 is $R\bar{3}m$ (No. 166) and is part of the D_{3d} point group. This leads to the corresponding Raman tensors

$$A_{1g} = \begin{pmatrix} a & 0 & 0 \\ 0 & a & 0 \\ 0 & 0 & b \end{pmatrix},$$
$$E_g^{(1)} = \begin{pmatrix} c & 0 & 0 \\ 0 & -c & d \\ 0 & d & 0 \end{pmatrix}, \text{ and} \tag{6.1}$$
$$E_g^{(2)} = \begin{pmatrix} 0 & -c & -d \\ -c & 0 & 0 \\ -d & 0 & 0 \end{pmatrix}.$$

The Wyckoff positions of the Fe (18h) and the Sn (6c1, 6c2) atoms indicate the existence of four A_{1g} and five E_g Raman-active phonons. According to the Raman tensors shown in Eq. 6.1 the A_{1g} phonons may be projected in the RR- and the E_g phonons in the RL-channel. With this information the peaks in Fig. 5.1.1 (a) can be identified as the four A_{1g} Raman-active phonons. In Fig. 5.1.1 (b) only four out of the five expected E_g Raman-active phonons can be identified. The fifth absent E_g phonon is probably to weak in intensity to be detected with this experimental setup. The respective eigenvectors of the identified A_{1g} and E_g phonon modes are pictured in Fig. 6.1.1.

To quantitatively analyze the observed phonons in the A_{1g} and E_g channels, these were fitted using a Voigt function (see Section 4.2.3). The widths indicated correspond directly to those of the phonon modes. The investigated peak energies and the linewidths (FWHM) are shown in Fig. 6.1.2 and 6.1.3. They were labeled consecutively from low to high energies. All phonon modes behave similar as a function of temperature, as already described in Section 5.1.1: they become harder and narrower upon cooling, which is a usual change in width and energy of phonons and is related to the anharmonic decay [98] and the lat-

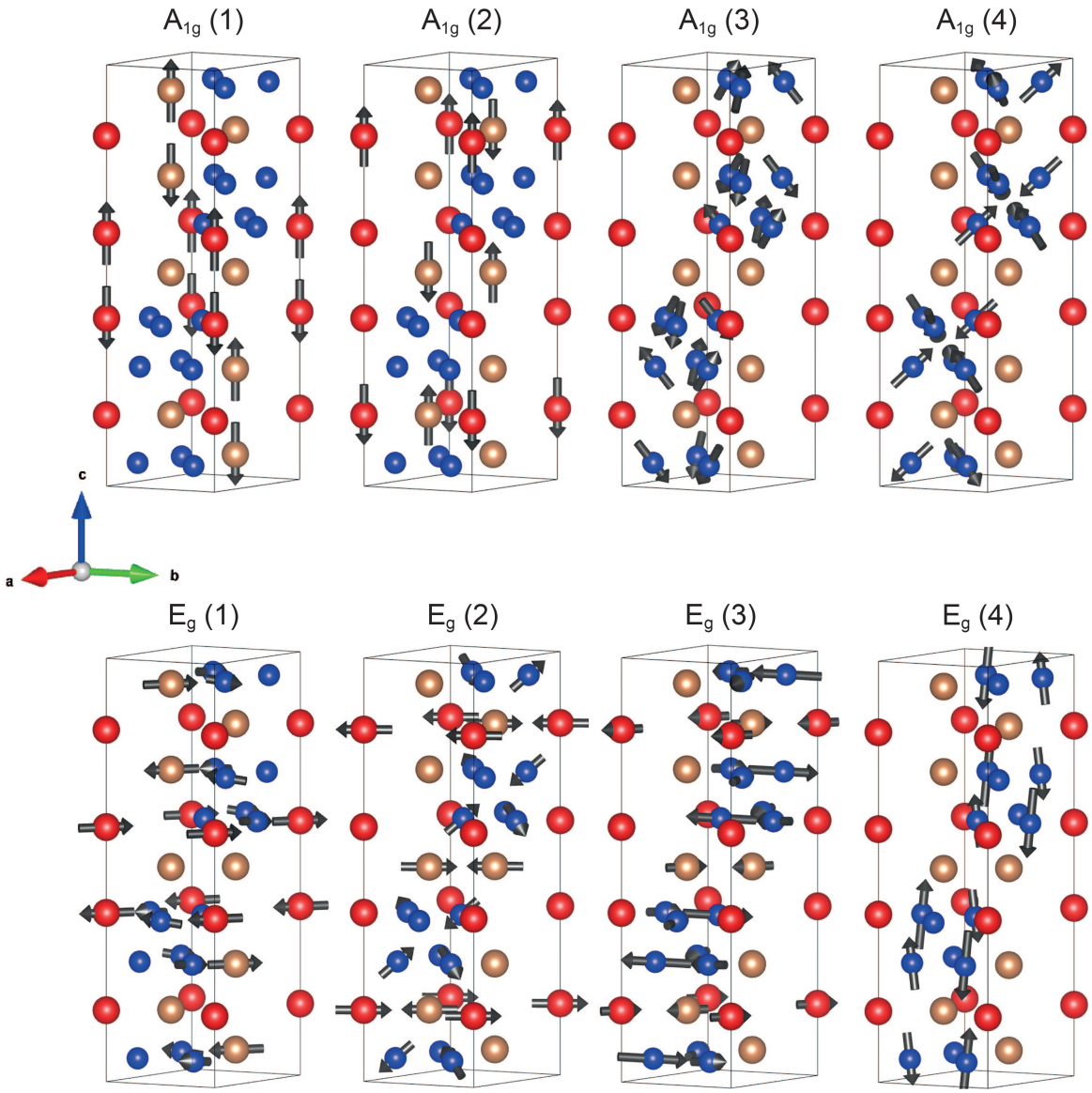

Figure 6.1.1.: Eigenvectors of the A_{1g} and E_g phonon modes. The blue atoms describe the position of the Fe atoms, which order in a perfectly aligned kagome lattice. The red and gold atoms represent the Sn atoms either located on the corners of the unit cell or forming a honeycomb lattice below and above each kagome lattice. The black arrows indicate the possible phononic vibration modes of the individual atoms in the lattice [17].

tice contraction [99]. As it can be seen in Fig. 6.1.2 the A_{1g} modes (full black symbols), which were measured upon cooling as indicated in the figure, deviate from the expected behaviour in the temperature range around 100 K (hatched area). There, kinks are observed in the energies of the $A_{1g}(1)$, $A_{1g}(3)$ and $A_{1g}(4)$ modes. Upon remeasuring the data in a row warming up from 50 K with an increment of 10 K in the temperature range from $50 - 150$ K and an increment of 50 K in the temperature range from $150 - 300$ K (open black symbols) demonstrates that the kinks can still be observed, although they are shifted slightly in energy. The origin of this shift is not entirely clear. It may be related to the first-order nature of the reorientation transition and a possible hysteresis [62]. An influence of

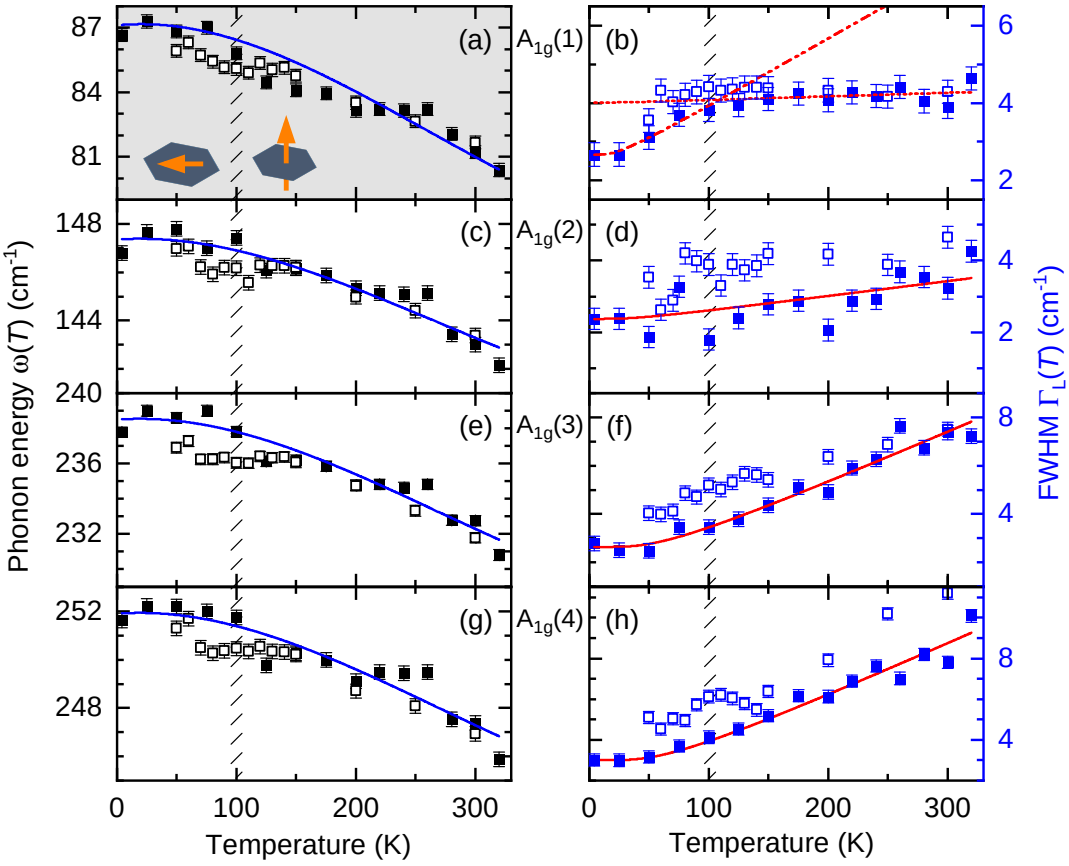

Figure 6.1.2.: Phonon energies ω_0 (black) and Lorentzian widths Γ_L (blue) of Fe_3Sn_2 in A_{1g} symmetry. The magnetization orientation with respect to the ab plane is indicated in (a). The parameters are derived by fitting procedures as described in the text. The first series of measurements (full black and blue symbols) were taken at temperatures listed in the following sequence: $[320, 300, 200, 100, 75, 50, 25, 4.2, 125, 150, 175, 220, 240, 260, 280]$ K. The second series (open black and blue symbols) was measured in a row warming up from 50 K with an increment of 10 K in the range of interest from $50 - 150$ K. All linewidths Γ_L were fitted according to Eq. 6.2 (red lines). The linewidth of the A_{1g} mode at 86 cm^{-1} in panel (b) shows an anomalous behavior, displaying a change in the expected temperature dependence at ≈ 100 K as indicated by the dashed area. Eq. 6.2 yields $\lambda_{\text{ph-ph},1} = 0.2$ at low temperature and only $\lambda_{\text{ph-ph},1} = 0.015$ above 100 K [17].

the fitting procedure is unlikely but cannot be excluded with certainty.

As already mentioned the phonon width reduces with decreasing temperature. This conventional reduction can be understood in terms of anharmonic decay [98] and can be represented by

$$\Gamma_L(T) = \Gamma_{L,0}\left(1 + \frac{2\lambda_{\text{ph-ph}}}{\exp\left(\frac{\hbar\omega_0}{2k_BT}\right) - 1}\right). \tag{6.2}$$

Since $\Gamma_{\mathrm{L},0}(T)$ and ω_0 can be extrapolated to zero from the experimental points below 50 K, only the phonon-phonon coupling $\lambda_{\text{ph-ph},i}$ in Eq. 6.2 is left as a free parameter, which is determined by a least-square fit of Eq. 6.2 to the experimental data. The fitted curves are

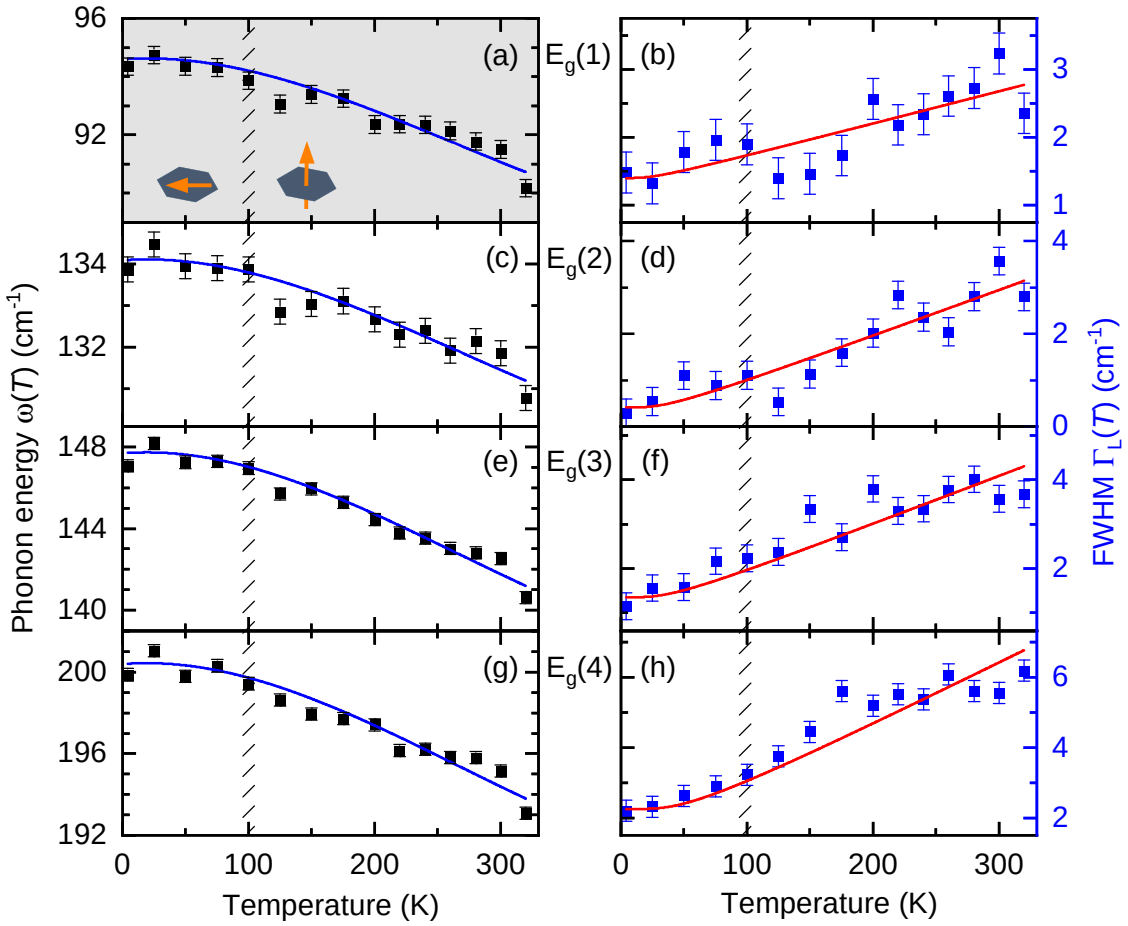

Figure 6.1.3.: Phonon energies ω_0 (black) and Lorentzian widths Γ_L (blue) of Fe_3Sn_2 in E_g symmetry. The linewidth and phonon energies behave like those of ordinary phononic excitations without anomaly near the spin reorientation transition temperature [17].

shown as dashed-dotted and dotted red lines in Fig. 6.1.2. The resulting values for $\lambda_{\text{ph-ph}}$ can be found in Table 6.1.1.

All phonons except for the $A_{1g}(1)$ mode show conventional behaviour and become exponentially narrower upon cooling. The only exception, the $A_{1g}(1)$ phonon, behaves unexpectedly. The impact of the Kagome layer on the phonon energy changes is only visible in the A_{1g} channel due to the eigenvectors. Hence, it can not be seen in E_g. The temperature-dependence according to Eq. 6.2 only appears for $T \leq 100$ K as shown as a dashed-dotted line in Fig. 6.1.2 (a). The phonon-phonon coupling yields $\lambda_{\text{ph-ph}}(A_{1g}(1)) = 0.2$. For a temperature $T \geq 100$ K the width is nearly temperature independent which corresponds to an unusually small coupling of $\lambda_{\text{ph-ph}}(A_{1g}(1)) = 0.015$. The symmetric phonon-phonon decay channel is only accessible, if the spins are rotated into the ab-plane. Otherwise (spins pointing along the c-axis) the channel is blocked.

Since the phonon energy $\omega(T)$ contains contributions from the lattice contraction, which depends on the thermal occupation of the phonons, as well as from the anharmonic decay it can be described by

Phonon	$A_{1g}(1)$	$A_{1g}(2)$	$A_{1g}(3)$	$A_{1g}(4)$
$\lambda_{\text{ph-ph},i}$	0.20 ± 0.02, 0.015 ± 0.008	0.14 ± 0.05	0.68 ± 0.08	0.74 ± 0.08
γ_i	0.84 ± 0.05, 0.88 ± 0.05	0.34 ± 0.02	0.32 ± 0.02	0.22 ± 0.01
Phonon	$E_g(1)$	$E_g(2)$	$E_g(3)$	$E_g(4)$
$\lambda_{\text{ph-ph},i}$	0.11 ± 0.03	1.11 ± 0.59	0.29 ± 0.06	0.42 ± 0.07
γ_i	0.46 ± 0.02	0.25 ± 0.01	0.51 ± 0.02	0.37 ± 0.02

Table 6.1.1.: Electron-phonon coupling and mode-specific Grüneisen parameters. The phonon-phonon coupling parameters $\lambda_{\text{ph-ph},i}$ were derived from the approximate harmonic fits to the temperature-dependent linewidths according to Eq. 6.2. As indicated in Fig. 6.1.2 as dashed-dotted and dotted lines, respectively, the two values of $\lambda_{\text{ph-ph},i}$ for $A_{1g}(1)$ correspond to temperatures above and below 100 K [17]. The Grüneisen parameters are derived according to Eq. 6.3.

$$\begin{aligned}\omega_{\text{ph},i}(T) &= \omega_i(0) + \Delta_i(T) = \omega_i(0) + \Delta_i^{(1)}(T) + \Delta_i^{(2)}(T) \\ &= \omega_i(0) + \omega_i(0)\left\{\exp\left[-3\gamma_i \int_0^T \alpha(T')dT'\right] - 1\right\} - \frac{\Gamma_i(0)^2}{2\omega_i(0)}\left[1 + \frac{4\lambda_{\text{ph-ph},i}}{\exp\left(\frac{\hbar\omega_0}{2k_BT}\right) - 1}\right].\end{aligned} \tag{6.3}$$

Here, only the two lowest-order contributions $\Delta_i(T) = \Delta_i^{(1)}(T) + \Delta_i^{(2)}(T)$ are taken into account. The first order contribution $\Delta_i^{(1)}(T)$ originates from the thermal lattice expansion, while the second order contribution $\Delta_i^{(2)}(T)$ stems from the anharmonic decay of phonons. The phonon energy $\omega_{\text{ph},i}(T)$ can be described by Eq. 6.3 [100]. The thermal expansion data $\alpha(T)$ was obtained from unpublished data [101] (c.f. Appendix A.1). The theoretical temperature dependences according to Eq. 6.3 are displayed in Fig. 6.1.2 (a), (c), (e) and (g) as well as Fig. 6.1.3 (a), (c), (e) and (g) by blue curves. The relative change in frequency of the lattice vibrations is proportional to the relative volume change [102]. This fact is expressed by the Grüneisen parameter $\gamma_{\mathbf{k}s} = -\partial(\ln \omega_i)/\partial(\ln V)$ of the mode $\mathbf{k}s$. In a real solid, $\gamma_{\mathbf{k}s}$ is not the same for all normal modes. Hence, the overall Grüneisen parameter γ

$$\gamma = \frac{\sum_{\mathbf{k},s} \gamma_{\mathbf{k}s} c_{vs}(\mathbf{k})}{\sum_{\mathbf{k},s} c_{vs}(\mathbf{k})}, \tag{6.4}$$

defined as the weighted average of $\gamma_{\mathbf{k}s}$, is temperature-dependent. As stated by Ashcroft and Mermin. [103], $\gamma_{\mathbf{k}s}$ of each normal mode is weighted by its contribution to the specific heat c_{vs}. According to Eq. 6.4, γ approaches a constant value at temperatures close to and above the Debye temperature (c.f. Ref. [100]), as well as a (different) constant value for $T \to 0$ [103]. All Grüneisen parameters γ_i in this thesis describe the overall Grüneisen parameter γ in the large temperature limit.

The mode specific Grüneisen parameters γ_i of Fe_3Sn_2 can be found in Tab. 6.1.1. All

phonon modes have $\gamma < 1$. Except for the $A_{1g}(1)$ phonon mode, all γ_i are around 0.5. The Grüneisen parameter for the $A_{1g}(1)$ phonon mode is $\gamma_{A_{1g}(1),1} = 0.84$ for $\lambda_{\text{ph-ph},1}(A_{1g}(1)) = 0.2$ and $\gamma_{A_{1g}(1),2} = 0.88$ for $\lambda_{\text{ph-ph},2}(A_{1g}(1)) = 0.015$. Since the Grüneisen parameters of the $A_{1g}(1)$ phonon mode of the two different phases do not differ in the same magnitude as the phonon-phonon coupling parameter $\lambda_{\text{ph-ph}}(A_{1g}(1))$, the first order contribution $\Delta_i^{(1)}(T)$ presumably dominates the phonon energy ω.

Fe_3Sn_2 is purely magnetic. It orders at $T_C \approx 670$ K. Therefore, gaps are not expected in the temperature range below 300 K. As shown in Fig. 5.1.2 the E_g spectra vary only little with temperature below 100 cm^{-1}. But the increase at low temperature is considered to be real. A peak at ≈ 47 cm^{-1} appears at 4.2 K, which doesn't diverge towards zero energy as it would in the case of diffuse scattering of laser light. There could be three origins of this intensity increase: It could either originate from particle-hole excitations which reflects the temperature dependence of the resistivity $\rho(T)$ [see Fig. 5.1.1 (b)], from a band gap induced by the spin reorientation which were suggested by the optical measurements [104] or from magnetic fluctuations in a geometrically frustrated system similar to FeSe [89]. There are no indications of a flat band in the 200 meV range which would be expected to manifest itself as an enhanced intensity in the range 200 meV or 1600 cm^{-1}.

As opposed to the E_g spectra [Fig. 5.1.2 (a)], the A_{1g} continuum is essentially temperature-independent [Fig. 5.1.2 (b)]. As already mentioned, different excitations or regions of the Brillouin zone are projected in the two different symmetries. With the knowledge of the correspondence between transport and low-energy E_g spectra, our observation suggests that the carrier relaxation observed in the A_{1g} spectra is almost temperature-independent [17].

6.1.2. $Co_3Sn_2S_2$

Just as Fe_3Sn_2, the Weyl semimetal $Co_3Sn_2S_2$ belongs to the space group $R\bar{3}m$ and the point group D_{3d}. According to the Wyckoff-positions of the Co (9d), the S (6c) and the S (3a, 3b) atoms, one A_{1g} and one E_g phonon mode are Raman-active. The A_{1g} and the E_g phonon modes are the allowed representations of the Wyckoff position of the S atoms (6c) and can be projected in the RR- and RL-channel, respectively.

Fig. 6.1.4 shows the phononic excitations in the A_{1g} and E_g channels as solid lines at the temperatures indicated along with the theoretical curves as black dashed lines. The spectra are consecutively offset by 1 cts/(s mW) for clarity. A smooth phenomenological curve as a background is subtracted before fitting. Since the phonon line of E_g [Fig. 6.1.4 (b)] is symmetric, a Voigt function was used to fit the data. The A_{1g} [Fig. 6.1.4 (a)] phonon line, on the other hand, shows an obvious asymmetric shape. This asymmetry stems from the interference between the electronic continuum and the phonon [106]. Therefore, a Fano function convoluted with a Gauss function is used for fitting the A_{1g} phonon line [105]:

$$\chi''(\omega) = \left|\frac{A}{q^2-1}\right| \frac{2\sqrt{\ln(2)}}{\omega_G\sqrt{\pi}} \Big\{ \left(q^2-1\right)\cdot B(\omega) - 2q\cdot C(\omega) \Big\}$$

$$B(\omega) = \frac{1}{\pi}\int_{-\infty}^{\infty} \frac{\sqrt{\ln(2)}\cdot\frac{\omega_L}{\omega_G}\cdot e^{-t^2}}{\left(\sqrt{\ln(2)}\cdot\frac{\omega_L}{\omega_G}\right)^2 + \left(2\sqrt{\ln(2)}\cdot\frac{\omega-\omega_c}{\omega_G} - t\right)^2}\, dt \tag{6.5}$$

$$C(\omega) = \frac{-1}{\pi}\int_{-\infty}^{\infty} \frac{\left(2\sqrt{\ln(2)}\cdot\frac{\omega-\omega_c}{\omega_G} - t\right)\cdot e^{-t^2}}{\left(\sqrt{\ln(2)}\cdot\frac{\omega_L}{\omega_G}\right)^2 + \left(2\sqrt{\ln(2)}\cdot\frac{\omega-\omega_c}{\omega_G} - t\right)^2}\, dt$$

The resulting temperature-dependent fitting parameters of the A_{1g} and E_g phonon lines are depicted in Fig. 6.1.5. The hatched area indicates the phase transition temperature $T_C = 180$ K. The ferromagnetic (FM) and the paramagnetic (PM) phases are indicated. The dashed black lines represent the prediction according to Eq. 6.3. The volume change of $Co_3Sn_2S_2$, which is needed to calculate the phonon energy [107], can be found in Appendix A.2. The dashed blue and purple lines on the other hand represent the change in linewidths of both the Fano and the Voigt function. The temperature dependence is given by Eq. 6.2 and obtained by a least square fit to the experimental data.

Fig. 6.1.5 (a) pictures the A_{1g} phonon mode parameters. The dashed black line and therefore Eq. 6.3 nicely describes the phonon energy dispersion as a function of temperature. In the phonon linewidth an anomalous behaviour can be found. The whole temperature range cannot be described by a single set of parameters. Therefore, the range below and above the phase transition temperature $T_C = 180$ K was considered separately. The dashed blue line represents the data below T_C and the dashed purple line above T_C. At the transi-

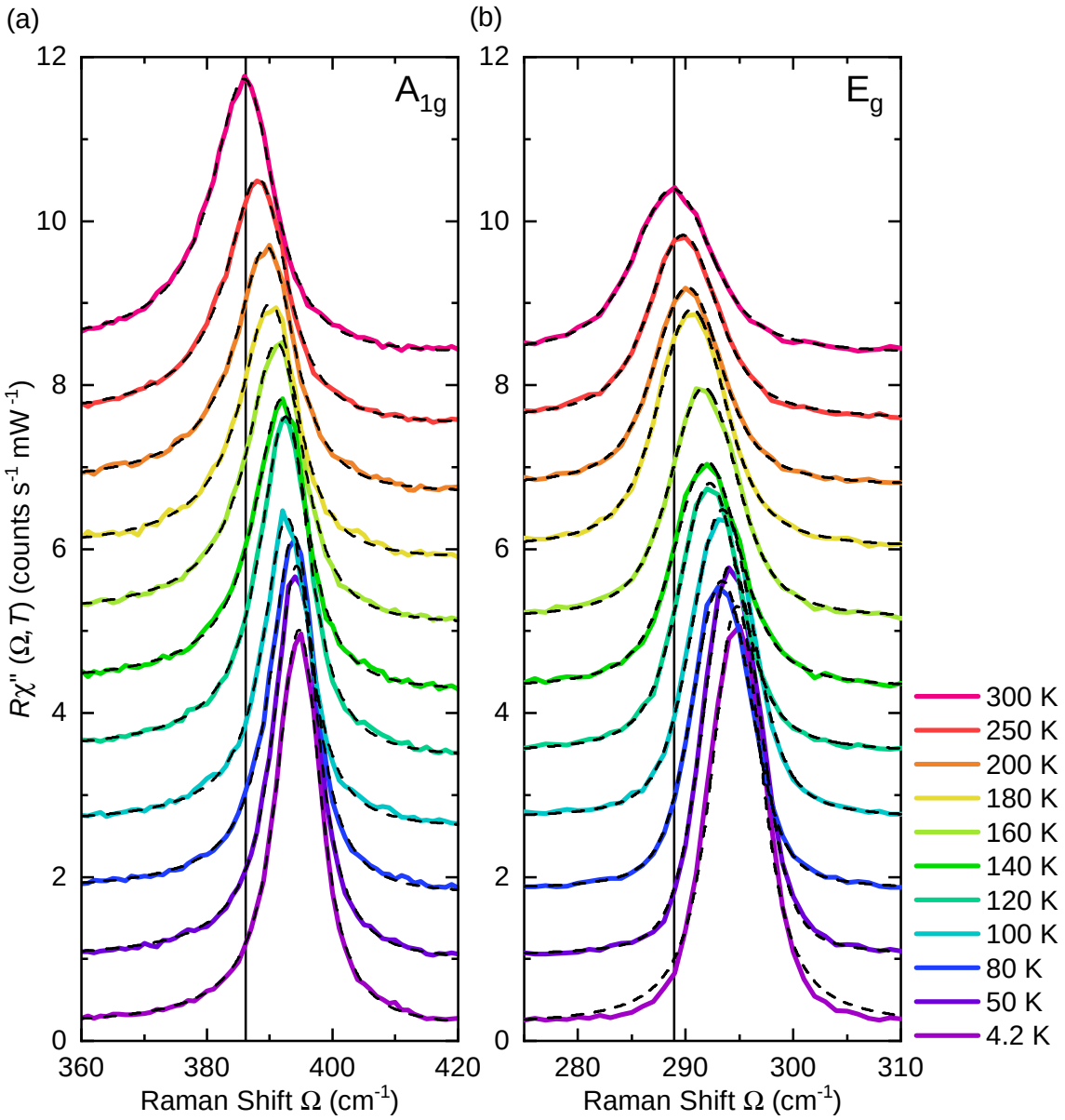

Figure 6.1.4.: Raman-active phonons of $Co_3Sn_2S_2$. Panel (a) and (b) show the best fit of the theoretical curves to the Raman-active A_{1g} and E_g phonon modes, respectively, at temperatures as indicated by the color bar. The solid lines represent the experimental data while the dashed lines indicate the theoretical curves. The data are consecutively offset by 1.0 cts/(s mW). Since the A_{1g} phonon line shows an asymmetry, a Fano function convoluted with a Gaussian distribution was used for fitting in order to account for the resolution of the spectrometer (Eq. 6.5 [105]). The E_g phonon line is symmetric, therefore a Voigt function was used, which is a Lorentzian convoluted with a Gaussian.

tion temperature $T_C = 180$ K $Co_3Sn_2S_2$ undergoes a transition from a paramagnetic material to an out-of-plane ferromagnetic material with ordered Co spins in the Kagome layer. Since the spin-phonon coupling seems to be significant, this transition is reflected in the behaviour of the phonons. This is the reason, why the phonon linewidth cannot be described by a single set of parameters in the whole temperature range. There is no obvious change

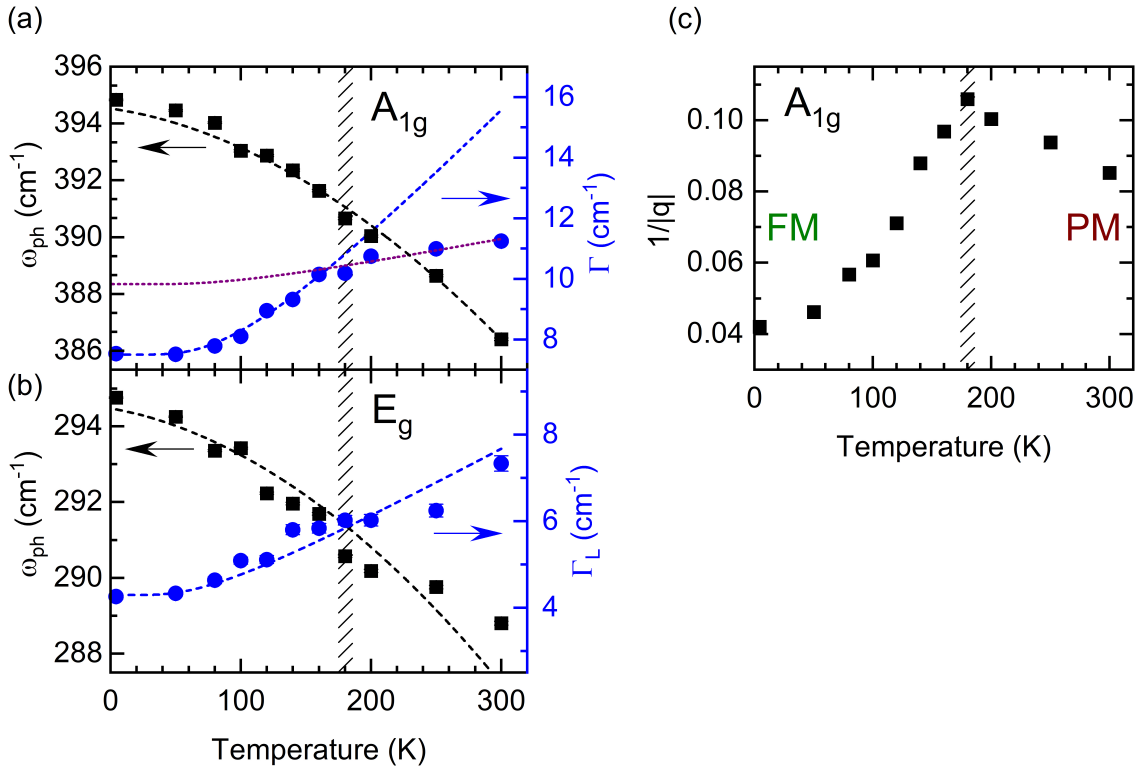

Figure 6.1.5.: Raman-active phonon modes as a function of temperature in $Co_3Sn_2S_2$. The dashed area indicates the phase transition temperature $T_C = 180$ K. (a) and (b) Temperature-dependence of the phonon energies ω_{ph} and linewidths Γ. The dashed black curve indicates the fitting of the phonon energy. The dashed purple and blue curves depicts the fit of the phonon linewidths. The dashed blue line in (a) indicates the fitting of the phonon linewidth for temperatures below the phase transition temperature $T_C = 180$ K, while the dashed purple line was fitted for temperatures above T_C. (c) Temperature-dependent asymmetry factor $1/|q|$ of the A_{1g} phonon line obtained from the fitting with a Fano function. The ferromagnetic (FM) phase and the paramagnetic (PM) phase are indicated in dark green and dark red, respectively.

in phonon energy and linewidth near T_C for the E_g phonon line as shown in Fig. 6.1.5 (b). The asymmetry factor $1/|q|$ of the A_{1g} phonon line [Fig. 6.1.5 (c)] increases slightly above T_C upon cooling, reaches a peak at T_C and decreases significantly below T_C. The fitting parameters of the phonons are listed in Tab. 6.1.2.

Phonon	A_{1g}	E_g
$\lambda_{\text{ph-ph},i}$	$0.85 \pm 0.03, 0.12 \pm 0.04$	0.40 ± 0.03
γ	$2.29 \pm 0.05, 2.41 \pm 0.06$	2.86 ± 0.20

Table 6.1.2.: Coupling parameters of $Co_3Sn_2S_2$. There are two Raman active phonons in $Co_3Sn_2S_2$ in the A_{1g} and E_g channel, respectively. Fitting the phonon linewidth with Eq. 6.2 provides the phonon-phonon coupling parameters $\lambda_{\text{ph-ph},i}$. The Grüneisen constants γ are obtained by fitting the temperature-dependent phonon energies with Eq. 6.3. The first values of the A_{1g} phonon mode correspond to the data below $T_C = 180$ K and the latter values to the fitted values above T_C.

The Grüneisen parameters γ_i of $Co_3Sn_2S_2$ for the A_{1g} phonon mode is $\gamma_{A_{1g},1} = 2.29 \pm 0.05$, if the phonon energy below the phase transition T_C is taken into account and $\gamma_{A_{1g},2} = 2.41 \pm 0.06$ for the data above the transition temperature $T_C = 180$ K. The Grüneisen parameters γ_i for the E_g phonon mode is $\gamma_{E_g} = 2.86 \pm 0.20$. Although $\lambda_{\text{ph-ph},i}$ of the A_{1g} phonon mode changes significantly at T_C, the Grüneisen parameters γ_i do not change significantly. The phonon energy and therefore the phonon shift as a function of temperature are dominated by the first order contribution $\Delta_i^{(1)}(T)$. For the E_g phonon mode the first order contribution $\Delta_i^{(1)}(T)$ dominates the phonon energy as well.

Spectra at very high energies are expected to be temperature independent if for example interband transitions or luminescence are ignored. To check the variation or stability of the spectral weight in the high-energy limit, the sums of the measured intensities at $3000 - 3600$ cm^{-1} were calculated and are plotted in Fig. 6.1.6. The blue points describe the sum of intensities of the E_g channel as a function of temperature. The data points are distributed around a constant value (represented as the dashed black line), which means that the spectral weight is nearly constant above 3000 cm^{-1}. The pink data points on the other hand describe the sum of intensities of the A_{1g} channel. These data points behave differently compared to the E_g data. The dashed grey line serves as a guide to the eye. Below 100 K they appear to be nearly constant. Between $100 - 200$ K they vary linearly and become constant again above 200 K. Comparing these characteristic temperatures to the transition temperatures in $Co_3Sn_2S_2$, there might be correlation between the change of the magnetic state and the slope of the sum of intensities in A_{1g} channel.

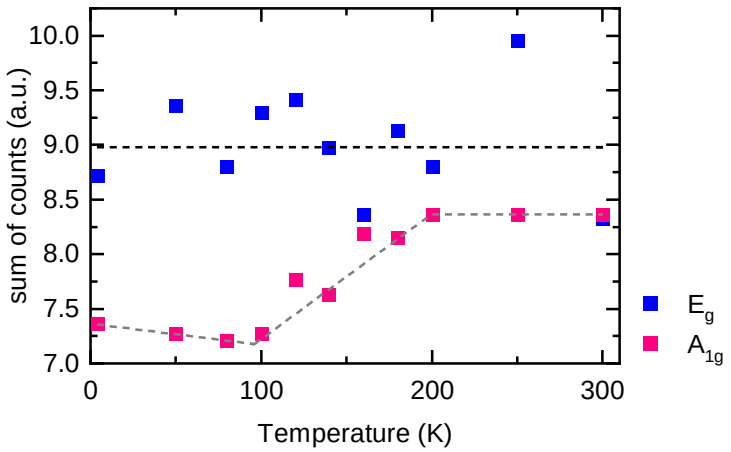

Figure 6.1.6.: The intensity values at energies between $3000 - 3600$ cm^{-1} were summed up for A_{1g} (pink data points) and E_g (blue data points). The dashed black line and the grey dashed line serve as a guide to the eye.

The results of Fig. 6.1.6 allow us to adjust the spectra in a way that they match above 3000 cm^{-1}. Now we determine the differences of the spectra presented in Section 5.1.2. These are computed as $\Delta\chi''_\mu(\Omega, T) = \chi''_\mu(\Omega,\ T) - \chi''_\mu(\Omega,\ 200\,\text{K})$ and can be seen exemplarily for 180 K (light green) and 4.2 K (purple) in Fig. 6.1.7 (a) and (b) in A_{1g} and E_g symmetries,

respectively. The difference spectra were integrated in order to be able to compare the temperature-dependent change of the spectral weight, in A_{1g}, E_g and $A_{1g} + E_g$ symmetries. The positive part $\int_{\Omega \in \Delta\chi'' > 0} \Delta\chi''_\mu(\Omega, T) d\Omega$ (shown in Fig. 6.1.7 as purple area) and negative part $\int_{\Omega \in \Delta\chi'' < 0} \Delta\chi''_\mu(\Omega, T) d\Omega$ (shown in Fig. 6.1.7 as dark green area) parts in the difference spectra are discussed separately.

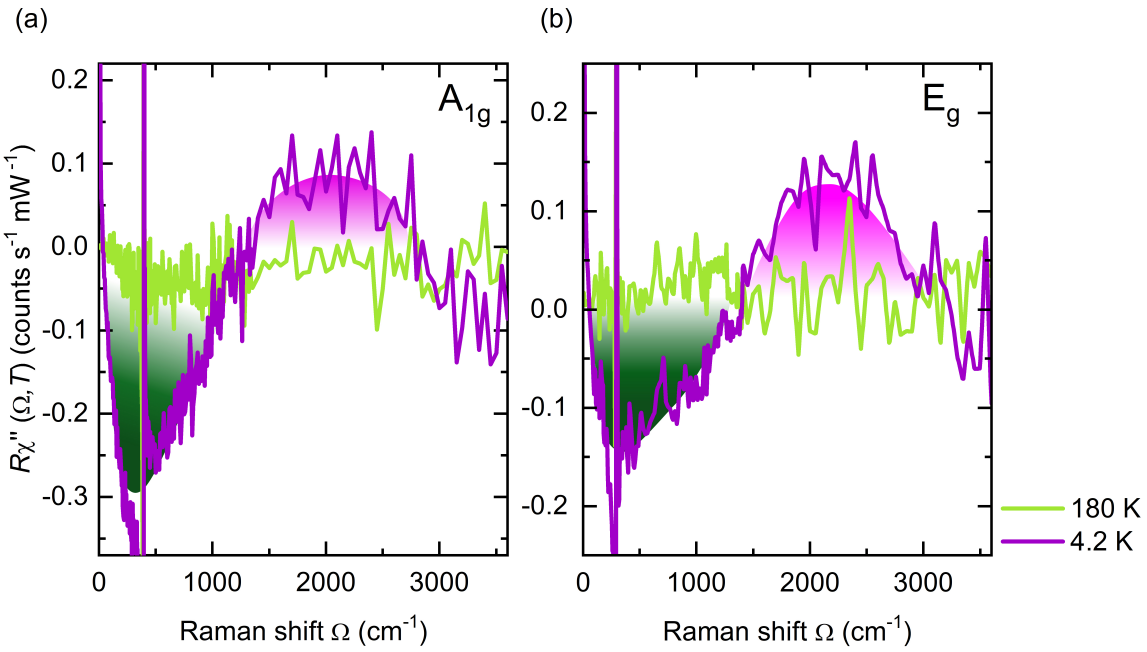

Figure 6.1.7.: Temperature-dependent electronic Raman response of $Co_3Sn_2S_2$. The spectra show the difference between the indicated temperatures and 200 K in the (a) A_{1g} and the (b) E_g symmetries. The green regions and the pink regions indicate the negative and positive intensity of the difference spectra respectively.

The magnitudes of the resulting integrals are pictured in Fig. 6.1.8 as dark green squares for the negative intensity regions and purple squares for the positive intensity regions. The decay and the increase of the integrated spectral weight decrease in both A_{1g} and E_g symmetries with increasing temperature. Both the loss and the increase of the integrated spectral weight seem to disappear above T_C, since they are decreasing monotonically. As already mentioned while introducing the Raman spectra of $Co_3Sn_2S_2$ in Section 5.1.2, the loss of the spectral weight at the low energy range is larger than the increase at high energy range in A_{1g} symmetry, and vice versa in E_g symmetry. There is no sum rule in Raman, so the loss and increase of the spectral weight in one spectrum are not necessarily equal. The sum of the spectra ($A_{1g} + E_g$) in Fig. 6.1.8 (c) describes a linear behaviour in both the loss and increase of the spectral weight. At 100 K the green curve exhibits a hump while the purple curve shows a dip. The difference in spectral weight redistribution in the different channels A_{1g} and E_g hints the anisotropic electronic structure in $Co_3Sn_2S_2$.

The main question in $Co_3Sn_2S_2$ is: Does the magnetism arise from itinerant or from localized electrons? Taking a look at the band structure (c.f. Section 2.1.2) reveals, that due

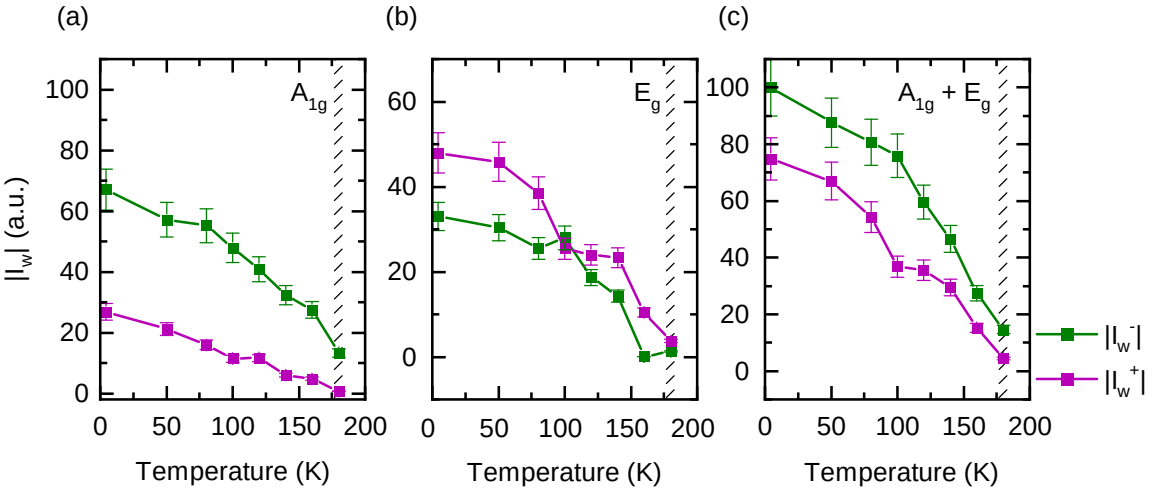

Figure 6.1.8.: Temperature-dependent electronic Raman response of $Co_3Sn_2S_2$ in the A_{1g} and the E_g symmetries. (a), (b), and (c) Temperature dependence of integrated spectral weight in the A_{1g}, E_g, and $A_{1g}+E_g$ symmetries. The positive (purple points) and negative (dark green points) intensity regions are integrated separately. The error bars are given by 10% of the integrated area. The hatched ranges indicate the ferromagnetic phase transition.

to the ferromagnetic phase transition the spin up and spin down bands split. The spin-up bands cross the Fermi level and therefore lead to a metallic character of the sample. The spin-down band on the other hand opens a gap of approximately 0.35 eV and shows an insulating character. Since the electrons, which come from the correlated Co $3d$ orbitals, are itinerant [108] and the band structure shows a metallic behaviour for the spin-up bands, the magnetism seems to have an itinerant origin. To test this thesis, Raman signatures of $Co_3Sn_2S_2$ were compared with the following features of the different origins of magnetism. As already introduced in Section 3.2 Raman spectra with local moments show a well-defined peak, which exhibits a weak but continuous temperature dependence. In contrast in Raman spectra of itinerant systems a gap opens at low energies and at the same time intensity accumulates at higher energies [85, 86, 89]. Both symmetries show a redistribution of spectral weight. In A_{1g} a gap opens below 1200 cm^{-1} and in E_g below 1350 cm^{-1} while intensity is redistributed to above these values. Comparing this behaviour to the Raman signatures found in $BaFe_2As_2$ [89] and La_2CuO_4 [109], $Co_3Sn_2S_2$ shows significant similarities to $BaFe_2As_2$. Therefore $Co_3Sn_2S_2$ exhibits the Raman signatures of an itinerant magnet. This conclusion agrees with the information obtained from the band structure.

In the following, the aim is to identify if either the spin (spin-phonon (sp-ph) coupling) or the charge (electron-phonon (el-ph) coupling) channels couple to the phonon in $Co_3Sn_2S_2$ leading to an asymmetric phonon line in the A_{1g} symmetry. Due to the existence of a ferromagnetic phase transition, the sp-ph coupling could originate from the generation of spin channels meaning phonons can directly couple to spins. If sp-ph coupling occurs, a renormalization of the phonon energy and linewidth occurs and the phonon line stays symmetric. The renormalization leads to phonon softening in the ferromagnetic systems

and hardening in the antiferromagnetic ones [110]. Since the phonon line should be symmetric, which is not the case in $Co_3Sn_2S_2$, and no renormalization of the A_{1g} phonon was found, the phonon most likely does not couple to the spin channels. The el-ph coupling can origin in the charge channel and therefore, arises from intra- or interband transitions with a phonon, which is expected in some special systems with low-lying excitations. To this end, the energy scale of these low-lying excitations needs to match the phonon energy. The first possibility for low-lying excitations in $Co_3Sn_2S_2$ are the Weyl points, which are located 60 meV [30, 38] above and below the Fermi level, which means the energy scale of the low-lying excitation is larger than 120 meV. This is much higher than the A_{1g} phonon energy (48.8 meV), but the transition can still be possible in this energy range due to thermal excitations at higher temperatures [111]. The second possible mechanism for the generation of el-ph coupling through charge channels could be the existence of a flat band. In $Co_3Sn_2S_2$ the energy scale of the flat band (-8 meV in scanning tunneling microscopy/spectroscopy [43] and ≈ 30 meV in optical conductivity [44]) is smaller than the A_{1g} phonon energy. But, if the flat band does exist in a reasonable energy range, it is likely to enhance the el-ph coupling.

In $Co_3Sn_2S_2$, the A_{1g} phonon mode stems from the vibration of the S atoms. The bands near the Fermi energy E_F derived from the Co $3d$ orbitals change considerably, if the S atoms vibrate, since the tetrahedral coordination of the S atoms with the Co atoms contribute to the electronic density of states. This vibration could change the energy scale of one of the mentioned flat bands leading to a high density of states close to E_F enhancing the coupling of the phonons to the 3d electrons of Co. This el-ph coupling leads to the observed asymmetric nature of the A_{1g} phonon mode represented by the asymmetry factor $1/|q|$ in Fig. 6.1.5 (c). Upon cooling the thermal excitation of electrons decreases leading to a higher occupation of the peak in the density of states. Therefore, the el-ph coupling increases for lower temperatures resulting in a higher asymmetry factor $1/|q|$, peaking at the transition temperature. As soon as the gap starts opening below T_C, electrons get bound to lower energy states reducing the amount of electrons participating in the el-ph coupling and hence, also the asymmetry factor $1/|q|$. The latter saturates at a value above zero for $T \to 0$ due to the residual metallic character of $Co_3Sn_2S_2$. Thus, the el-ph coupling in $Co_3Sn_2S_2$ could be flat band driven, but suppressed due to magnetic ordering below the transition temperature.

6.1.3. CsV_3Sb_5

The Kagome metal CsV_3Sb_5 was recently discovered by Ortiz *et al.* [21]. CsV_3Sb_5 is a quasi-2D material, which belongs to the space group $P6/mmm$. The hexagonal crystal structure with V-Sb layers intercalated by Cs atoms consists of a structurally perfect 2D kagome lattice of vanadium. As for all Kagome metals, the A_{1g} and the E_{2g} symmetries can be projected in RR- and RL-channel, respectively, which are pictured in Fig. 6.1.9 (a) and (b). The related Raman vertices of both symmetries for scattering from charge excitations

are shown in Fig. 6.1.9 (c), (d), (e), and (f). The first order A_{1g} symmetry mainly maps the Γ point, while the second order A_{1g} symmetry also maps the M points. The first order E_{2g} symmetry on the other hand mainly projects the M points.

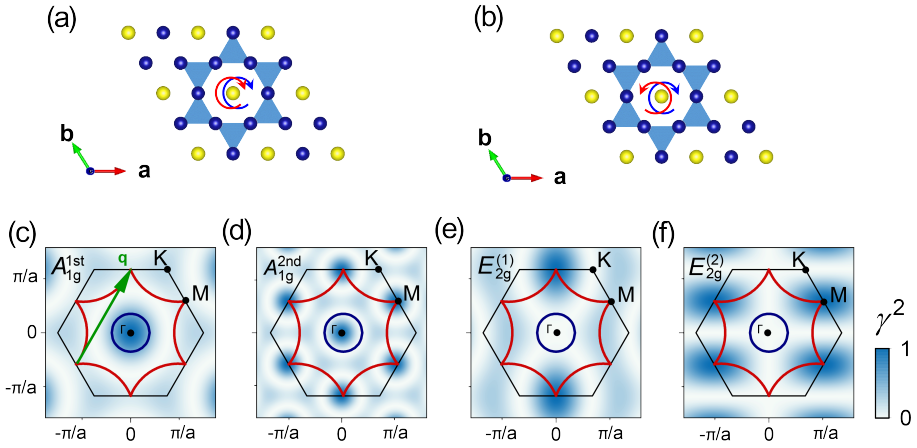

Figure 6.1.9.: Polarization configurations and related Raman vertices for electronic excitations in CsV_3Sb_5. The Kagome lattice of VSb layers with the polarization configurations of (a) A_{1g} and (b) E_{2g} symmetries. The color mapping in (c) and (d) shows the Raman vertices for the first- and second-order A_{1g} symmetry, respectively, while the color mapping in (e) and (f) picture the first order E_{2g} symmetry. The first Brillouin Zone is displayed by the black hexagon. The red and blue lines indicate the Fermi pockets. The green arrow in (c) highlights the Nesting vector q, which links two M points [112].

Electronic Continuum

Fig. 6.1.10 presents the polarization-dependent Raman spectra above (green line at 103 K) and below (purple line at 13 K) $T_{CDW} = 94$ K in the range from 50 cm^{-1} to 3600 cm^{-1} in A_{1g} [Fig. 6.1.10 (a)] and E_{2g} [Fig. 6.1.10 (b)] symmetry. In both symmetries the opening of a gap is observed. The spectra measured above and below T_{CDW} cross each other at 1600 cm^{-1} and 1550 cm^{-1} in A_{1g} and E_{2g}, respectively. The redistribution of spectral weight to higher energies is slightly stronger in the A_{1g} than in the E_g symmetry and decreases with warming up the sample. It disappears above the CDW critical temperature $T_{CDW} = 94$ K (compare Fig. 5.1.5). The gap energy is identified with the crossing points as 99.2 meV in A_{1g} and 96.1 meV in E_{2g}. This identification is plausible but not supported by theory. Yet, the energies are comparable to the results from optical spectroscopy and ARPES measurements [113–115]. The CDW gap is expected to appear at the M points as electron pockets are located at this point in k-space. The Raman vertices in Fig. 6.1.9 show, that only measurements in E_g map the M points. A gap-like feature can also be seen in A_{1g} channel, although the first order A_{1g} Raman vertex (Fig. 6.1.9 (c) mainly projects the excitations at Γ point. Probably, one needs to take the second-order A_{1g} Raman vertex into account as well, which does map the M points. Therefore, the second-order Raman vertex is not negligible.

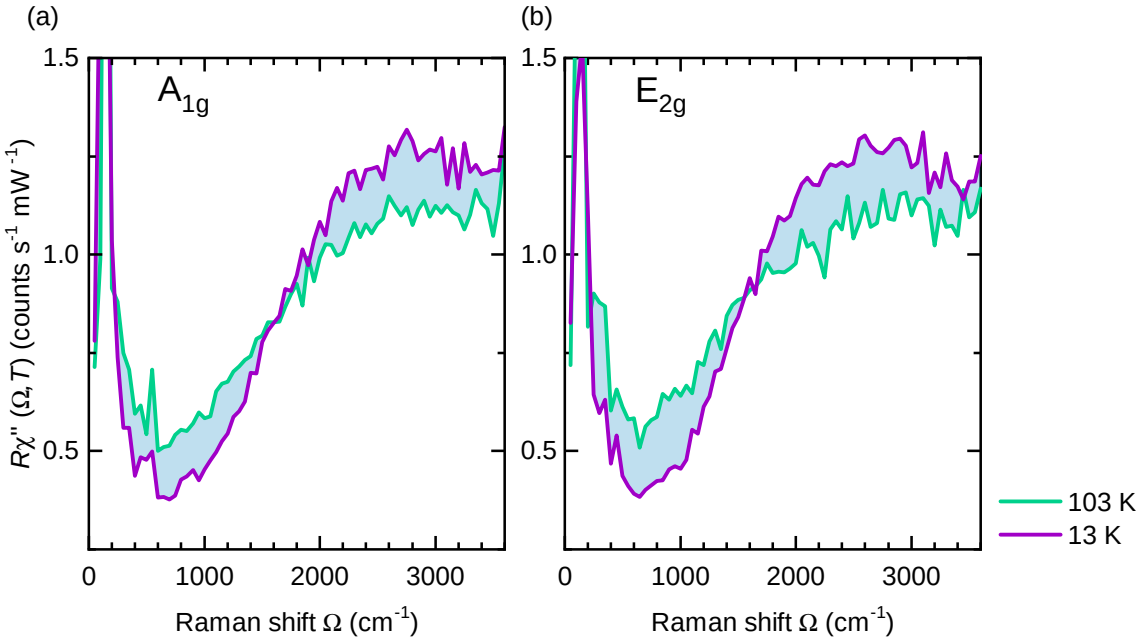

Figure 6.1.10.: CDW gap excitation in (a) A_{1g} and (b) E_{2g} symmetry of CsV_3Sb_5 at temperatures as indicated. The redistribution of the spectral weight of the Raman response above (green curve) and below (purple curve) $T_{CDW} = 94$ K is highlighted in light blue.

Lattice Excitations

Chen *et al.* [116] have identified two strong phonon lines, one in A_{1g} (138.2 cm^{-1} at 13 K) and one in E_{2g} (119.5 cm^{-1} at 13 K) symmetry. In addition to those lines Fig. 6.1.11 shows the appearance of several new lines below the CDW critical temperature $T_{CDW} = 94$ K. The lattice distortion occurring in CsV_3Sb_5 below T_{CDW} folds the phonon band by a vector q. This vector q links to the nesting points (M points in CsV_3Sb_5). If this happens, phonons at zone boundaries are folded towards the nesting point and therefore become Raman active. The charge density wave transition also leads to the fact, that the ideal kagome structure is energetically unstable at zero temperature. Tan *et al.* [117] found with DFT calculations the favoured structure: the so-called inverse star-of-David (ISD) [118]. Due to the change in structure, the V atoms move from 3g (1/2, 0, 1/2) to 12q (x, y, 1/2). This structure change and the folding of the phonon band by a vector q due to the lattice distortion would entail the appearance of eight additional Raman active modes. These phonons are called zone-folded phonons [119, 120]. Two phonons should appear in A_{1g}, four in E_{2g} and two in E_{1g}. If one only takes the phonons exhibiting ordinary phononic behaviour into account, the number of measured phonons in A_{1g} does match the expected number of ordinary phonons in both A_{1g} and E_{2g} symmetry.

The phonons in the A_{1g} and the E_{2g} symmetry were observed at the temperatures indicated and are presented consecutively offset by 1 cts/(s mW) for clarity. In A_{1g} three additional phonon lines reemerge with energies 44.3 cm^{-1} [$A_{1g}(1)$], 104.4 cm^{-1} [$A_{1g}(2)$]

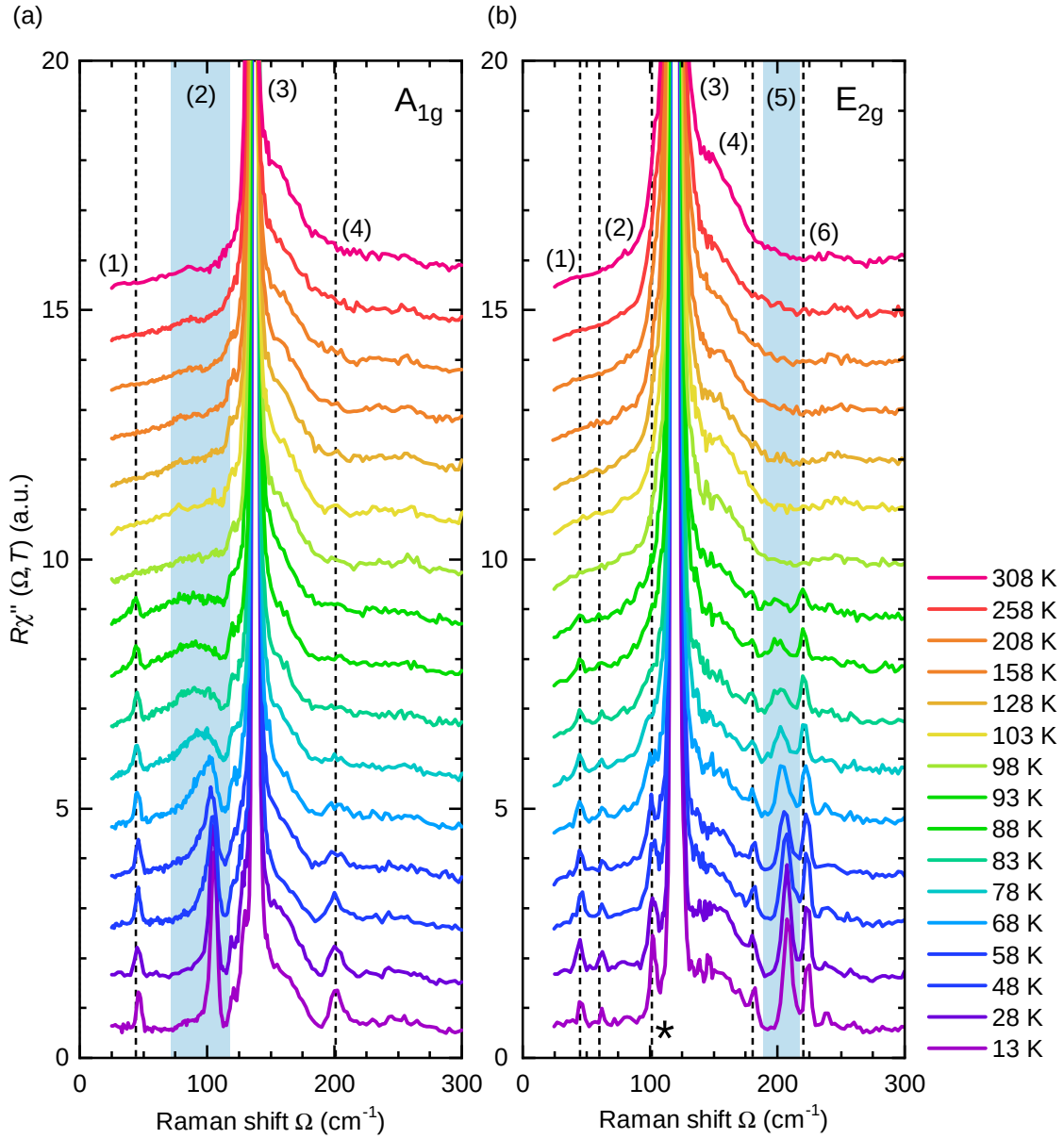

Figure 6.1.11.: The temperature-dependent Raman spectra of CsV_3Sb_5 in the (a) A_{1g} and (b) E_g symmetry at temperatures as indicated, respectively. The data are consecutively offset by 1.0 cts/(s mW) each for clarity. The dashed black lines mark the energy of the phonon, for the temperature, where it initially manifests. The light blue areas highlight the evolution and the position of the amplitude modes in Ω.

and 201.1 cm^{-1} [$A_{1g}(4)$] at 13 K. In E_{2g} even six additional phonon lines appear with energies 45.7 cm^{-1} [E_{2g} (1)], 62.4 cm^{-1} [E_{2g} (2)], 102.0 cm^{-1} [E_{2g} ($*$)], 181.5 cm^{-1} [E_{2g} (4)], 208.3 cm^{-1} [E_{2g} (5)] and 223.9 cm^{-1} [E_{2g} (6)] at 13 K. The peak marked with an asterisk in Fig. 6.1.11 (b), which appears on the low-energy side of the $E_{2g}(3)$ phonon will not be considered further. The third peak in the A_{1g} symmetry and the sixth peak in E_{2g} behave differently compared to the other phonons. These peaks and their evolution as a function of temperature are highlighted with the light blue area. First, both peaks appear as a broad

hump, shift towards higher energies, and sharpen drastically with decreasing temperature. The shape of the third peak in the A_{1g} symmetry is asymmetric, the sixth peak in the E_{2g} symmetry is symmetric. As already mentioned in Chapter 5, the shoulder of the $A_{1g}(3)$ and the $E_{2g}(4)$ phonon lines is probably resulting from contamination of the sample surface. Before fitting all symmetric peak lines with a Voigt function (Eq. 4.1) and the asymmetric peak line with a Fano function resulting from convoluted with a Gauss function (Eq. 6.5), a phenomenological curve, which describes the electronic continuum, was subtracted from the data (c.f. Section 3.2).

The resulting temperature-dependent peak energies $\omega(T)$ and the linewidth Γ_L of the A_{1g} and the E_{2g} peak lines are illustrated in Fig. 6.1.12 and Fig. 6.1.14, respectively and $\lambda_{\text{ph-ph},i}$ is listed in Table 6.1.3. The hatched areas illustrate the CDW critical temperature $T_{CDW} = 94$ K.

Phonon	$A_{1g}(1)$	$A_{1g}(2)$	$A_{1g}(3)$
$\lambda_{\text{ph-ph},i}$	0.26 ± 0.09	2.95 ± 0.89	0.67 ± 0.09, 0.09 ± 0.01
Phonon	$E_{2g}(1)$	$E_{2g}(2)$	$E_{2g}(3)$
$\lambda_{\text{ph-ph},i}$	0.37 ± 0.2	1.33 ± 3.55	0.24 ± 0.02
Phonon	$E_{2g}(4)$	$E_{2g}(5)$	$E_{2g}(6)$
$\lambda_{\text{ph-ph},i}$	0.67 ± 1.23	1.80 ± 0.59	6.86 ± 2.73

Table 6.1.3.: Coupling parameters of CsV_3Sb_5. Below the transition, there are four Raman active phonons in the A_{1g} and seven Raman active phonons in the E_{2g} channel, respectively. Fitting the phonon linewidth with Eq. 6.2 provides the phonon-phonon coupling parameters $\lambda_{\text{ph-ph},i}$. The first value for the $A_{1g}(3)$ phonon mode belongs to the data ranging below T_{CDW} and the latter value to the data above T_{CDW}.

Fig. 6.1.12 shows the A_{1g} results for phonon energies and widths. Since the peaks (1), (2) and (4) in the A_{1g} channel exclusively appear below T_{CDW}, only the parameters for temperatures below 100 K are shown. All phonon lines in the A_{1g} channel shift to higher energies, as already mentioned, except for the $A_{1g}(4)$ phonon. This phonon has a constant energy of ≈ 201 cm^{-1}. While cooling the $A_{1g}(3)$ phonon shifts linearly to higher energies above T_{CDW} and below T_{CDW}, the slope behaves similar to that of the other lines. In general, the signal of the different peaks is weak, which is problematic for fitting both, the Voigt function and the convoluted Fano function, which are pictured as solid red lines. Therefore, the error bars especially in Fig. 6.1.12 (b), (d) and (f) are substantial compared with the value itself. In (b) a Voigt function and $\lambda_{\text{ph-ph}}(A_{1g}(1)) = 0.26 \pm 0.09$ describe the data satisfactorily.

The second peak in Fig. 6.1.11 (a) shows a totally different behaviour than the others and will be described in the next subsection. In the phonon linewidth of $A_{1g}(3)$ an anomalous behaviour can be found. Since the data below T_{CDW} shows a completely different slope than above, the analysis was split at T_{CDW}. The dashed pink line represents the data below

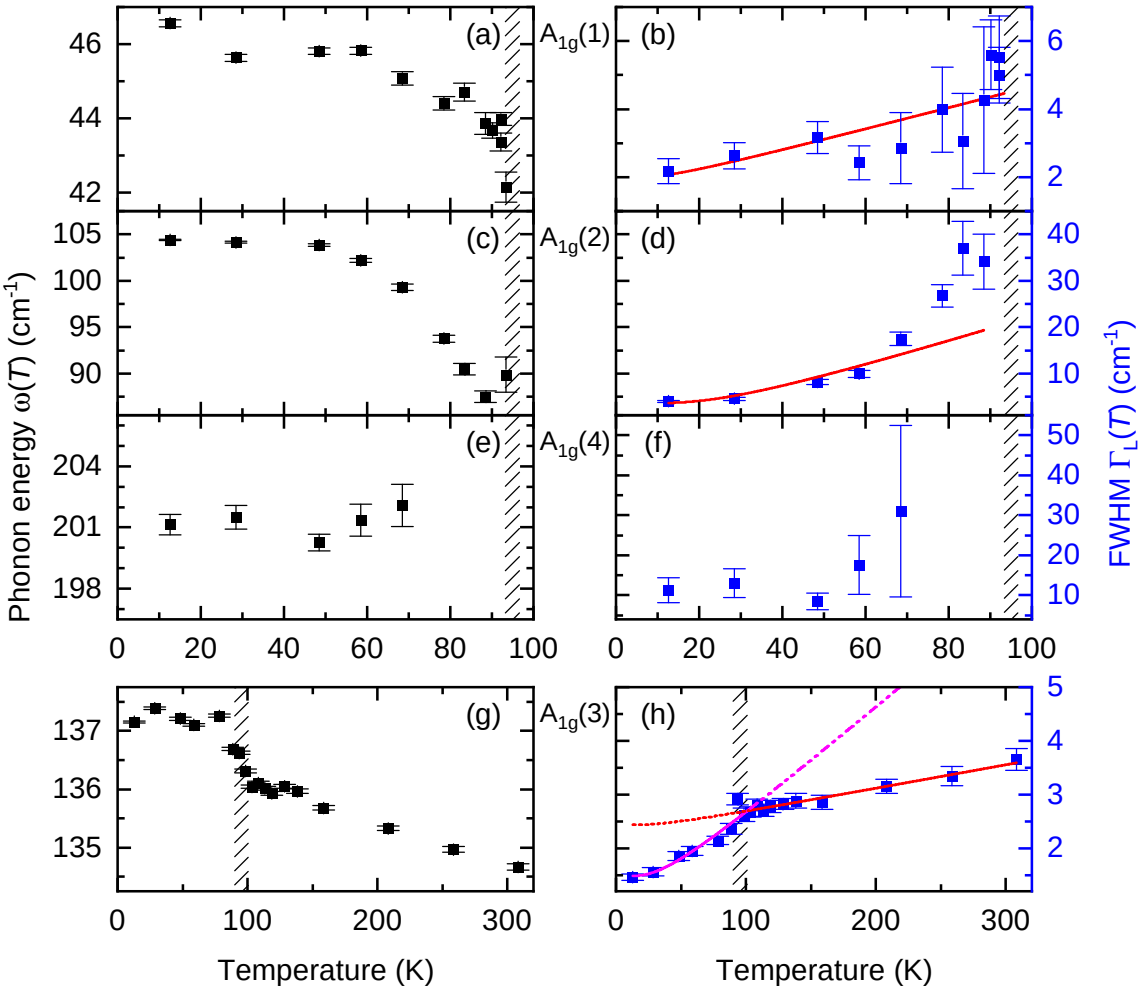

Figure 6.1.12.: Phonon energies ω (black) and Lorentzian widths Γ_L (blue) of CsV_3Sb_5 in A_{1g} symmetry. The hatched area indicates the CDW critical temperature $T_{CDW} = 94$ K. The labels of the phonon lines correspond to the numbering in Fig. 6.1.11 (a). The peaks (1), (2) and (4) only appear below the transition temperature T_{CDW}. The dashed pink line in (h) indicates the variation with temperature of the phonon linewidth of the $A_{1g}(3)$ phonon for temperatures below T_{CDW}, while the dotted red line was obtained above T_{CDW} using Eq. 6.2 in both cases. The signal of the $A_{1g}(4)$ phonon is to weak compared to the noise, so the fit did not converge. The parameters are derived by fitting procedures as described in the text.

T_{CDW} and the dotted red line those above T_{CDW}. The $\lambda_{\text{ph-ph}}(A_{1g}(3))$ parameter for the high temperature data exhibits a drastically smaller anharmonic decay of phonons compared to the low temperature data. The fourth phonon is barely above background noise, entailing large error bars on the line widths.

Since the order transition of the CDW is not clear, a hysteresis of the phonon energy and the linewidth at the phase transition temperature might occur in Raman spectra. Therefore data from 50 cm^{-1} to 180 cm^{-1} were measured with a step width of $\Delta\Omega = 1$ cm^{-1} in RR-polarization sequentially warming up and cooling down with a finer temperature resolution around the transition temperature T_{CDW}. The data received shows the strong

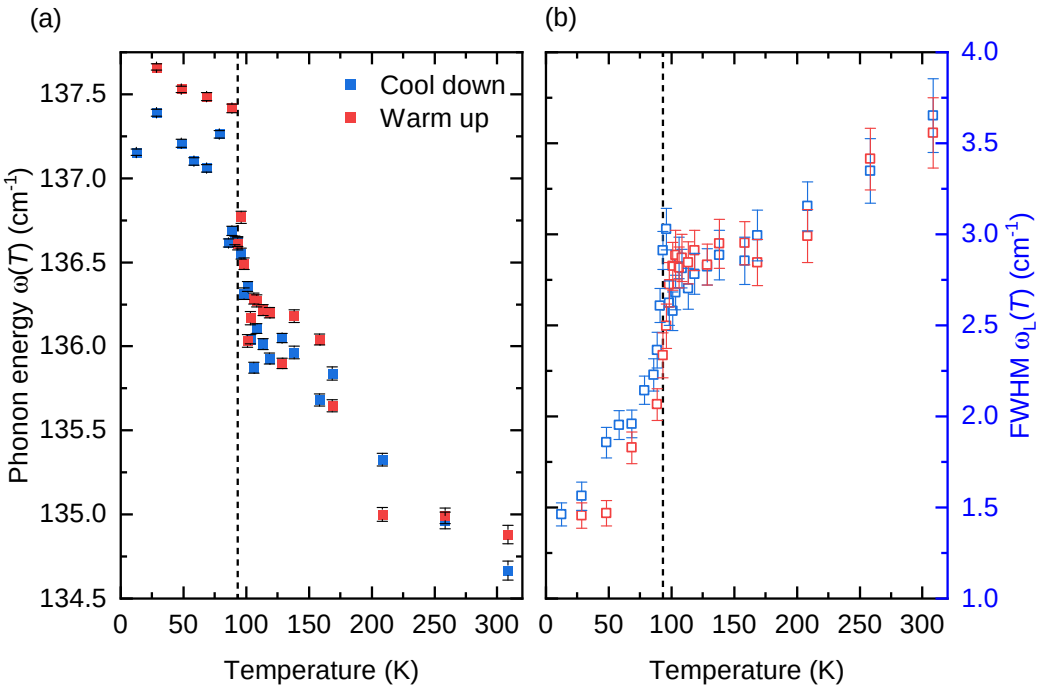

Figure 6.1.13.: (a) Phonon energies $\omega(T)$ and (b) Lorentzian widths Γ_L of CsV_3Sb_5 in A_{1g} symmetry. The data was measured sequentially cooling down from 308 K to 13 K (blue spectra) and warming up from 13 K to 308 K (red spectra). The dashed lines indicate the CDW critical temperature $T_{CDW} = 94$ K. No Hysteresis was observed.

symmetric phonon line in A_{1g} at the energy 134.7 cm^{-1} at 308 K. The phonon energy $\omega(T)$ and the linewidth $\Gamma_L(T)$ are plotted in Fig. 6.1.13. The hatched line indicates T_{CDW}. In Fig. 6.1.13 (a), below 100 K the slope of the phonon energy $\omega(T)$ seems to be linear and almost constant above 100 K. However, the slope around the T_{CDW}, is much steeper. In Fig. 6.1.13 (b) the slope of $\Gamma_L(T)$ shows a similar behaviour. It gets steeper around T_{CDW} and flattens afterwards again. Above T_{CDW} the linewidth presumably shows the existence of anharmonic coupling. At $T = 0$ both the slope of the phonon energy and the slope of the linewidth disappear ($d\omega/dT = 0$). Moreover, the phonon energy $\omega(T)$ and $\Gamma_L(T)$ behave similarly while warming up and cooling down the sample. No sign of a hysteresis was observed in the Raman spectra obtained. Therefore, an argument can be made for either a second-order or a weak first-order phase transition. This conclusion is also supported by Li *et al.* [121].

Fig. 6.1.14 shows the energies ω and the linewidths Γ of the peaks in the E_{2g} channel. Since the peaks (1), (2), (4) (5) and (6) in the E_{2g} channel exclusively appear below T_{CDW}, only the parameters for temperatures below 100 K are shown. In E_{2g}, all peaks harden and sharpen while cooling down below T_{CDW}. Since phonon (2), (4) and (6) slowly accumulate spectra weight below T_{CDW} and are also rather low in intensity even at low temperature, they are hardly distinguishable from the background noise. This fact makes fitting difficult and leads to huge error bars. The phonon-phonon coupling parameter $\lambda_{ph\text{-}ph}(E_{2g})$

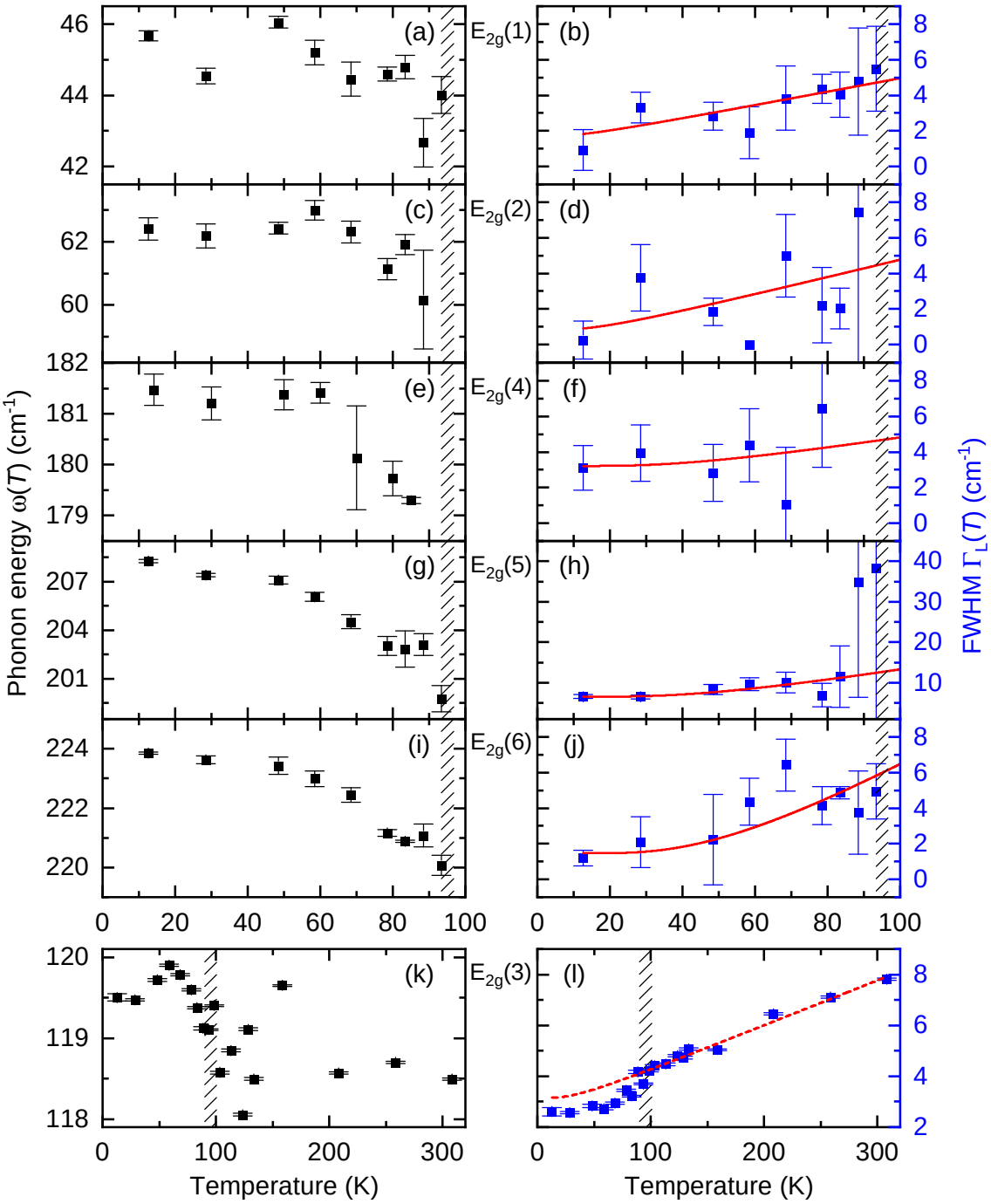

Figure 6.1.14.: Phonon energies ω (black) and Lorentzian widths Γ_L (blue) of CsV_3Sb_5 in the E_{2g} symmetry. The hatched area indicates the CDW critical temperature $T_{CDW} = 94$ K. The labels of the phonon lines correspond to the numbering in Fig. 6.1.11 (b). The dashed red line in (l) indicates the variation with temperature of the phonon linewidth of the E_{2g} (3) phonon for temperatures above T_{CDW}. The parameters are derived by fitting procedures as described in the text.

for these three phonons also reflects this problem. Phonon (1) with an energy around 44 cm^{-1} couples with a factor of $\lambda_{\text{ph-ph}}(E_{2g}(1)) = 0.37 \pm 0.2$ to the anharmonic decay of

phonons. Phonon (3) in E_{2g} [Fig. 6.1.14 (l)] shows anharmonicity above T_{CDW} and hence, can be described by Eq. 6.2. The corresponding phonon-phonon coupling parameter is $\lambda_{\text{ph-ph}}(E_{2g}(3)) = 0.24 \pm 0.02$. Below T_{CDW}, the same theoretical description does not suit the data, which leads to the conclusion, that this E_{2g} couples to the electrons of the gap as well.

Peak (5) in Fig. 6.1.14 (h) shows a similar behaviour as the peak in Fig. 6.1.12 (d). Here, a broad hump also shifts to higher energies and sharpens by a factor of 2 below T_{CDW} towards lower temperatures. The peak shifts from 199.8 cm^{-1} at 93 K to 208.3 cm^{-1} 13 K. The change in linewidth describes the evolution from a broad hump at 93 K to a sharp peak at 13 K. For temperatures close to the transition temperature, the hump slowly emerges from the background and making the determination of the width and position difficult. We extract $\lambda_{\text{ph-ph}}(E_{2g}(5)) = 1.80 \pm 0.59$, which is larger than one and thus physically questionable. Whether or not the magnitude of $\lambda_{\text{ph-ph}}(E_{2g}(5))$ indicates that the mode has an origin other than phononic remains open on the basis of the unstable fitting procedure.

6.1.4. Amplitude modes

The second peak in the A_{1g} symmetry starting to appear as a broad hump shifts to higher energies and sharpens drastically towards lower temperatures. This fact is reflected in the energies of this excitation. The peak shifts from 87.5 cm^{-1} at 88 K to 104.4 cm^{-1} at 13 K. Since the peak sharpens, also the linewidth changes by an order of magnitude. The experimental results cannot be described by a lineshape typical for a phonon, and we conclude that the mode is not a simple lattice vibration. This asymmetric peak in Fig. 6.1.11 (a) was investigated in two different samples to check the reproducibility.

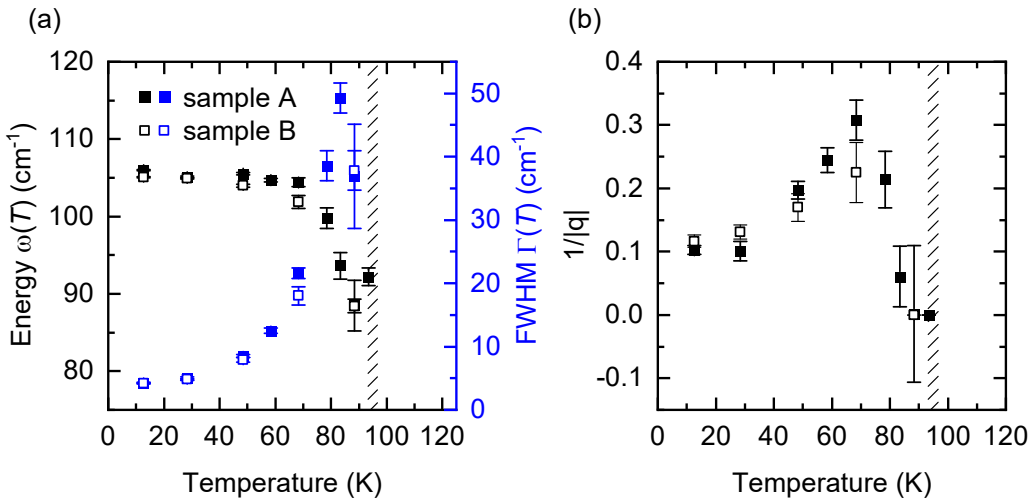

Figure 6.1.15.: (a) Mode energies ω (black) and linewidths Γ (blue) of CsV_3Sb_5 in the A_{1g} symmetry. (b) The temperature-dependent asymmetry factor $1/|q|$ of the A_{1g} amplitude mode line obtained from the fitting with a Fano function. The hatched area indicates the CDW critical temperature.

The corresponding mode energies ω and linewidths Γ of samples A and B are plotted in Fig. 6.1.15 (a). The hatched area indicates the CDW critical temperature. The temperature-dependence of the linewidth and the shift in energy are similar for both samples and much stronger than those of the other modes. Since the peak at temperatures close to T_{CDW} appears gradually as a function of decreasing temperature, the precise line shape is difficult to determine as apparent from the huge error in Fig. 6.1.15 (a). The asymmetry factor $1/|q|$ of the amplitude mode in A_{1g} symmetry is shown in Fig. 6.1.15 (b). Below T_{CDW}, the asymmetry factor $1/|q|$ of the amplitude mode first increases with decreasing temperature, reaches its highest value at 68 K and decreases again for $T \to 0$.

The two lines, which behave differently compared to the other phonon peaks are located at 104.4 cm^{-1} in the A_{1g} channel and 208.3 cm^{-1} in the E_{2g} channel at 13 K. These lines disappear and the corresponding linewidths increase drastically while warming up to T_{CDW}. This behaviour leads to the conclusion, that these are CDW-coupled amplitude modes (AM) [122], since collective excitations of the electrons can occur in a CDW-driven material. Similarly, two AMs were found in 2H-TaS_2 [123]. Here, the amplitude of the electron density wave is excited, which changes the polarizability and thus is Raman active [27]. In an almost perfect crystal an amplitude starts to rise below the CDW critical temperature at zero energy. Due to impurities this is not the case in CsV_3Sb_5 and hence, the amplitude mode starts to build up at the finite energy 87.5 cm^{-1} in A_{1g} and 199.8 cm^{-1} in E_{2g}. Interactions between amplitude modes and electrons can change the lineshape from a Lorentz distribution to a Fano distribution analogous to electron-phonon coupling. As it can be seen in Fig. 6.1.15 and Fig. 6.1.14 the A_{1g} AM is asymmetric and the E_{2g} AM is symmetric, respectively. More details of the Fano-fit can be found in Appendix C. Since the CDW gap shifts to higher energies for lower temperatures, a higher density of free charge carriers can be found there. This could lead to a higher coupling at the corresponding energies and a larger asymmetry. To my knowledge, it is the first observation of an asymmetric amplitude mode in all of the known CDW materials.

6.2. Tetraboride TmB_4

As already introduced in Section 2.2.1 the space group of TmB_4 is $P4/mbm$ (No. 127) and is part of the D_{4h} $(4/mmm)$ point group. This leads to the corresponding Raman tensors

$$A_{1g} = \begin{pmatrix} a & 0 & 0 \\ 0 & a & 0 \\ 0 & 0 & b \end{pmatrix},$$
$$B_{1g} = \begin{pmatrix} c & 0 & 0 \\ 0 & -c & 0 \\ 0 & 0 & 0 \end{pmatrix}, \text{ and} \tag{6.6}$$
$$B_{2g} = \begin{pmatrix} 0 & d & 0 \\ d & 0 & 0 \\ 0 & 0 & 0 \end{pmatrix}.$$

The Wyckoff positions of the Tm-atoms (4g), the B-atoms of the basal plane of the octaeder (8j), the apical B-atoms sitting on top of the pyramids (4e) and the dimer pairs (4h) entail five A_{1g}, four B_{1g} and four B_{2g} Raman-active phonons. According to the Raman tensors shown in Eq. 6.6 the A_{1g} phonons may be projected in RR- and both the B_{1g} and the B_{2g} phonons in RL-channel. A full symmetry analysis of TmB_4 at 100 K can be found in Appendix B.2.

With this information the peaks in Fig. 5.2.1 (a) can be identified as four of the five expected A_{1g} Raman-active phonons. In Fig. 5.2.1 (b) six peaks appear. In accordance with the symmetry analysis of TmB_4 in the energy range below 650 cm^{-1}, the peak at 120 cm^{-1} has been identified as a B_{2g} phonon. The phonon at 600 cm^{-1} contributes to the B_{1g} symmetry. The remaining four phonons at 660.6 cm^{-1}, 681.0 cm^{-1}, 982.1 cm^{-1}, and 1001.2 cm^{-1} are in either B_{1g} or B_{2g} symmetry since the symmetry analysis is limited to the range below 650 cm^{-1}. Therefore, only six of the eight expected $B_{1g} + B_{2g}$ Raman-active phonons can be seen. The seventh and eighth absent $B_{1g} + B_{2g}$ phonons are probably to weak in intensity to be detected with this experimental setup. These phonons are used as probes to investigate the crystal's response to different magnetic phases and their dependence on the orientation of the field.

6.2.1. Investigation of the Phase Diagram

In the following various cuts through phase diagram are studied with either constant magnetic field and changing temperature (c.f. Fig. 6.2.1) or vice versa (c.f. Fig. 6.2.4).

First, to scan horizontally through the phase diagram as pictured in Fig. 6.2.1, an external magnetic field of $B = 1$ T was applied during measurements at temperatures as indicated in Fig 5.2.1. To quantitatively analyze each phonon of the obtained data, a Voigt function

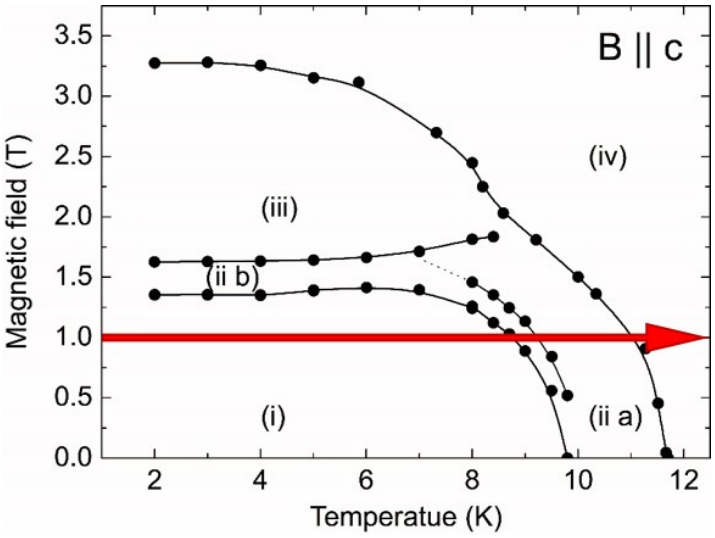

Figure 6.2.1.: Phase diagram of TmB_4 as a function of the temperature and the magnetic field. The numbering of the phases correspond to that in the phase diagram in Section 2.2.3. The red arrow indicates the parameter varied in the measurement. Here, the temperature was changed and the magnetic field was held constant at $B = 1$ T [24].

was used to fit the phonons (c.f. Section 4.2.3). The derived peak energies $\omega(T)$ (black points) and the linewidths $\Gamma_L(T)$ (FWHM) (blue points) are pictured in Fig. 6.2.2 and 6.2.3 in A_{1g} and $B_{1g} + B_{2g}$, respectively.

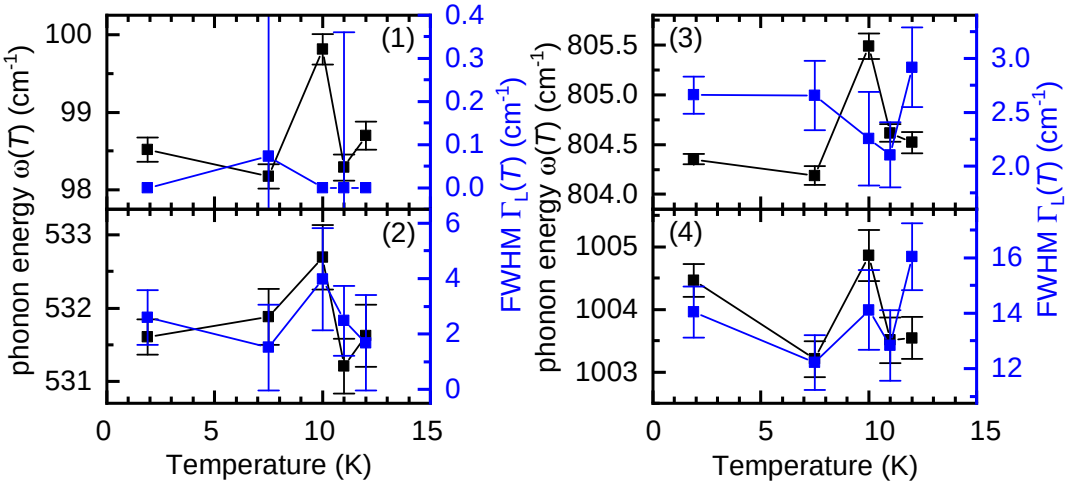

Figure 6.2.2.: Phonon energies ω (black) and Lorentzian widths Γ_L (blue) of TmB_4 in A_{1g} symmetry of measurements with an applied magnetic field $B = 1$ T at 1.8 K, 7.5 K, 10 K, 11 K, and 12 K. The labeling of the panels corresponds to the labeling of the phonon peaks in Fig. 5.2.1 (a).

In A_{1g} symmetry the four phonon modes are located at 98.5 cm^{-1} [$A_{1g}(1)$], 531.6 cm^{-1} [$A_{1g}(2)$], 804.4 cm^{-1} [$A_{1g}(3)$], and 1004.5 cm^{-1} [$A_{1g}(4)$] at 1.8 K as shown in Fig. 5.2.1 (a). The linewidths of all A_{1g} phonons ($A_{1g}(1) - (4)$ in Fig. 6.2.2 $(1) - (4)$, respectively) do only change in the small range $\Delta\Gamma_L = 1.8$ cm^{-1} in the observed temperature range. The energy

of the $A_{1g}(1) - (4)$ phonons is constant in the temperature range $T = [1.9, 12]$ K, except at 10 K. At 10 K all A_{1g} phonons shift by more than 1 cm^{-1}. At this temperature TmB_4 is in the Intermediate phase, which means that the sample shows short range ferromagnetic order and long range antiferromagnetic order. In all other magnetically ordered phases the phonon energy stays constant.

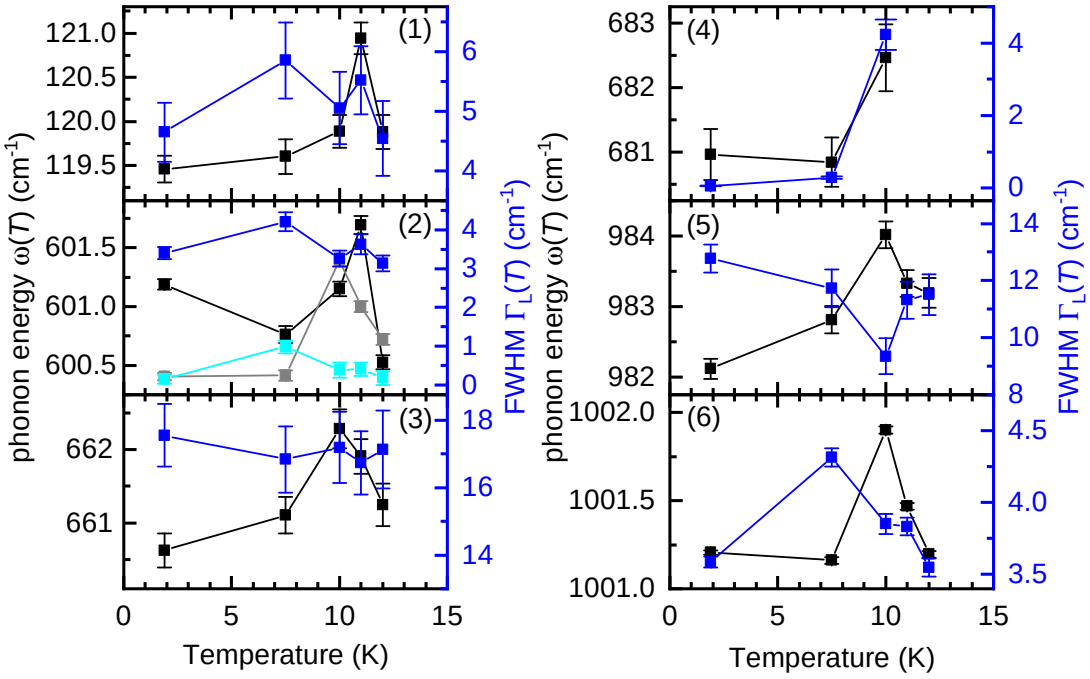

Figure 6.2.3.: Phonon energies ω (black) and Lorentzian widths Γ_L (blue) of TmB_4 in $B_{1g} + B_{2g}$ symmetry of measurements with an applied magnetic field $B = 1$ T at 1.8 K, 7.5 K, 10 K, 11 K, and 12 K. The labeling of the panels corresponds to the labeling of the phonon peaks in Fig. 5.2.1 (b). (2) The line at 660.6 cm^{-1} was measured with two different spectrometer positions which overlap in the range 581.25 cm^{-1} to 632.5 cm^{-1}. The data points plotted in cyan and grey were measured with the spectrometer in high-energy position.

In $B_{1g} + B_{2g}$ symmetry the six phonons are located at 119.5 cm^{-1} [RL(1)], 601.2 cm^{-1} [RL(2)], 660.6 cm^{-1} [RL(3)], 681.0 cm^{-1} [RL(4)], 982.1 cm^{-1} [RL(5)], and 1001.2 cm^{-1} [RL(6)] at 1.8 K as shown in Fig. 5.2.1 (b). The phonon excitation RL(4) at 681.0 cm^{-1} is located on the high-energy shoulder of the RL(3) phonon at 660.6 cm^{-1}. There are only three values for both the linewidth Γ_L and the phonon energy ω, since the intensity of the phonon mode at temperatures larger 10 K was to small for a meaningful fit. The measurements were performed in two steps, first the low energy part between 30.0 cm^{-1} and 632.5 cm^{-1} and then the high energy part between 581.25 cm^{-1} and 1142.5 cm^{-1}. This means that the line at 601.2 cm^{-1} is measured twice using different spectrometer positions. In Fig. 6.2.3 (2) the blue and black curves describe the peak at 601.2 cm^{-1} measured with the spectrometer in the low-energy position and the cyan and grey curves the peak at 601.2 cm^{-1} measured with the spectrometer in the high-energy position. The data points of the two different measurements do not coincide since the phonon is recorded on different

positions on the CCD detector. Since the same Gaussian width was used for the resolution the Lorentzian width of the phonon depends on the configuration, although it should be the way around. This is an artifact which cannot easily be eliminated in a controlled fashion. Various reasons which cannot easily be grasped may contribute including optical aberrations, misalignment of the detector or the resolution which depends on the grating angle.

The RL(3)-(6) phonon modes shift to higher energies at 10 K and shift back to lower energies for higher temperatures. The two modes RL(1) at 120.9 cm^{-1} [Fig. 6.2.3 (1)] and RL(2) 601.7 cm^{-1} [Fig. 6.2.3 (2)] from the low energy data exhibit the largest shift at 11 K. The linewidths of all phonons appearing in $B_{1g} + B_{2g}$ symmetry stay at an almost constant value. Only the linewidth of the RL(5) phonon varying between 982.1 cm^{-1} and 984.0 cm^{-1} [Fig. 6.2.3 (5)] is smaller by 30 % at 10 K.

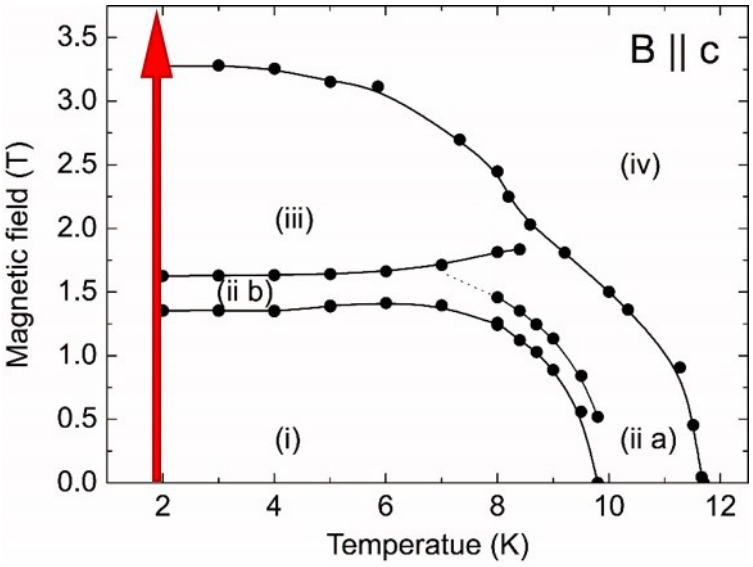

Figure 6.2.4.: Phase diagram of TmB_4 as a function of the temperature and the magnetic field. The numbering of the phases correspond to that in the phase diagram in Section 2.2.3. The red arrow indicates the changed parameter in the measurement. Here, the magnetic field was changed and the temperature was maintained at $T = 1.8$ K [24].

For the vertical scan as shown in Fig. 6.2.4, measurements were performed at the constant temperature $T = 1.8$ K and different magnetic fields as plotted in Fig. 5.2.3. For the quantitative analysis of the phonons a Voigt function was used (c.f. Section 4.2.3). The resulting peak energies $\omega(T)$ (black points) and the linewidths $\Gamma_L(T)$ (FWHM) (blue points) are plotted in Fig. 6.2.5 and 6.2.6 in A_{1g} and $B_{1g} + B_{2g}$, respectively.

In A_{1g} symmetry the four phonon modes are located at 98.1 cm^{-1} [$A_{1g}(1)$], 531.1 cm^{-1} [$A_{1g}(2)$], 804.1 cm^{-1} [$A_{1g}(3)$], and 1005.4 cm^{-1} [$A_{1g}(4)$] at 0 T as shown in Fig. 5.2.3 (a). The linewidths of $A_{1g}(1)$ and (2) phonons in Fig. 6.2.5 (1) and (2), respectively, seem to be constant in the observed magnetic field range. The linewidths of the $A_{1g}(3)$ and (4) phonons in Fig. 6.2.5 (3) and (4), respectively, decrease with increasing the magnetic field. The energy of all RL phonons has a minimum at 1.58 T.

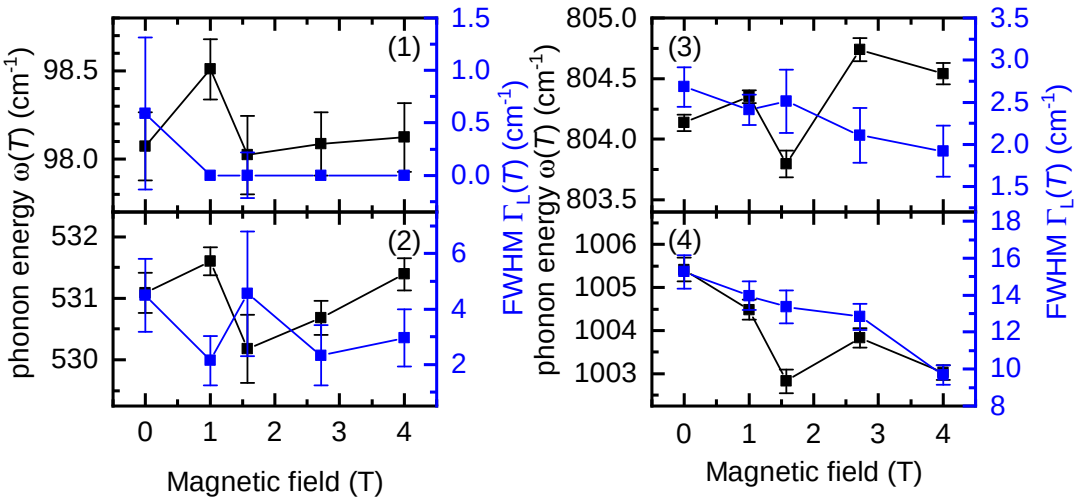

Figure 6.2.5.: Phonon energies ω (black) and Lorentzian widths Γ_L (blue) of TmB_4 in A_{1g} symmetry in the superfluid phase at 1.8 K for different magnetic fields ranging from $0-4$ T. The labeling of the panels corresponds to the labeling of the phonon peaks in Fig. 5.2.3 (a).

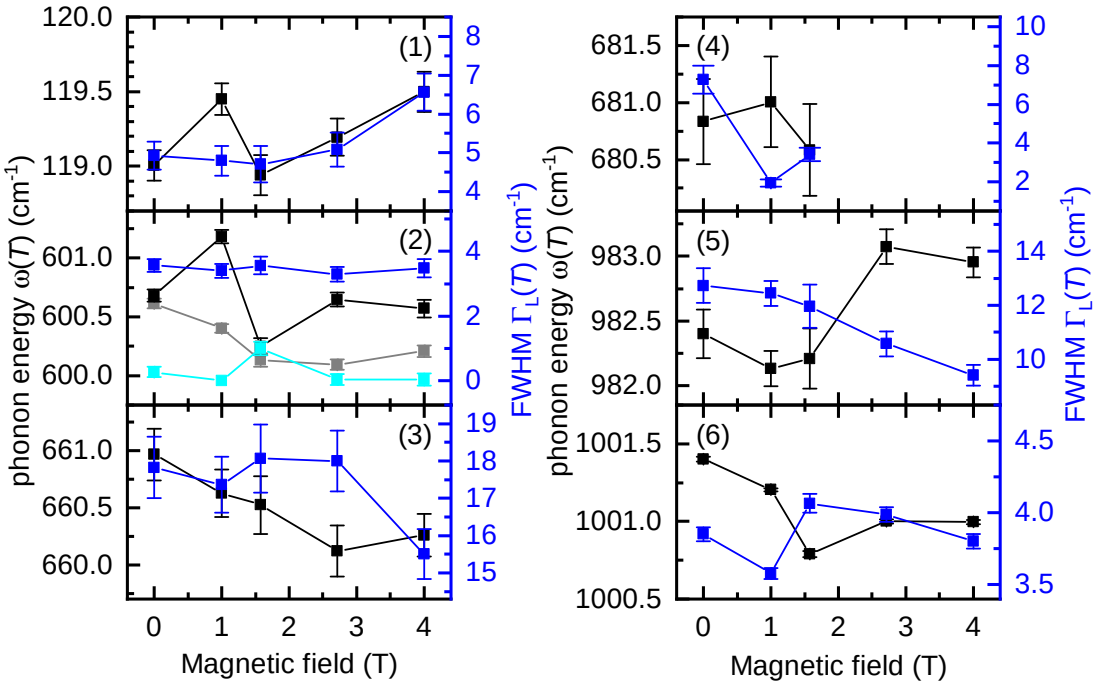

Figure 6.2.6.: Phonon energies ω (black) and Lorentzian widths Γ_L (blue) of TmB_4 in $B_{1g}+B_{2g}$ symmetry in the superfluid phase at 1.8 K for different magnetic fields ranging from $0-4$ T. The labeling of the panels corresponds to the labeling of the phonon peaks in Fig. 5.2.3 (b).

The same sequence of measurements as in RR configuration was also performed in RL polarization (see Fig. 6.2.4). The parameters of the $B_{1g}+B_{2g}$ phonons are plotted in Fig. 6.2.6. The RL(4) phonon (Fig. 6.2.6 (4)] could only be observed for magnetic fields up to 1.5 T and will be disregarded in the following. Although the data are noisy there are a few trends: (i) Minimal phonon energy is observed between 1 and 1.6 T similar as in A_{1g}

symmetry (RR) except for the RL(3) mode [Fig. 6.2.6 (3)]. (ii) RL(1) and RL(5) Phonons [Fig. 6.2.6 (1) and (5)] become harder, RL(3) and RL(6) phonons [Fig. 6.2.6 (3) and (6)] become softer with increasing field. (iii) The line widths are nearly constant (within the statistical noise) except for RL(1) and RL(5) phonons [Fig. 6.2.6 (1) and (5)] where they increase and, respectively, decrease significantly with increasing field. In the field range $1.3 - 1.6$ T the sample is in the plateau regime, which means that long range antiferromagnetic order intercalated with small stripes of ferromagnetic order as shown in Fig. 2.2.3 is established. Although the effects occurring upon crossing phase transition lines are small the overall picture of this analysis allows us to conclude that the various reorientations of the spin patterns have a correspondence in the lattice properties. Obviously the eigenvectors of the phonons determine strength and type of the interaction. However, it is too early for a quantitative analysis and certainly beyond the scope of this thesis. An important step are measurements at elevated temperature which would facilitate an analysis of the anharmonic decay and of the phonon-phonon coupling parameters as in the cases discussed in Section 6.1.

There are two possible reasons for the unexpectedly weak effects. First, all magnetic ordering phenomena are at $q \neq 0$ [24], and the coupling to Raman-active phonons at $q = 0$ is correspondingly weak. Second, all measurements were performed on polished surfaces, and it is not known to which depth the polishing procedure damages the surface. Although diamond polishing paste with a minimal grain size of $1\ \mu$m was used the influence may be substantial. In a further experiment cleaved samples should be used for cross-checking.

6.2.2. Magneto-caloric Effect

The coupling between magnetic order and lattice is a prerequisite of the strong magneto-caloric effect observed in TmB_4 [25]. The strongest magneto-caloric effect appears in TmB_4, if one rotates the sample in the magnetic field from an orientation with the basal plane of the crystal being parallel to being perpendicular with respect to the magnetic field at 20 K [25]. To search for related phonon anomalies, first measurements were performed with the direction of the magnetic field parallel to the c-axis of the sample. Afterwards, the sample was tilted, which results in an applied magnetic field perpendicular to the c-axis. With the sample surface parallel (c-axis perpendicular) to the field an extra mirror oriented at 45° w.r.t. the c-axis and the field axis in front of the surface is need to couple in and out the incident and scattered light. This mirror leads to a additional 15% loss of intensity in the stray light path.

The phonon peaks of the Raman spectra in Fig. 5.2.4 (a) and (b) were quantitatively analyzed with a Voigt function (c.f. Section 4.2.3). The obtained parameters, the peak energy $\omega(T)$ (black points) and the linewidth $\Gamma_{\mathrm{L}}(T)$ (FWHM) (blue points) of the phonon peak, are shown in Fig. 6.2.7 (a) and (b) for A_{1g} symmetry. Phonons at 120 cm^{-1} [Fig. 6.2.7 (c)] and at 601 cm^{-1} [Fig. 6.2.7 (d)] have B_{2g} and B_{1g} symmetry, respectively. Their dependence on the field orientation are shown on the respective panels. Neither the A_{1g} nor the B_{1g} nor

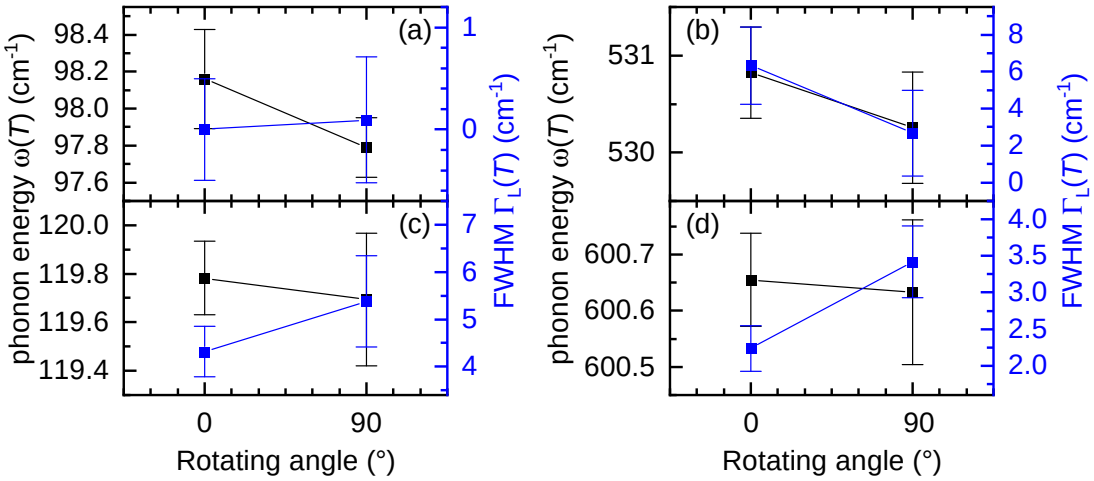

Figure 6.2.7.: Phonon energies ω (black) and Lorentzian widths Γ_L (blue) of TmB_4 in (a) and (b) A_{1g}, (c) B_{2g}, and (d) B_{1g} symmetry in an applied magnetic field of $B = 4.5$ T and a temperature of 20 K parallel (0°) and perpendicular (90°) to the c-axis of the sample.

the B_{2g} phonons depend significantly on the field orientation.

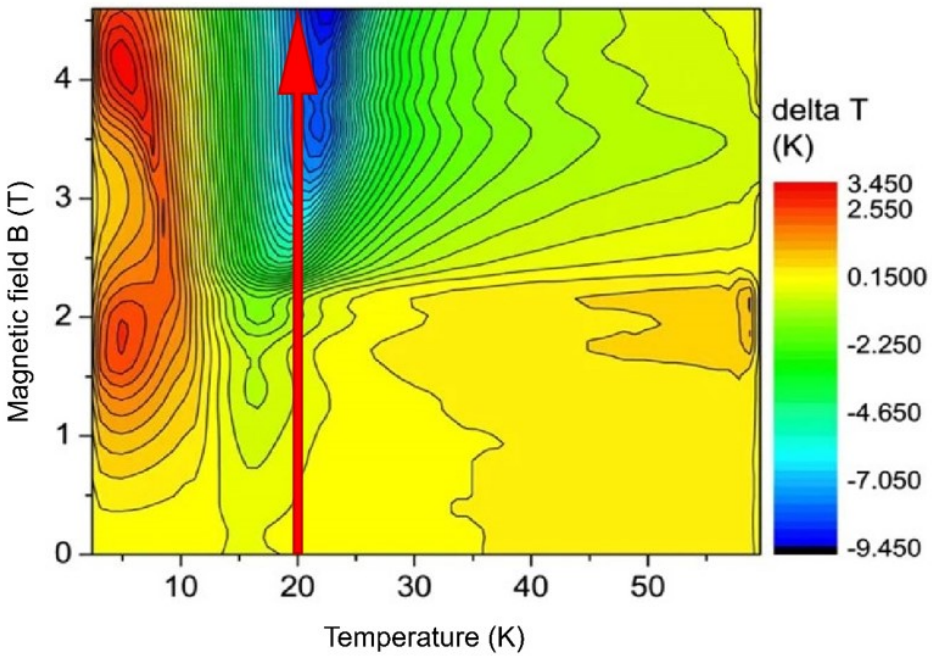

Figure 6.2.8.: Magneto-caloric effect phase diagram of TmB_4 as a function of the temperature and the magnetic field. The red arrow indicates the changed parameter in the measurement. Here, the strength of the magnetic field was changed and the temperature was held constant at $T = 20$ K [25].

To see whether the phonon modes in the A_{1g}, the B_{1g}, and the B_{2g} symmetry couple to the magneto-caloric effect, measurements were performed in the range of the highest change in temperature, which occurs at 20 K and 4.5 T. Therefore, first measurements were

performed at the constant temperature 20 K and the magnetic field was ramped up in the range $0.5 - 4.5$ T as indicated with a red arrow in Fig. 6.2.8.

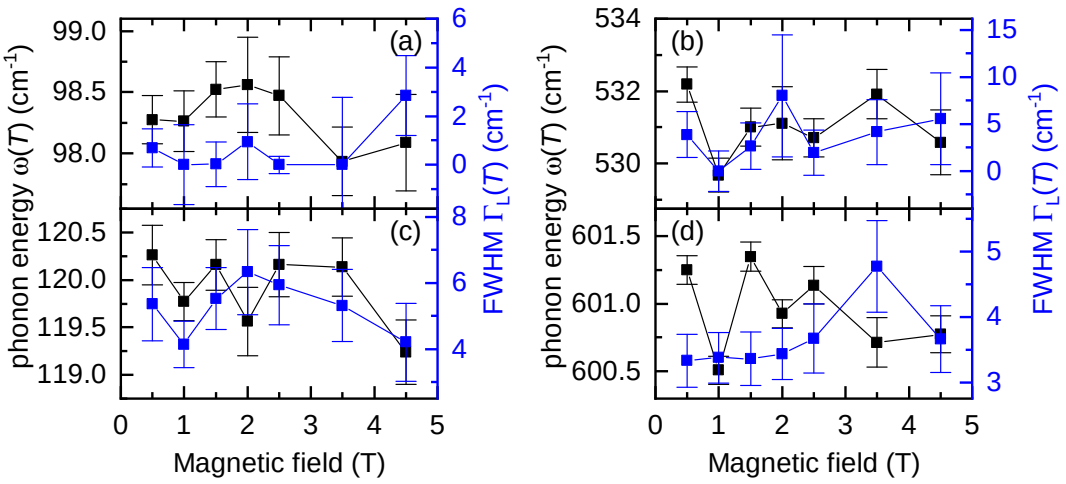

Figure 6.2.9.: Phonon energies ω (black) and Lorentzian widths Γ_L (blue) of TmB_4 in (a) and (b) A_{1g}, (c) B_{2g}, and (d) B_{1g} symmetry at 20 K for magnetic fields between $0.5 - 4.5$ T.

Fig. 6.2.9 illustrates the evolution of both the phonon energy ω (black points) and the phonon linewidth Γ_L (blue points) as a function of temperature of the phonon spectra plotted in Fig. 5.2.2. The A_{1g} phonons are located at 98.3 cm^{-1} [Fig. 6.2.9 (a)] and 532.2 cm^{-1} [Fig. 6.2.9 (b)] with an applied magnetic field $B = 0.5$ T. The B_{2g} phonon has an energy of 120.3 cm^{-1} [Fig. 6.2.9 (c)] and the B_{1g} phonon has an energy of 601.2 cm^{-1} [Fig. 6.2.9 (d)] with an applied magnetic field $B = 0.5$ T. Both the phonon energies and the linewidths of all phonons show no statistically significant magnetic field dependence.

The following measurements investigate the coupling of the phonons to the magneto-caloric effect at a constant magnetic field $B = 4.5$ T and varying temperatures ranging from $15 - 25$ K as indicated with a red arrow in Fig. 6.2.10. The corresponding Raman spectra of these measurements are pictured in Fig. 5.2.5.

Fig. 6.2.11 shows both the change in the phonon energy ω (black points) and the phonon linewidth Γ_L (blue points) as a function of temperature of the phonon peaks pictured in Fig. 5.2.5. The phonons in A_{1g} are located at 97.7 cm^{-1} [Fig. 6.2.11 (a)] and 530.2 cm^{-1} [Fig. 6.2.11 (b)] at the temperature $T = 15$ K. The energy of the phonon in the B_{2g} symmetry is 119.5 cm^{-1} [Fig. 6.2.11 (c)] and the energy of the phonon in B_{1g} symmetry is 600.5 cm^{-1} [Fig. 6.2.11 (d)] at the temperature $T = 15$ K. The phonon energy ω of the phonons in all observed symmetries, A_{1g}, B_{1g}, and B_{2g}, is almost constant.

No significant changes of the phonon linewidth Γ_L were observed either. There may be a small tendency of the phonon energy $\omega(B)$ to increase with the field. This leads to the conclusion, that the magneto-elastic coupling is very weak if observable at all. Yet, also here one has to consider possible effects from the polished surface. In addition, the magneto-caloric effect is transient in nature and may not be observable in an experiment

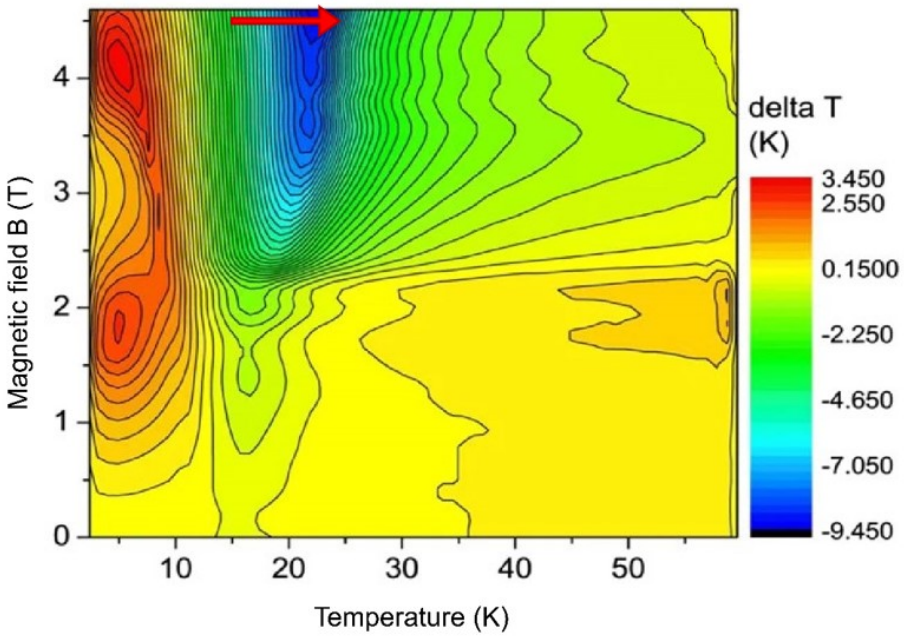

Figure 6.2.10.: Magneto-caloric effect phase diagram of TmB_4 as a function of the temperature and the magnetic field. The red arrow indicates the changed parameter in the measurement. Here, the temperature was changed and the magnetic field was held constant at $B = 1$ T [25].

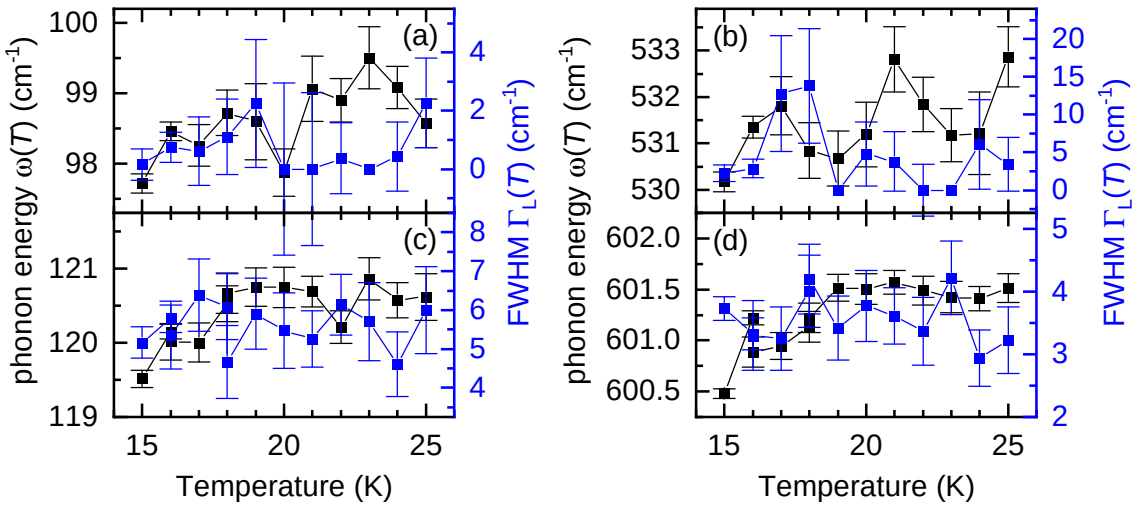

Figure 6.2.11.: Phonon energies ω (black) and Lorentzian widths Γ_L (blue) of TmB_4 in (a) and (b) A_{1g}, (c) B_{2g}, and (d) B_{1g} symmetry in an applied magnetic field $B = 4.5$ T at different temperatures.

which requires at least two minutes acquisition time. On the other hand, the stability of these energies and widths makes us confident that the changes observed across the phase boundaries found in Figs. 6.2.2, 6.2.3, 6.2.5, and 6.2.6 are significant.

7. Summary

In this thesis, various magnetic materials having Archimedean lattice structures were studied by Raman spectroscopy as a function of temperature and light polarization. TmB_4 was additionally studied in variable applied magnetic fields.

In the Kagome ferromagnet Fe_3Sn_2 all phonon lines except for one were identified. Under the assumption that the optical phonons decay symmetrically into two lines at $\omega_0/2$ and $\pm\mathbf{k}$ the dimensionless phonon-phonon coupling parameter $\lambda_{\text{ph-ph},i}$ could be extracted and was found to be $\lambda_{\text{ph-ph},i}$ in the range 0.1 to 1.1. A clear anomaly was observed in the A_{1g} phonon having the lowest energy [$A_{1g}(1)$] where $\lambda_{\text{ph-ph},1}$ increases from 0.015 to 0.2 below the reorientation temperature of the Fe spins. This means, that $\lambda_{\text{ph-ph},1}$ is switched on, as soon as the Fe spins point perpendicular to the motion of the Sn vibrations. To check the contribution of the thermal expansion of the lattice to the phonon energy $\omega(T)$, the Grüneisen parameter γ_i for all phonon modes were extracted. γ_i ranges between 0.23 to 0.94. In $A_{1g}(1)$ the first order contribution $\Delta_1^{(1)}(T)$ dominates. γ_1 stays almost constant although the phonon-phonon coupling parameter $\lambda_{\text{ph-ph},(1)}$ changes by more than a factor of 10. Since Fe_3Sn_2 has a relatively high Curie temperature ($T_C = 670$ K), strong changes in the electronic properties in the range $4.2 - 300$ K are not to be expected. Yet, a substantial variation with temperature at low energies was found in the E_g continuum. On the one hand this variation is reminiscent of the strong temperature dependence of the resistivity $\rho(T)$. On the other hand, the low energy peak may originate from magnetic fluctuations in a geometrically frustrated system [17] or from a band gap induced by the spin reorientation as suggested by optical measurements [104]. However, the rather different energies in the two experiments argue against this possibility [17].

In the Weyl semimetal $Co_3Sn_2S_2$ two Raman active phonon modes with A_{1g} and E_g symmetry are observed. The E_g phonon line is symmetric and no changes in phonon energy and linewidth can be found. The phonon-phonon coupling parameter $\lambda_{\text{ph-ph},i}$ and the Grüneisen parametera γ_i were extracted for both phonon lines. Similar to the A_{1g} phonon modes in Fe_3Sn_2, a significant change in the coupling parameter of the A_{1g} phonon was observed with values for $\lambda_{\text{ph-ph}}(A_{1g})$ of 0.12 and 0.85 above or below the magnetic transition temperature, respectively. At T_C $Co_3Sn_2S_2$ transitions from a paramagnetic material to a ferromagnetic material with an out-of-plane orientation of the Co spins. Since the Co spins sitting on the Kagome layer order ferromagnetically, they couple to the lattice, leading to the change of the temperature dependence of the phonon linewidth. Although the phonon-phonon coupling parameters $\lambda_{\text{ph-ph},i}$ in A_{1g} symmetry change by a factor of ≈ 6

across T_C, the Grüneisen parameters γ_i do not change significantly. This indicates that the energy of the A_{1g} phonon mode is dominated by the first order contribution $\Delta_i^{(1)}(T)$, which originates from the thermal lattice expansion. The A_{1g} phonon line is asymmetric and well described by a Fano function suggesting its strong coupling to the electronic continuum. The Fano asymmetry parameter $1/|q|$ exhibits a non-monotonic temperature dependence. Upon heating, the asymmetry factor increases towards T_C and then decreases slowly again. The electronic continua in both A_{1g} and E_g symmetry show a redistribution of the spectral weight below T_C. The redistribution of spectra weight in the ordered phase argues more for itinerant SDW magnetism. Features typical for two-magnon excitations could not be observed.

Similar to $Co_3Sn_2S_2$, CsV_3Sb_5 shows a spectral weight redistribution in both the A_{1g} and E_g symmetry below the charge-density-wave (CDW) critical temperature ($T_{CDW} = 94$ K). This indicates, that a gap opens at approximately 1600 cm^{-1} in the A_{1g} and 1550 cm^{-1} in the E_g symmetry. The CDW gap is expected to appear at the M points. Although only the E_g symmetry selectively maps the M points, the gap like features can be found in both symmetries. Suggesting an influence of the second-order Raman vertex several new phonons appear below T_{CDW} in addition to the A_{1g} and E_g mode present at all temperatures. These new phonons are associated with the lattice distortion due to the CDW transition. No sign of a hysteresis was found in the energy of the A_{1g} phonon at T_C. Therefore, an argument can be made for either a second-order or a weak first-order phase transition. Two amplitude modes at 104.4 cm^{-1} in A_{1g} and 208.3 cm^{-1} in E_g symmetry were observed at 12.6 K. The amplitude mode in A_{1g} symmetry couples strongly to the continuum and hence, shows an asymmetric Fano line shape. Theoretical calculations are needed to further investigate this new interesting Kagome-layer material.

The rich temperature-field phase diagram of the tetraboride TmB_4 [24] was studied in a magnetic field of up to 4.5 T and for two orientations of the sample with respect to the field. To scan both vertically and horizontally through the phase diagram either the temperature was held constant and the externally applied magnetic field was varied or vice versa. Only the energy of the phonons change, when the material enters either the plateau regime or the intermediate phase. These phases show both a long range antiferromagnetic order. While the Plateau regime exhibits short range ferromagnetic order, the ordering in the Intermediate phase is intercalated by small stripes of ferromagnetic order. In the range of the strongest magneto-caloric effect (MCE) measurements at $B = 4.5$ T and $T = 20$ K [25] were performed. Either the temperature or the externally applied magnetic field was held constant and the other parameter was varied. The phonons were not affected by neither changes in temperature nor the magnetic field. Since the strongest rotating magnetocaloric effect is detected, when the sample is rotated by either $90°$ or $270°$, measurements were performed before and after the sample was rotated by $90°$ in an externally applied magnetic field. The Raman spectra did neither show significant changes in the phonon energy $\omega(T)$ nor linewidth $\Gamma_L(T)$. The transient nature of the magneto-caloric effect may be a seri-

ous challenge. In future studies cleaved samples should be explored to exclude a possible negative influence of the polishing procedure..

A. Thermal Lattice Expansion

A.1. Thermal Expansion of Fe_3Sn_2

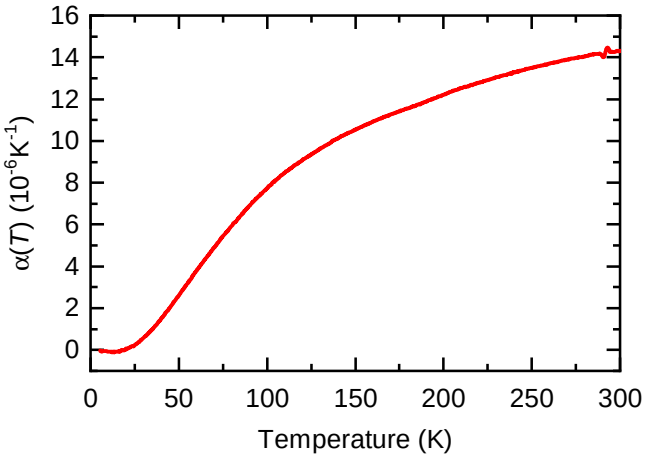

Figure A.1.1.: Thermal expansion coefficient $\alpha(T)$ of Fe_3Sn_2

The phonon energy $\omega(T)$ can be described by Eq. 6.3. The first order contribution $\Delta_i^{(1)}(T)$ consists of an integral of the thermal expansion coefficient $\alpha(T)$ of the sample. The thermal expansion coefficient data of Fe_3Sn_2 is provided by Dr. Christoph Meingast's group from Karlsruhe Institute of Technology, which is shown in Fig. A.1.1. The integral of the data was fitted with a third order polynomial and then inserted in Eq. 6.3.

A.2. Volume Change of $Co_3Sn_2S_2$

The phonon energy $\omega(T)$ can be described by Eq. 6.3. The first order contribution $\Delta_i^{(1)}(T)$ consists of an integral of the thermal lattice expansion $\alpha(T)$ of the sample. The integrated thermal expansion describes the volume of the sample. Typical volume values of $Co_3S_2S_2$ [124] are pictured in Fig. A.2.1 as black dots. The data were fitted with a polynomial00 function of fourth order (blue line) and then inserted in Eq. 6.3.

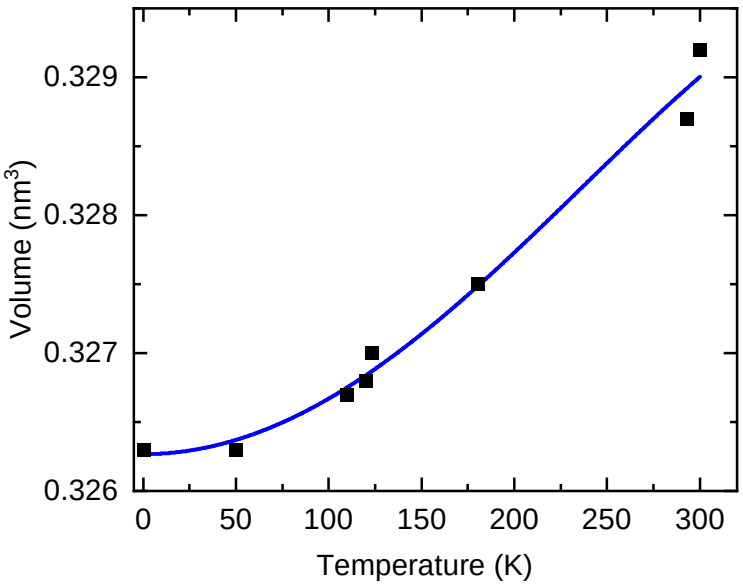

Figure A.2.1.: Volume of $Co_3S_2S_2$ as a function of temperature

B. Symmetry Analysis

B.1. CsV_3Sb_5

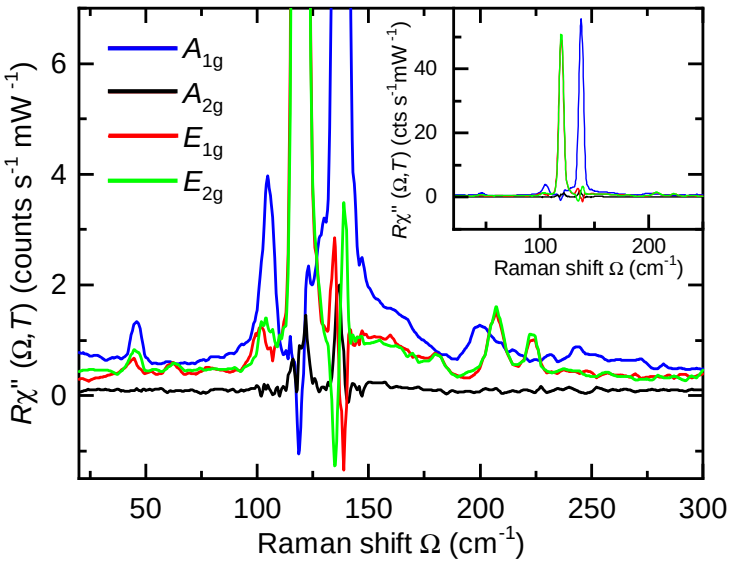

Figure B.1.1.: Symmetry analysis of CsV_3Sb_5 at 20 K for the four main symmetries as indicated. The spectra in E_{1g} and E_{2g} show the same seven peaks and therefore, they can't be distinguished. The A_{1g} spectrum has four peaks, while the A_{2g} symmetry contribution can be neglected.

Fig. B.1.1 shows Raman spectra of the four main symmetries of the Kagome lattice material CsV_3Sb_5 at 20 K. The A_{1g} symmetry exhibits four peaks at around 46 cm^{-1}, 105 cm^{-1}, 137 cm^{-1} and 200 cm^{-1}, respectively. The spectrum in A_{2g} symmetry has only small intensity compared to the other symmetries. Therefore, it is negligible and won't be considered in this thesis.

In both E_{1g} and E_{2g} symmetry, seven peaks appear at around 45 cm^{-1}, 62 cm^{-1}, 103 cm^{-1}, 119 cm^{-1}, 180 cm^{-1}, 207 cm^{-1} and 223 cm^{-1}, respectively. The Raman spectra in E_{1g} and E_{2g} symmetry have the same shape and therefore, it isn't possible for the programm to distinguish between these two different symmetries.

B.2. TmB_4

The symmetry analysis for energies below 650 cm^{-1} of the tetraboride TmB_4 at 100 K consists of the four main symmetries in this material. The A_{1g} symmetry consists of one peak

located at cm^{-1} superimposed onto a continuum. The spectrum in A_{2g} symmetry is low in intensity and shows neither a peak nor any other visible contribution. Therefore, the A_{2g} symmetry of TmB_4 will be neglected.

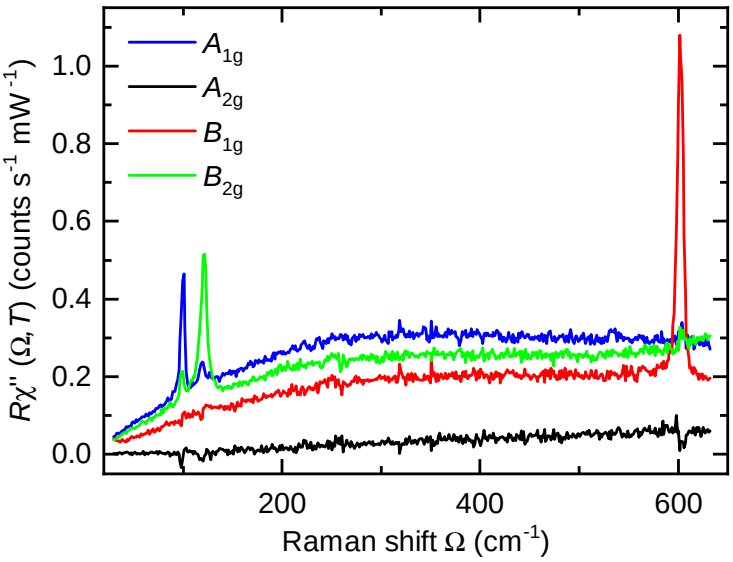

Figure B.2.1.: Symmetry analysis of TmB_4 at 20 K for the four main symmetries as indicated. The A_{2g} symmetry contribution can be neglected. The A_{1g}, B_{1g} and B_{2g} symmetries all show one peak superimposed onto a continuum, respectively.

The B_{1g} symmetry exhibits a sharp peak at cm^{-1}. Its intensity is comparable to the one in A_{1g} and is also superimposed onto a continuum. Small leakages can be found in both A_{1g} and B_{1g} symmetries of both phonons, respectively. A strong peak at the energy cm^{-1} in B_{2g} symmetry is superimposed onto a continuum, as well as the other two peaks in the energy range pictured. Since the symmetry analysis of TmB_4 was only performed in the low energy range, the B_{1g} and the B_{2g} symmetries will be labeled with $B_{1g} + B_{2g}$.

C. Fano Fits of CsV_3Sb_5

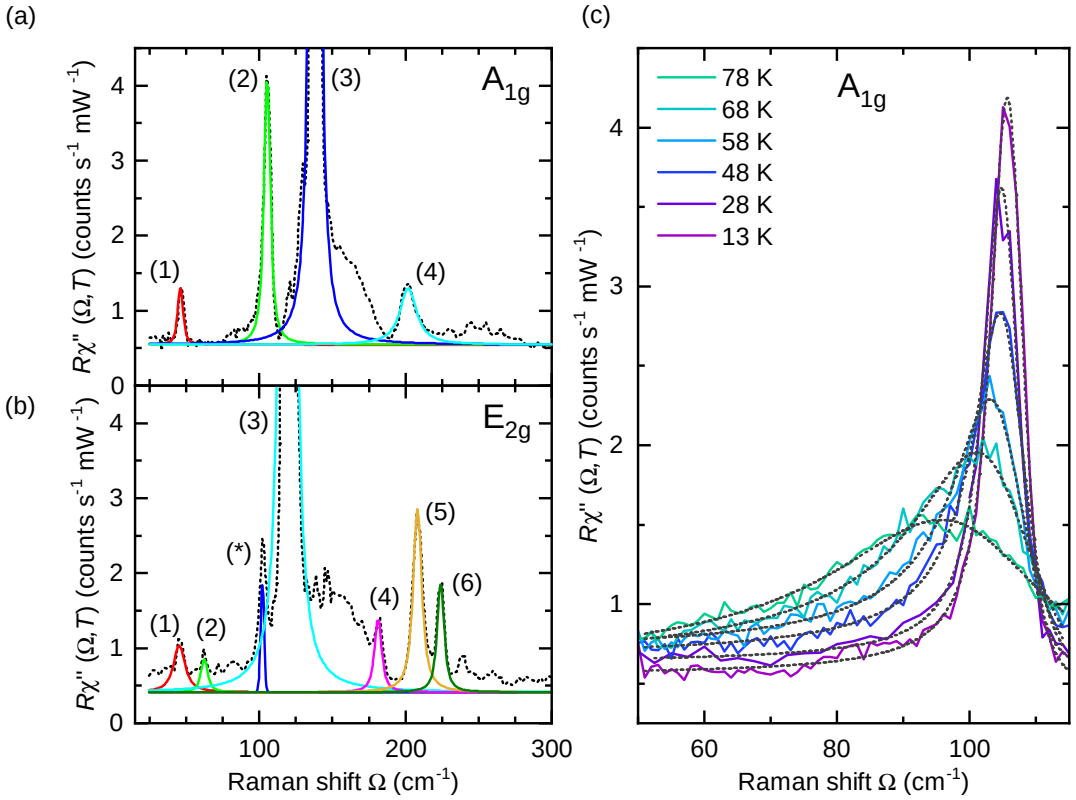

Figure C.0.1.: Fitting results of the Raman active phonon modes and the amplitude modes in A_{1g} and E_{2g} symmetry. Panel (a) and (b) present the Voigt fits (coloured lines) of the different peaks in A_{1g} and E_{2g} symmetry, respectively. Peak (2) and peak (5) in panel (a) and (b), respectively, were fitted with a Fano function convoluted with a Gaussian distribution. The dashed lines describe the actual Raman spectra at 12.6 K. Panel (c) shows the evolution of the amplitude mode in A_{1g} (coloured lines), which were fitted with a Fano function convoluted with a Gaussian distribution, at temperatures as indicated.

Fig. C.0.1 presents the fitting results of both the Raman active phonon modes and the amplitude modes in (a) A_{1g} and (b) E_{2g} symmetry at 12.6 K. The phonon modes (1), (3), and (4) in A_{1g} and the phonon modes (1)-(4), (*), and (6) in E_{2g} were fitted using a Voigt function (c.f. Eq. 4.1). The amplitude modes (2) in A_{1g} and (5) in E_{2g} are described by a Fano fit-function, which is convoluted with a Gaussian distribution, due to its asymmetric shape. The temperature-dependent evolution of the amplitude mode in A_{1g} and the corresponding Fano-fits are presented in Fig. C.0.1 (c). The asymmetry of the peak decreases for lower temperatures.

Bibliography

[1] D. J. J. Farnell, O. Götze, J. Richter, R. F. Bishop, and P. H. Y. Li, *Quantum $s = \frac{1}{2}$ antiferromagnets on Archimedean lattices: The route from semiclassical magnetic order to nonmagnetic quantum states*, Physical Review B **89**, 184407 (2014).

[2] U. Yu, *Ising antiferromagnet on the Archimedean lattices*, Physical Review E **91**, 062121 (2015).

[3] J. Richter, J. Schulenburg, and A. Honecker, in *Quantum Magnetism*, Lecture Notes in Physics, Vol. 645, edited by U. Schollwöck, J. Richter, D. J. J. Farnell, and R. F. Bishop (Springer Berlin Heidelberg, Berlin, Heidelberg, 2004) pp. 85–153.

[4] Y.-Z. Zheng, Z. Zheng, and X.-M. Chen, *A symbol approach for classification of molecule-based magnetic materials exemplified by coordination polymers of metal carboxylates*, Coordination Chemistry Reviews **258-259**, 1 (2014).

[5] J. V. Field, *Rediscovering the Archimedean Polyhedra: Piero della Francesca, Luca Pacioli, Leonardo da Vinci, Albrecht Dürer, Daniele Barbaro, and Johannes Kepler*, Archive for History of Exact Sciences **50**, 241 (1997).

[6] W. Osterhage, *Johannes Kepler* (Springer International Publishing, Cham, 2020).

[7] J. Vannimenus and G. Toulouse, *Theory of the frustration effect. II. Ising spins on a square lattice*, Journal of Physics C: Solid State Physics **10**, L537 (1977).

[8] G. Toulouse, in *Modern Trends in the Theory of Condensed Matter*, Lecture Notes in Physics, Vol. 115, edited by A. Pękalski and J. A. Przystawa (Springer Berlin Heidelberg, Berlin, Heidelberg, 1980) pp. 195–203.

[9] G. H. Wannier, *Antiferromagnetism. The Triangular Ising Net*, Physical Review **79**, 357 (1950).

[10] P. W. Anderson, *Localisation theory and the Cu-Mn problem: Spin glasses*, Materials Research Bulletin **5**, 549 (1970).

[11] H.-M. Guo and M. Franz, *Topological insulator on the kagome lattice*, Physical Review B **80**, 113102 (2009).

[12] W.-S. Wang, Z.-Z. Li, Y.-Y. Xiang, and Q.-H. Wang, *Competing electronic orders on kagome lattices at van Hove filling*, Physical Review B **87**, 115135 (2013).

[13] W.-H. Ko, P. A. Lee, and X.-G. Wen, *Doped kagome system as exotic superconductor*, Physical Review B **79**, 214502 (2009).

[14] M. Kang, L. Ye, S. Fang, J.-S. You, A. Levitan, M. Han, J. I. Facio, C. Jozwiak, A. Bostwick, E. Rotenberg, M. K. Chan, R. D. McDonald, D. Graf, K. Kaznatcheev, E. Vescovo, D. C. Bell, E. Kaxiras, J. van den Brink, M. Richter, M. P. Ghimire, J. G. Checkelsky, and R. Comin, *Dirac fermions and flat bands in the ideal kagome metal FeSn*, Nature Materials **19**, 163 (2019).

[15] L. Ye, M. Kang, J. Liu, F. von Cube, C. R. Wicker, T. Suzuki, C. Jozwiak, A. Bostwick, E. Rotenberg, D. C. Bell, L. Fu, R. Comin, and J. G. Checkelsky, *Massive Dirac fermions in a ferromagnetic kagome metal*, Nature **555**, 638 (2018).

[16] N. Morali, R. Batabyal, P. K. Nag, E. Liu, Q. Xu, Y. Sun, B. Yan, C. Felser, N. Avraham, and H. Beidenkopf, *Fermi-arc diversity on surface terminations of the magnetic Weyl semimetal $Co_3Sn_2S_2$*, Science **365**, 1286 (2019).

[17] G. He, L. Peis, R. Stumberger, L. Prodan, V. Tsurkan, N. Unglert, L. Chioncel, I. Kézsmárki, and R. Hackl, *Phonon anomalies associated with spin reorientation in the Kagome ferromagnet Fe_3Sn_2*, arXiv:2107.14623 (2021), arXiv:2107.14623 [cond-mat.mtrl-sci] .

[18] T. Kida, L. A. Fenner, A. A. Dee, I. Terasaki, M. Hagiwara, and A. S. Wills, *The giant anomalous Hall effect in the ferromagnet Fe_3Sn_2 - a frustrated kagome metal*, Journal of Physics: Condensed Matter **23**, 112205 (2011).

[19] Y. Okamura, S. Minami, Y. Kato, Y. Fujishiro, Y. Kaneko, J. Ikeda, J. Muramoto, R. Kaneko, K. Ueda, V. Kocsis, N. Kanazawa, Y. Taguchi, T. Koretsune, K. Fujiwara, A. Tsukazaki, R. Arita, Y. Tokura, and Y. Takahashi, *Giant magneto-optical responses in magnetic Weyl semimetal $Co_3Sn_2S_2$*, Nature Communications **11**, 4619 (2020).

[20] E. Liu, Y. Sun, N. Kumar, L. Muechler, A. Sun, L. Jiao, S.-Y. Yang, D. Liu, A. Liang, Q. Xu, J. Kroder, V. Süss, H. Borrmann, C. Shekhar, Z. Wang, C. Xi, W. Wang, W. Schnelle, S. Wirth, Y. Chen, S. T. B. Goennenwein, and C. Felser, *Giant anomalous Hall effect in a ferromagnetic Kagome-lattice semimetal*, Nature Physics **14**, 1125 (2018).

[21] B. R. Ortiz, L. C. Gomes, J. R. Morey, M. Winiarski, M. Bordelon, J. S. Mangum, I. W. H. Oswald, J. A. Rodriguez-Rivera, J. R. Neilson, S. D. Wilson, E. Ertekin, T. M. McQueen, and E. S. Toberer, *New kagome prototype materials: discovery of KV_3Sb_5, RbV_3Sb_5, and CsV_3Sb_5*, Physical Review Materials **3**, 094407 (2019).

[22] B. R. Ortiz, S. M. Teicher, Y. Hu, J. L. Zuo, P. M. Sarte, E. C. Schueller, A. M. Abeykoon, M. J. Krogstad, S. Rosenkranz, R. Osborn, R. Seshadri, L. Balents, J. He, and S. D. Wilson, CsV_3Sb_5*: A* $\mathbb{Z}_2$ *Topological Kagome Metal with a Superconducting Ground State*, Physical Review Letters **125**, 247002 (2020).

[23] N. Pakhira, J. Krishna, S. Nandy, T. Maitra, and A. Taraphder, *Electronic structure of metallic tetra-boride* TmB_4*: An LDA+DMFT study*, (2018), arXiv:1807.05388 [cond-mat.str-el] .

[24] K. Siemensmeyer, E. Wulf, H.-J. Mikeska, K. Flachbart, S. Gabáni, S. Matáš, P. Priputen, A. Efdokimova, and N. Shitsevalova, *Fractional Magnetization Plateaus and Magnetic Order in the Shastry-Sutherland Magnet* TmB_4, Physical Review Letters **101**, 177201 (2008).

[25] M. Orendáč, S. Gabáni, E. Gažo, G. Pristáš, N. Shitsevalova, K. Siemensmeyer, and K. Flachbart, *Rotating magnetocaloric effect and unusual magnetic features in metallic strongly anisotropic geometrically frustrated* TmB_4, Scientific Reports **8**, 10933 (2018).

[26] L. Peis, *Origin of the nematic fluctuations in iron-based superconductors*, Master's thesis, Technische Universtität München (2019).

[27] H.-M. Eiter, *Carrier and Lattice Dynamics in Systems with Charge and Spin Order*, Dissertation, Technische Universität München (2014).

[28] S. V. Isakov, S. Wessel, R. G. Melko, K. Sengupta, and Y. B. Kim, *Hard-Core Bosons on the Kagome Lattice: Valence-Bond Solids and Their Quantum Melting*, Physical Review Letters **97**, 147202 (2006).

[29] J. Wen, A. Rüegg, C.-C. J. Wang, and G. A. Fiete, *Interaction-driven topological insulators on the kagome and the decorated honeycomb lattices*, Physical Review B **82**, 075125 (2010).

[30] Q. Xu, E. Liu, W. Shi, L. Muechler, J. Gayles, C. Felser, and Y. Sun, *Topological surface Fermi arcs in the magnetic Weyl semimetal* $Co_3Sn_2S_2$, Physical Review B **97**, 235416 (2018).

[31] S. N. Guin, P. Vir, Y. Zhang, N. Kumar, S. J. Watzman, C. Fu, E. Liu, K. Manna, W. Schnelle, J. Gooth, C. Shekhar, Y. Sun, and C. Felser, *Zero-Field Nernst Effect in a Ferromagnetic Kagome-Lattice Weyl-Semimetal* $Co_3Sn_2S_2$, Advanced Materials **31**, 1806622 (2019).

[32] H. Zhao, H. Li, B. R. Ortiz, S. M. L. Teicher, T. Park, M. Ye, Z. Wang, L. Balents, S. D. Wilson, and I. Zeljkovic, *Cascade of correlated electron states in the kagome superconductor* CsV_3Sb_5, Nature **599**, 216–221 (2021).

[33] M. L. Kiesel and R. Thomale, *Sublattice interference in the kagome Hubbard model*, Physical Review B **86**, 121105 (2012).

[34] M. Kang, S. Fang, L. Ye, H. C. Po, J. Denlinger, C. Jozwiak, A. Bostwick, E. Rotenberg, E. Kaxiras, J. G. Checkelsky, and R. Comin, *Topological flat bands in frustrated kagome lattice CoSn*, Nature Communications **11**, 4004 (2020).

[35] H. Ibach and H. Lüth, *Elektronische Bänder in Festkörpern*, in *Festkörperphysik: Einführung in die Grundlagen* (Springer Berlin Heidelberg, Berlin, Heidelberg, 2009) pp. 159–187.

[36] G. Li, A. Luican, J. M. B. L. dos Santos, A. H. C. Neto, A. Reina, J. Kong, and E. Y. Andrei, *Observation of Van Hove singularities in twisted graphene layers*, Nature Physics **6**, 109 (2009).

[37] Y. Fu, N. Zhao, Z. Chen, Q. Yin, Z. Tu, C. Gong, C. Xi, X. Zhu, Y. Sun, K. Liu, and H. Lei, *Quantum transport evidence of topological band structures of kagome superconductor CsV3Sb5*, Physical Review Lett. 127, 207002 (2021) (2021), 10.1103/PhysRevLett.127.207002, version 2, arXiv:2104.08193 [cond-mat.supr-con] .

[38] D. F. Liu, A. J. Liang, E. K. Liu, Q. N. Xu, Y. W. Li, C. Chen, D. Pei, W. J. Shi, S. K. Mo, P. Dudin, T. Kim, C. Cacho, G. Li, Y. Sun, L. X. Yang, Z. K. Liu, S. S. P. Parkin, C. Felser, and Y. L. Chen, *Magnetic Weyl semimetal phase in a Kagomé crystal*, Science **365**, 1282 (2019).

[39] J.-Z. Ma, Q.-S. Wu, M. Song, S.-N. Zhang, E. B. Guedes, S. A. Ekahana, M. Krivenkov, M. Y. Yao, S.-Y. Gao, W.-H. Fan, T. Qian, H. Ding, N. C. Plumb, M. Radovic, J. H. Dil, Y.-M. Xiong, K. Manna, C. Felser, O. V. Yazyev, and M. Shi, *Observation of a singular Weyl point surrounded by charged nodal walls in PtGa*, Nature Communications **12**, 3994 (2021).

[40] H. Weng, C. Fang, Z. Fang, B. A. Bernevig, and X. Dai, *Weyl Semimetal Phase in Noncentrosymmetric Transition-Metal Monophosphides*, Physical Review X **5**, 011029 (2015).

[41] Q. Wang, Y. Xu, R. Lou, Z. Liu, M. Li, Y. Huang, D. Shen, H. Weng, S. Wang, and H. Lei, *Large intrinsic anomalous Hall effect in half-metallic ferromagnet $Co_3Sn_2S_2$ with magnetic Weyl fermions*, Nature Communications **9**, 3681 (2018).

[42] M. Yao, H. Lee, N. Xu, Y. Wang, J. Ma, O. V. Yazyev, Y. Xiong, M. Shi, G. Aeppli, and Y. Soh, *Switchable Weyl nodes in topological Kagome ferromagnet Fe_3Sn_2*, (2018), arXiv:1810.01514 [cond-mat.str-el] .

[43] J.-X. Yin, S. S. Zhang, G. Chang, Q. Wang, S. S. Tsirkin, Z. Guguchia, B. Lian, H. Zhou, K. Jiang, I. Belopolski, N. Shumiya, D. Multer, M. Litskevich, T. A. Cochran, H. Lin, Z. Wang, T. Neupert, S. Jia, H. Lei, and M. Z.

HASAN, *Negative flat band magnetism in a spin–orbit-coupled correlated kagome magnet*, Nature Physics **15**, 443 (2019).

[44] Y. XU, J. ZHAO, C. YI, Q. WANG, Q. YIN, Y. WANG, X. HU, L. WANG, E. LIU, G. XU, L. LU, A. A. SOLUYANOV, H. LEI, Y. SHI, J. LUO, AND Z.-G. CHEN, *Electronic correlations and flattened band in magnetic Weyl semimetal candidate $Co_3Sn_2S_2$*, Nature Communications **11**, 3985 (2020).

[45] Z. LIN, J.-H. CHOI, Q. ZHANG, W. QIN, S. YI, P. WANG, L. LI, Y. WANG, H. ZHANG, Z. SUN, L. WEI, S. ZHANG, T. GUO, Q. LU, J.-H. CHO, C. ZENG, AND Z. ZHANG, *Flatbands and Emergent Ferromagnetic Ordering in Fe_3Sn_2 Kagome Lattices*, Physical Review Letters **121**, 096401 (2018).

[46] Y. HU, S. M. L. TEICHER, B. R. ORTIZ, Y. LUO, S. PENG, L. HUAI, J. Z. MA, N. C. PLUMB, S. D. WILSON, J. F. HE, AND M. SHI, *Charge-order-assisted topological surface states and flat bands in the kagome superconductor CsV_3Sb_5*, (2021), arXiv:2104.12725 [cond-mat.supr-con] .

[47] Z. LIANG, X. HOU, F. ZHANG, W. MA, P. WU, Z. ZHANG, F. YU, J.-J. YING, K. JIANG, L. SHAN, Z. WANG, AND X.-H. CHEN, *Three-Dimensional Charge Density Wave and Surface-Dependent Vortex-Core States in a Kagome Superconductor CsV_3Sb_5*, Physical Review X **11**, 031026 (2021).

[48] F.-H. WANG, P. KRÜGER, AND J. POLLMANN, *Surface electronic structure of GaN(0001)-(1×1): comparison between theory and experiment*, Surface Science **499**, 193 (2002).

[49] H. RAZA, *Theoretical study of isolated dangling bonds, dangling bond wires, and dangling bond clusters on a $H:Si(001)-(2\times1)$ surface*, Physical Review B **76**, 045308 (2007).

[50] Z. ZHANG, Y. WANG, K. WATANABE, T. TANIGUCHI, K. UENO, E. TUTUC, AND B. J. LEROY, *Flat bands in twisted bilayer transition metal dichalcogenides*, Nature Physics **16**, 1093 (2020).

[51] M. I. B. UTAMA, R. J. KOCH, K. LEE, N. LECONTE, H. LI, S. ZHAO, L. JIANG, J. ZHU, K. WATANABE, T. TANIGUCHI, P. D. ASHBY, A. WEBER-BARGIONI, A. ZETTL, C. JOZWIAK, J. JUNG, E. ROTENBERG, A. BOSTWICK, AND F. WANG, *Visualization of the flat electronic band in twisted bilayer graphene near the magic angle twist*, Nature Physics **17**, 184 (2020).

[52] S. LISI, X. LU, T. BENSCHOP, T. A. DE JONG, P. STEPANOV, J. R. DURAN, F. MARGOT, I. CUCCHI, E. CAPPELLI, A. HUNTER, A. TAMAI, V. KANDYBA, A. GIAMPIETRI, A. BARINOV, J. JOBST, V. STALMAN, M. LEEUWENHOEK, K. WATANABE, T. TANIGUCHI, L. RADEMAKER, S. J. VAN DER MOLEN, M. P. ALLAN, D. K. EFETOV, AND F. BAUMBERGER, *Observation of flat bands in twisted bilayer graphene*, Nature Physics **17**, 189 (2020).

[53] C. WAYMAN AND H. BHADESHIA, *Physical Metallurgy*, 4th ed., edited by R. Cahn and P. Haasen (North Holland, 1996).

[54] W. WEN, C. DANG, AND L. XIE, *Photoinduced phase transitions in two-dimensional charge-density-wave 1T-TaS_2*, Chinese Physics B **28**, 058504 (2019).

[55] M. HOSSAIN, Z. ZHAO, W. WEN, X. WANG, J. WU, AND L. XIE, *Recent Advances in Two-Dimensional Materials with Charge Density Waves: Synthesis, Characterization and Applications*, Crystals **7**, 298 (2017).

[56] G. GRÜNER, *The dynamics of charge-density waves*, Rev. Mod. Phys. **60**, 1129 (1988).

[57] Q. WANG, P. KONG, W. SHI, C. PEI, C. WEN, L. GAO, Y. ZHAO, Q. YIN, Y. WU, G. LI, H. LEI, J. LI, Y. CHEN, S. YAN, AND Y. QI, *Charge Density Wave Orders and Enhanced Superconductivity under Pressure in the Kagome Metal CsV_3Sb_5*, Advanced Materials **33**, 2102813 (2021).

[58] C. LIU, J. SHEN, J. GAO, C. YI, D. LIU, T. XIE, L. YANG, S. DANILKIN, G. DENG, W. WANG, S. LI, Y. SHI, H. WENG, E. LIU, AND H. LUO, *Spin excitations and spin wave gap in the ferromagnetic Weyl semimetal $Co_3Sn_2S_2$*, Science China Physics, Mechanics & Astronomy **64**, 217062 (2020).

[59] W. SCHNELLE, A. LEITHE-JASPER, H. ROSNER, F. M. SCHAPPACHER, R. PÖTTGEN, F. PIELNHOFER, AND R. WEIHRICH, *Ferromagnetic ordering and half-metallic state of $Sn_2Co_3S_2$ with the shandite-type structure*, Physical Review B **88**, 144404 (2013).

[60] Z. GUGUCHIA, J. A. T. VEREZHAK, D. J. GAWRYLUK, S. S. TSIRKIN, J.-X. YIN, I. BELOPOLSKI, H. ZHOU, G. SIMUTIS, S.-S. ZHANG, T. A. COCHRAN, G. CHANG, E. POMJAKUSHINA, L. KELLER, Z. SKRZECZKOWSKA, Q. WANG, H. C. LEI, R. KHASANOV, A. AMATO, S. JIA, T. NEUPERT, H. LUETKENS, AND M. Z. HASAN, *Tunable anomalous Hall conductivity through volume-wise magnetic competition in a topological kagome magnet*, Nature Communications **11**, 559 (2020).

[61] L. A. FENNER, A. A. DEE, AND A. S. WILLS, *Non-collinearity and spin frustration in the itinerant kagome ferromagnet Fe_3Sn_2*, Journal of Physics: Condensed Matter **21**, 452202 (2009).

[62] N. KUMAR, Y. SOH, Y. WANG, AND Y. XIONG, *Magnetotransport as a diagnostic of spin reorientation: Kagome ferromagnet as a case study*, Physical Review B **100**, 214420 (2019).

[63] A. MIELKE, *Ferromagnetic ground states for the Hubbard model on line graphs*, Journal of Physics A: Mathematical and General **24**, L73 (1991).

[64] A. MIELKE, *Exact ground states for the Hubbard model on the Kagome lattice*, Journal of Physics A: Mathematical and General **25**, 4335 (1992).

[65] Y. NAGAOKA, *Ferromagnetism in a Narrow, Almost Half-Filled **s** Band*, Physical Review **147**, 392 (1966).

[66] F. POLLMANN, P. FULDE, AND K. SHTENGEL, *Kinetic Ferromagnetism on a Kagome Lattice*, Physical Review Letters **100**, 136404 (2008).

[67] C. Lacroix, P. Mendels, and F. Mila, eds., *Introduction to Frustrated Magnetism* (Springer Berlin Heidelberg, 2011).

[68] B. J. POWELL AND R. H. MCKENZIE, *Quantum frustration in organic Mott insulators: from spin liquids to unconventional superconductors*, Reports on Progress in Physics **74**, 056501 (2011).

[69] K. KATO, I. KAWADA, C. OSHIMA, AND S. KAWAI, *Lanthanum tetraboride*, Acta Cryst. **30**, 2933 (1974).

[70] J. S. OLSEN, A. WAŚKOWSKA, L. GERWARD, G. VAITHEESWARAN, V. KANCHANA, A. SVANE, N. SHITSEVALOVA, AND V. B. FILLIPOV, *HoB_4 at high pressure and low temperature: an experimental and theoretical study*, High Pressure Research **31**, 3 (2011).

[71] A. HARRISON, *First catch your hare: the design and synthesis of frustrated magnets*, Journal of Physics: Condensed Matter **16**, S553 (2004).

[72] S. S. SUNKU, T. KONG, T. ITO, P. C. CANFIELD, B. S. SHASTRY, P. SENGUPTA, AND C. PANAGOPOULOS, *Hysteretic magnetoresistance and unconventional anomalous Hall effect in the frustrated magnet TmB_4*, Physical Review B **93**, 174408 (2016).

[73] J. SHIN, Z. SCHLESINGER, AND B. S. SHASTRY, *Kondo-Ising and tight-binding models for* $\mathrm{TmB_4}$, Physical Review B **95**, 205140 (2017).

[74] H. WERHEIT, V. FILIPOV, N. SHITSEVALOVA, M. ARMBRÜSTER, U. SCHWARZ, A. IEVDOKIMOVA, V. MURATOV, V. GURIN, AND M. KORSUKOVA, *Raman scattering in rare earths tetraborides*, Solid State Sciences **31**, 24 (2014).

[75] Z. P. YIN AND W. E. PICKETT, *Rare-earth–boron bonding and 4f state trends in RB_4 tetraborides*, Physical Review B **77**, 035135 (2008).

[76] J. ETOURNEAU AND P. HAGENMULLER, *Structure and physical features of the rare-earth borides*, Philosophical Magazine B **52**, 589 (1985).

[77] T. DEVEREAUX AND R. HACKL, *Inelastic light scattering from correlated electrons*, Rev. Mod. Phys. **79**, 175 (2007).

[78] A. BAUM, *Interrelation of lattice, charge, and spin degrees of freedom in iron based systems*, Dissertation, Technische Universität München (2018).

[79] R. STUMBERGER, *Fluctuations and frustrated magnetism in sulphur substituted iron selenide*, Bachelor's thesis, Technische Universität München (2019).

[80] A. SMEKAL, *Zur Quantentheorie der Dispersion*, Naturwissenschaften **11**, 873 (1923).

[81] C. V. RAMAN AND K. KRISHNAN, *A New Type of Secondary Radiation*, Nature **121**, 501 (1928).

[82] G. LANDSBERG AND L. MANDELSTAM, *Eine neue Erscheinung bei der Lichtzerstreuung in Krystallen*, Naturwissenschaften **16**, 557 (1928).

[83] W. HAYES AND R. LOUDON, *Scattering of Light by Crystals* (John Wiley ans Sons, New York, 1978).

[84] R. E. PEIERLS, *Quantum Theory of Solids* (Oxford Univ. Press, Oxford, England, 1955) p. 108.

[85] M.-A. MÉASSON, Y. GALLAIS, M. CAZAYOUS, B. CLAIR, P. RODIÈRE, L. CARIO, AND A. SACUTO, *Amplitude Higgs mode in the 2H-$NbSe_2$ superconductor*, Physical Review B **89**, 060503 (2014).

[86] B. LORET, N. AUVRAY, Y. GALLAIS, M. CAZAYOUS, A. FORGET, D. COLSON, M.-H. JULIEN, I. PAUL, M. CIVELLI, AND A. SACUTO, *Intimate link between charge density wave, pseudogap and superconducting energy scales in cuprates*, Nature Physics **15**, 771 (2019).

[87] N. CHELWANI, A. BAUM, T. BÖHM, M. OPEL, F. VENTURINI, L. TASSINI, A. ERB, H. BERGER, L. FORRÓ, AND R. HACKL, *Magnetic excitations and amplitude fluctuations in insulating cuprates*, Physical Review B **97**, 024407 (2018).

[88] B. MUSCHLER, *Carrier dynamics of $Ba(Fe_{1-x}Co_x)_2As_2$ as a function of doping*, Dissertation, Technische Universität München (2012).

[89] A. BAUM, H. N. RUIZ, N. LAZAREVIĆ, Y. WANG, T. BÖHM, R. HOSSEINIAN AHANGHARNEJHAD, P. ADELMANN, T. WOLF, Z. V. POPOVIĆ, B. MORITZ, T. P. DEVEREAUX, AND R. HACKL, *Frustrated spin order and stripe fluctuations in FeSe*, Commun. Phys. **2**, 14 (2019).

[90] C. HOFFMANN, Diplomarbeit, Technische Universität München (1997).

[91] U. ZWECK, *Electronic and magnetic excitations in underdoped $YBa_2Cu_3O_{6+x}$*, Masterarbeit, Technische Universität München (2018).

[92] D. JOST, *Cooper pairing and fluctuations in Fe-based superconductors*, Dissertation, Technische Universität München (2019).

[93] F. VENTURINI, *Raman Scattering Study of Electronic Correlations in Cuprates: Observation of an Unconventional Metal-Insulator Transition*, Dissertation, Technische Universität München (2003).

[94] W. PRESTEL, *Study of the Interaction Processes in Cuprate Superconductors by a Quantitative Comparison of Spectroscopic Experiments*, Dissertation, Technische Universität München (2012).

[95] M. SIGL, *Magnetismus und Phononen in CuMnAs*, Bachelor's thesis, Technische Universität München (2020).

[96] P. JASCHKE, *Untersuchung der Gitter- und Ladungsträgerdynamik von MnSi in der Umgebung der magnetisch geordneten Phase*, Diplomarbeit, Technische Universität München (2012).

[97] T. STAUFER, *Electronic Raman effect in High-T_C Superconductors with and without magnetic field*, Master's thesis, Technische Universität München (1991).

[98] P. G. KLEMENS, *Anharmonic Decay of Optical Phonons*, Physical Review **148**, 845 (1966).

[99] C. POSTMUS, J. R. FERRARO, AND S. S. MITRA, *Pressure Dependence of Infrared Eigenfrequencies of KCl and KBr*, Physical Review **174**, 983 (1968).

[100] H.-M. EITER, P. JASCHKE, R. HACKL, A. BAUER, M. GANGL, AND C. PFLEIDERER, *Raman study of the temperature and magnetic-field dependence of the electronic and lattice properties of MnSi*, Physical Review B **90**, 024411 (2014).

[101] C. MEINGAST, *private conversation (2021)*.

[102] R. GROSS AND A. MARX, *Festkörperphysik* (Oldenbourg Wissenschaftsverlag GmbH, 2012).

[103] N. W. ASHCROFT AND N. D. MERMIN, *Solid State Physics* (Saunder College, Philadelphia, 1976) p. 493.

[104] A. BISWAS, O. IAKUTKINA, Q. WANG, H. C. LEI, M. DRESSEL, AND E. UYKUR, *Spin-Reorientation-Induced Band Gap in Fe_3Sn_2: Optical Signatures of Weyl Nodes*, Physical Review Letters **125**, 076403 (2020).

[105] S. SCHIPPERS, *Analytical expression for the convolution of a Fano line profile with a gaussian*, Journal of Quantitative Spectroscopy and Radiative Transfer **219**, 33 (2018).

[106] M. V. KLEIN, *Light Scattering in Solids I*, edited by M. Cardona, Topics in Applied Physics, Vol. 7 (Springer, Berlin, Heidelberg, 1983) pp. 147–204.

[107] A. BAUM, A. MILOSAVLJEVIĆ, N. LAZAREVIĆ, M. M. RADONJIĆ, B. NIKOLIĆ, M. MITSCHEK, Z. I. MARANLOO, M. ŠĆEPANOVIĆ, M. GRUJIĆ-BROJČIN, N. STOJILOVIĆ, M. OPEL, A. WANG, C. PETROVIC, Z. V. POPOVIĆ, AND R. HACKL, *Phonon anomalies in FeS*, Physical Review B **97**, 054306 (2018).

[108] Y. Xing, J. Shen, H. Chen, L. Huang, Y. Gao, Q. Zheng, Y.-Y. Zhang, G. Li, B. Hu, G. Qian, L. Cao, X. Zhang, P. Fan, R. Ma, Q. Wang, Q. Yin, H. Lei, W. Ji, S. Du, H. Yang, W. Wang, C. Shen, X. Lin, E. Liu, B. Shen, Z. Wang, and H.-J. Gao, *Localized spin-orbit polaron in magnetic Weyl semimetal $Co_3Sn_2S_2$*, Nature Communications **11**, 5613 (2020).

[109] B. Muschler, W. Prestel, L. Tassini, R. Hackl, M. Lambacher, A. Erb, S. Komiya, Y. Ando, D. Peets, W. Hardy, R. Liang, and D. Bonn, *Electron interactions and charge ordering in CuO_2 compounds*, Eur. Phys. J. Special Top. **188**, 131 (2010).

[110] B. S. Araújo, A. M. Arévalo-López, C. C. Santos, J. P. Attfield, C. W. A. Paschoal, and A. P. Ayala, *Spin–phonon coupling in monoclinic $BiCrO_3$*, Journal of Applied Physics **127**, 114102 (2020).

[111] B. Xu, Y. M. Dai, L. X. Zhao, K. Wang, R. Yang, W. Zhang, J. Y. Liu, H. Xiao, G. F. Chen, S. A. Trugman, J.-X. Zhu, A. J. Taylor, D. A. Yarotski, R. P. Prasankumar, and X. G. Qiu, *Temperature-tunable Fano resonance induced by strong coupling between Weyl fermions and phonons in TaAs*, Nature communications **8**, 14933 (2017).

[112] G. He, L. Peis, D. Li, R. Stumberger, H. T. Yang, H. J. Gao, and R. Hackl, *Strong Fano Resonance of Charge-Density-Wave Amplitude Mode in Kagome Metal CsV_3Sb_5 [Manuscript in preparation (2021)]*.

[113] X. Zhou, Y. Li, X. Fan, J. Hao, Y. Dai, Z. Wang, Y. Yao, and H.-H. Wen, *Origin of charge density wave in the kagome metal CsV_3Sb_5 as revealed by optical spectroscopy*, Physical Review B **104**, l041101 (2021).

[114] E. Uykur, B. R. Ortiz, O. Iakutkina, M. Wenzel, S. D. Wilson, M. Dressel, and A. A. Tsirlin, *Low-energy optical properties of the nonmagnetic kagome metal CsV_3Sb_5*, Physical Review B **104**, 045130 (2021).

[115] K. Nakayama, Y. Li, T. Kato, M. Liu, Z. Wang, T. Takahashi, Y. Yao, and T. Sato, *Multiple energy scales and anisotropic energy gap in the charge-density-wave phase of the kagome superconductor CsV_3Sb_5*, Physical Review B **104**, l161112 (2021).

[116] X. Chen, X. Zhan, X. Wang, J. Deng, X.-B. Liu, X. Chen, J.-G. Guo, and X. Chen, *Highly Robust Reentrant Superconductivity in CsV_3Sb_5 under Pressure*, Chinese Physics Letters **38**, 057402 (2021).

[117] H. Tan, Y. Liu, Z. Wang, and B. Yan, *Charge Density Waves and Electronic Properties of Superconducting Kagome Metals*, Physical Review Letters **127**, 046401 (2021).

[118] H. Miao, H. X. Li, W. R. Meier, H. N. Lee, A. Said, H. C. Lei, B. R. Ortiz, S. D. Wilson, J. X. Yin, M. Z. Hasan, Z. Wang, H. Tan, and B. Yan, *Geometry of the*

charge density wave in kagom metal AV_3Sb_5, (2021), arXiv:2106.10150 [cond-mat.str-el] .

[119] R. Samnakay, D. Wickramaratne, T. R. Pope, R. K. Lake, T. T. Salguero, and A. A. Balandin, *Zone-Folded Phonons and the Commensurate–Incommensurate Charge-Density-Wave Transition in 1T-$TaSe_2$ Thin Films*, Nano letters **15**, 2965 (2015).

[120] O. R. Albertini, R. Zhao, R. L. McCann, S. Feng, M. Terrones, J. K. Freericks, J. A. Robinson, and A. Y. Liu, *Zone-center phonons of bulk, few-layer, and monolayer 1T-TaS_2: Detection of commensurate charge density wave phase through Raman scattering*, Physical Review B **93**, 214109 (2016).

[121] H. Li, T. T. Zhang, T. Yilmaz, Y. Y. Pai, C. E. Marvinney, A. Said, Q. W. Yin, C. S. Gong, Z. J. Tu, E. Vescovo, C. S. Nelson, R. G. Moore, S. Murakami, H. C. Lei, H. N. Lee, B. J. Lawrie, and H. Miao, *Observation of Unconventional Charge Density Wave without Acoustic Phonon Anomaly in Kagome Superconductors $A\mathrm{V}_3\mathrm{Sb}_5$ ($A = \mathrm{Rb}$, Cs)*, Phys. Rev. X **11**, 031050 (2021).

[122] C. S. Snow, J. F. Karpus, S. L. Cooper, T. E. Kidd, and T.-C. Chiang, *Quantum Melting of the Charge-Density-Wave State in 1T-$TiSe_2$*, Physical Review Letters **91**, 136402 (2003).

[123] R. Grasset, Y. Gallais, A. Sacuto, M. Cazayous, S. Mañas-Valero, E. Coronado, and M.-A. Méasson, *Pressure-Induced Collapse of the Charge Density Wave and Higgs Mode Visibility in 2H-TaS_2*, Physical Review Letters **122**, 127001 (2019).

[124] P. Vaqueiro and G. G. Sobany, *A powder neutron diffraction study of the metallic ferromagnet $Co_3Sn_2S_2$*, Solid State Sciences **11**, 513 (2009).

Acknowledgments

Only teamwork makes the dream work. Hence, I'd like to thank everyone who made this whole year one hell of a ride, who supported me during my time at the Walther-Meißner-Institute and while writing this thesis.

Prof. Dr. Rudi Hackl
for supervising this thesis, for his knowledge and wisdom, his help in the lab, for introducing me to Raman spectroscopy and scientific work, for proof-reading this thesis, and for the coffee and sweets.

Prof. Dr. Rudolf Gross and Prof. Dr. Stefan Filipp
for the opportunity to perform measurements for my master's thesis and to work in a good atmosphere at the Walther-Meißner-Institute.

Leander Peis
for all the late nighters, the coffee, the beer, the fun, and all these phrases I will never forget. I couldn't have asked for a better one. Never forget our number one motto and all the other life-changing mottos.

Ge He
for his help, his knowledge, his support, and the fun. I know, you're still waiting for the good news. Me too.

Andreas Baum
for his support in the lab and his help, although he wasn't working for the WMI anymore.

The WMI staff
especially the craftsmen of the WMI workshop and the technicians of the He liquefaction, for not only their help at work related stuff but also for always having an open ear, a good advice or just a warm and comforting smile.

The staff of the TUM crystal laboratory
for their help with the sample preparation.

Sybilla Plöderl and Maria Botta
for the talks, the hugs, the chocolate and the support.

All Bachelor, Master, PhD students, and Postdocs

for not only the work-related discussion and the help through ups and downs, but especially the never-ending ice cream breaks (still holding the record of five ice cream breaks a day), the coffee breaks, the Glühwein and Kinderpunsch breaks (it got too cold for ice cream but breaks are very important), the food (thanks Yuki!), the Room-128-raves (cleanroom raves were just for the cool kids, but SSIO a day, keeps the doctor away), the strong Meme-game, the races with our chairs, and so on and so on. I could probably fill a whole book with all the stuff we've done. I'm going to miss you all. P.S. thanks for the promised memes I never got, except for Nykki's.

Especially I want to thank

- **The "Hong Hong Crew"**, especially Matthias Grammer, Manuel Michael Müller, Florian Fesquet, Yuki Nojiri, and Kedar Eshwar Honasoge. God damn, without you I would have laughed way less, I wouldn't know so many new bad jokes and I wouldn't have thought about being a donut. But always remember, what happens at "Hong Hong", or anywhere else, stays at "Hong Hong".
- **Niklas Bruckmoser** for introducing me to Techno-music (thanks for the best mix-tapes ever), the endless conversations, and for being our "rock" in room 128 and my personal Life coach. Baddest best b***h on earth forever.
- **Philipp Schwenke** for not only his daily bad jokes (God damn, you totally rubbed off on us), but for being a good friend.
- **Leonhard Hölscher** for always being there, not only for me, but anybody and for cheering us all.
- **Lukas Vetter** for all our jokes, nobody understood. There's a blonde person out there, who won't consider you as attractively repulsive. Until then, just keep going with the wardrobe nicknames.
- **Johannes Schirk** for not being the Flunky-ball team member I wanted nor the one I needed, but the one I got. Next time, you start to throw the piece of wood (no budget for a real ball). By the way, your IT service ("Lad dir endlich Chrome runter!") was the best I ever got.
- **Monika Scheufele**. I loved all of our (deep) talks, our laughs and our gossiping.
- **Elisabeth Meidinger** for always having an open ear, a warm hug and a good advice. No matter what.

My family

Mom, Dad, Robin, and Rocco, I couldn't have done it without your endless support and your love. I love you so much.

"Beloved WMI, enjoy the calm after the storm!"